CHAPTER 6

Magnetic Properties of Conducting Polymers

Kenji Mizoguchi and Shin-ichi Kuroda†*

Tokyo Metropoliton University Japan
†Electrotechnical Laboratory, Tsukuba, Japan

1 INTRODUCTION

When considering 'Magnetic Properties' one immediately thinks of 'susceptibility'. Susceptibility is one of the basic properties that characterizes materials science. In this chapter, 'Magnetic Properties' in its wide meaning including 'susceptibility' will be critically reviewed, particularly in the field of conjugated/conducting polymers. We discuss mainly experimental results obtained by magnetic resonance techniques; NMR (nuclear magnetic resonance), ESR (electron spin resonance), ENDOR (electron-nuclear double resonance). Many reviews related to magnetic properties have been reported [1–7] especially in the field of the conjugated polymers—a comprehensive and well organized review has been written by Kahol et al. [2]. This review focuses in some detail, critically, on magnetic resonance studies of lattice structures, the structure and dynamics of the neutral soliton in polyacetylene (PA) and other excitations, spin dynamics in conducting states, susceptibility and ESR linewidth. The authors will be grateful for any comments on errors found in this work which will aid them in their revision of the work.

Even in limited topics on 'Magnetic properties', there are a huge number of titles to be discussed and it is impossible to cover all of them within the limited time span and ability given. The basic concepts on the magnetic resonances are compactly summarized in [2] and in detail in [8–11]. The conducting polymers are intrinsically one-dimensional systems with strong electron–lattice coupling. Doping changes their electronic state from insulating/semiconducting to conducting/metallic and induces a variety of electronic elementary excitation, solitons, polarons and bipolarons, which is one of the attractive features of the conducting polymers as summarized in [1,12–19]. The characteristics of such excitations are of continuing interest in this field; their stability and dynamics in a variety of polymers, has applications in science and technology. Some topics which are not covered are well covered by reviews in the literature on magnetic properties in conjugated and conducting polymers, for example, on high-resolution NMR studies, light-induced ESR and polydiacetylene [2].

2 STRUCTURAL STUDY BY MAGNETIC RESONANCE

Since most of the conjugated polymers contain a lot of protons which give a strong NMR signal by virtue of their large nuclear magnetic moment, ^{1}H NMR line broadening due to the nuclear dipolar interaction is a good candidate for extraction of structural information on the semi-crystalline conjugated polymers. For this purpose the second M_2 and the fourth M_4 moments of the NMR spectrum are powerful tools, since it is theoretically simple, compared with the lineshape itself [2,8,11]. As a standard technique for such an analysis, continuous-wave (cw) NMR is adopted to obtain NMR spectrum $f(\omega)$, followed by numerical integration to calculate the $2n$th moments M_{2n} defined by

$$M_{2n} = \frac{\int \omega^{2n} f(\omega) \, d\omega}{\int f(\omega) \, d\omega}. \tag{6.1}$$

For polyacetylene (PA) and polyparaphenylene (PPP) several investigations with cw-NMR have been reported [20–24]. Concerning this method, an improvement on how to estimate more accurately the second moment M_2 has been proposed [25].

Using a complementary technique of pulse NMR the moments of the spectrum are also given by the free induction decay (FID) $G(t)$ with the relation [2,8,11]

$$M_{2n} = (-1)^n \left(\frac{d^{2n} G(t)}{dt^{2n}} \right)_{t=0} \Big/ G(0). \tag{6.2}$$

The cw-NMR is orthodox and sufficiently reliable if the signal-to-noise ratio of the spectrum is high enough to estimate its baseline precisely. In the pulse NMR case, on the other hand, since the short-time behaviour immediately after the intense radio-frequency (rf) pulse irradiation is important, as expected from (6.2), recovery time or dead time of the experimental equipment after the pulse, causes a serious limitation of reliability for the estimated moments. To overcome this weak point the improvements in technique, the magic echo sequence [26–29] and in analysis, the functional forms of fitting [30–32] were applied to recover the FID signal at $t = 0$. Details are described in [2].

In this chapter the second moment studies are mainly reviewed for the two typical conjugated polymers; Shirakawa-type (S-PA) [20–22,27,30–32] and Naarmann and Theophilou-type (NT-PA) polyacetylenes [24] and polyparaphenylene [23,28,29]. The characteristic of NT-PA is a high degree of chain orientation attained by mechanical stretching, [33] which provides additional information on the polymer chain arrangement; how much misorientation of the chains is left behind and how much of the amorphous portion exists [34]. From an analysis of the second moment M_2

together with the frequency dependence of the ESR linewidth and the spin-spin relaxation rate T_2^{-1}, the neutral soliton is found to distribute inhomogenously in the crystalline and the amorphous part of $(CH)_x$ [24].

Finally, rationality of the crystal structures proposed by X-ray and electron-beam diffraction techniques [35–51] can be estimated by comparing the second moments M_2 calculated from such structure with those of NMR spectra.

2.1 Polyacetylene

2.1.1 Shirakawa polyacetylene

Typical absorption and the derivative lineshapes of ^1H cw-NMR taken at 20 K in *trans*-polyacetylene (*trans*-PA) are shown together with the Gaussian lineshape in Figures 6-1(a) and (b) [22]. It is easily found that the lineshape in *trans*-PA is markedly different from the Gaussian lineshape as demonstrated in this figure. Such a deviation from the Gaussian lineshape is consistent with the observation of oscillatory FIDs [2,27,30,32].
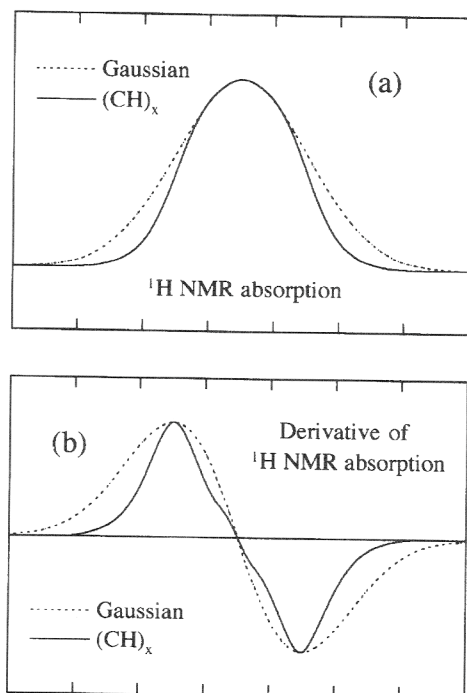

Figure 6.1. ^1H NMR lineshape in *trans*-PA taken at 20 K, [22] compared with the Gaussian lineshape shown by the dotted curves with the same peak-to-peak linewidth as *trans*-PA: (a) absorption spectra; and (b) derivative of absorption.

Although Ikehata and co-workers have reported that the observed lineshape could be approximated by the Gaussian lineshape studied by cw-NMR [21], the increased S/N ratio clearly revealed the deviation from the Gaussian lineshape [22,30]. The absorption lineshape in Figure 6-1(a) is closer to the boxshape than the Gaussian shape. The Gaussian lineshape is expected when there is a sufficiently large number of equivalent protons which produce the largest and the same nuclear dipolar field at the reference site, because they give a binomial distribution of resonance lines as a component for the lineshape. More distant nuclei simply broaden such lines to form a continuous Gaussian-like distribution.

A good example was found in the ^{19}F NMR lineshape of CaF_2 single crystals [8,52]. Fluorine atoms form a simple cubic lattice. When the magnetic field is directed in the [100] direction, only *two* of the six first-nearest neighbour (1st-nn) fluorines make the largest dipolar field, resulting in a flat-top, box-type lineshape very different from the Gaussian. On the other hand, when the magnetic field is directed to [110] and [111] directions, *four* of the six 1st-nn fluorines for [110] and the *six* of the twelve 2nd-nn fluorines for [111] play such a role, and result in a gradual change of the lineshape from the box to the Gaussian as the magnetic field was directed from [100] to [110] and further to [111]. (Here, the six 1st-nn fluorine nuclei for [111] do not contribute to the dipolar field parallel to the magnetic field, since they are positioned at the magic angle i.e., $\cos\theta = 1/\sqrt{3}$.) In the case of PA, since *only the two* 1st-nn protons along the chain with a distance $r_{nn} = 2.46$ Å play the role, some deviation from the Gaussian lineshape could be expected. The local field by 2nd-nn protons with $r_{2nn} = 3.13$ Å is only one-fifth of the 1st-nn protons, small enough to act as a perturbation to broaden the split resonance lines by the 1st-nn protons. Therefore, the observation of the flat-top lineshape in *trans*-PA is physically reasonable.

The peak-to-peak linewidth ΔH_{pp} of the absorption derivative of ^1H NMR in *trans*-PA shows a little narrowing from the 8.9 G at 4.2 K to 8.1 G at 300 K as shown in Figure 6.2 [22]. The possible origin of this temperature dependence of the linewidth could be assigned by comparing ΔH_{pp} with the second moment M_2, because motional narrowing of NMR spectra can reduce the linewidth, but does not change the second moment M_2, as shown quantum mechanically [8,11]. In conclusion, the temperature dependence of the lattice parameter is the origin of the observed temperature dependence of ΔH_{pp}, that is, the second moment M_2 of ^1H NMR varies proportionally with the
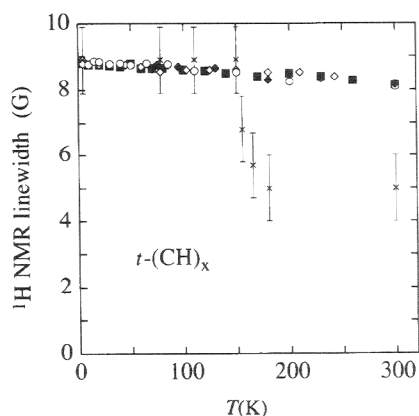
Figure 6.2. The temperature dependence of the ^{1}H NMR peak-to-peak linewidth ΔH_{pp} in *trans*-PA [21,22]: ×, after [21]. The other symbols: ◆ (2.0 G); ○ (1.5 G); ◇ (1.3 G); ■ (1.0 G) are taken from [22], where the figures in the parentheses mean the ESR linewidth ΔH_{pp} at 50 MHz and 300 K. It is remarkable that ΔH_{pp} is practically independent of the magnitudes of the second moments M_2. The curious behaviour of × symbols was interpreted by the motional narrowing due to chain rotation around the chain axis [21]. So far, no successful follow-up of this data has been reported [2,20,22,30].
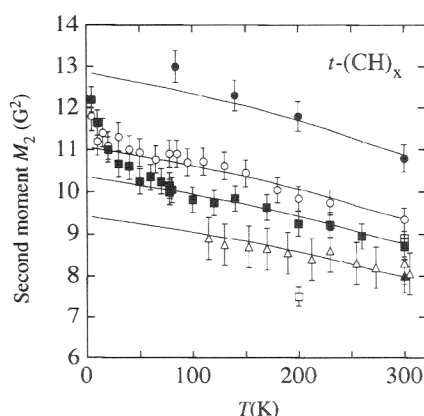

Figure 6.3. The temperature dependence of the second moment M_2 in *trans*-PA: ● [28]; □ [2]; ▲ [32] were obtained by the pulse techniques. The first two data at 200 K are the same data, but analyzed with different fitting functions to estimate M_2. ⊞ [20]; ○ (1.3 G); ■ (1.0 G); ▲ (0.5 G) [22]; △ [30] were taken by cw-NMR for different batches of *trans*-PA, where the figures in the parentheses mean the ESR linewidth ΔH_{pp} at 50 MHz and 300 K. The solid curves indicate $\varepsilon \Delta H_{pp}^2$, where $\varepsilon = 0.121$, 0.133, 0.141 and 0.165 from bottom to top. For the Gaussian lineshape, $M_2 = 0.25 \, \Delta H_{pp}^2$ holds.

square of the linewidth ΔH_{pp} as shown by the solid curves in Figure 6.3, which demonstrates invariance of the lineshape and absence of the motional narrowing. It is worth noting that the lineshape actually shows negligible change through 100 K–300 K [22], which contrasts with the case of PPP (see section 2.2) [2,23,29]. Below 100 K, however, a broadening tail appears and its magnitude apparently depends on the samples. To detect this tail, a careful study is required, for example, it needs a wide scan range of the magnetic field and a high enough S/N ratio. The origin of such broadening could be assigned to the para-magnetic spins of the trapped neutral solitons. In this figure, the large difference of the excess broadening below 50 K, depending on the samples, is not coming from the neutral soliton concentration, but from the measuring condition, i.e. the range of magnetic field scan.

So, the problem is the systematic difference observed in M_2 above 100 K, as shown in Figure 6.3. Two factors can be considered. The first is of technical origin and the second is an intrinsic one. Firstly, the data reported by different groups with the cw-NMR converge to the narrow range of $M_2 \sim 8$–9 G^2 [20,22], while the data analysis of FID and the magic echo with the pulse NMR seems to be sensitive to the functional forms for fitting as demonstrated by the filled circles and the open square at 200 K in Figure 6.3 [2]. The second point is a correlation between M_2 and the ESR linewidth demonstrated in Figure 6.4 [22]. The observed second
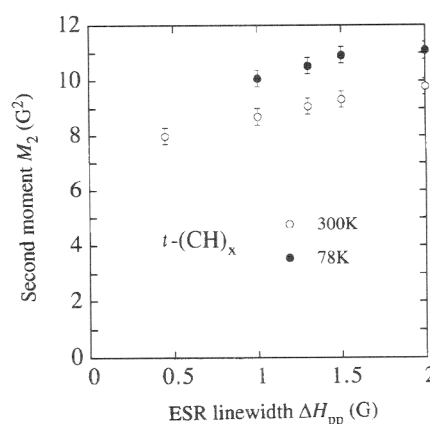

Figure 6.4. The second moment M_2 versus the ESR linewidth (taken at 50 MHz) at 300 and 78 K in *trans*-PA [22]. The second moment M_2 increases with increasing ESR linewidth. It is expected that the intrinsic second moment of the *trans*-isomer is realized at the minimum of the ESR linewidth, see text for details.

moment M_2 taken at 300 and 78 K varies systematically with the ESR linewidth taken at 300 K and 50 MHz. The ESR linewidth is governed mainly by the width due to trapping which is the same as the inhomogeneous hyperfine broadening in nature, as will be shown in Section 4.3. Let us consider the process of thermal isomerization from *cis*- to *trans*-isomers. In *cis*-PA the ESR linewidth is broad, 6–8.5 G at 300 K [53,54], due to the hyperfine broadening of the trapped neutral soliton [54] and the second moment M_2 is as large as almost 20 G^2 [35–38]. As the isomerization proceeds, *trans*-segments increase and the soliton becomes free to move in the *trans*-isomer, resulting in the motional narrowing of the ESR linewidth. After passing through the minimum of the ESR linewidth, that is, less than 0.5 G at X-band, it begins to broaden possibly due to degradation of the polymer chain itself and cross-linking between chains which traps the solitons, causing ESR broadening, and also increase of the second moment M_2. Therefore, it is expected that the second moment M_2 will reach the minimum in the ideal *trans*-PA.

Thus obtained from Figure 6.4, the second moment $M_2 = 8.0 \pm 0.5$ G^2 for the best *trans*-PA sample at 300 K, can be compared with that calculated from the proposed model structures [2,39–48]. Simplified model structures of *trans*-PA are shown in Figure 6.5. Using these structures with the lattice parameters in Table 6.1 and $P2_1/a$ space group, the second moment M_2 is calculated as a function of a setting angle ϕ_{set} in Figure 6.6. To compare the experimental result with the calculated one, two corrections were made: (1) the effect of the surface area of fibrils with the diameter of
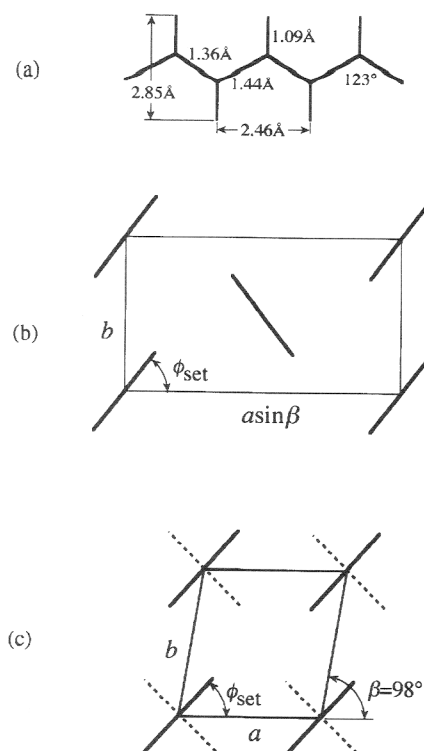
Figure 6.5. The simplified model structure for *trans*-PA: (a) the model structure of single chain; (b) the orthorhombic structure, Akaishi *et al*, [41] Shimamura *et al*, [42] Baughman *et al* [39,40] and Fincher *et al* [43]; and (c) the monoclinic structure, Lieser *et al* [45,46].

Table 6.1. The various lattice parameters of the model structures for *trans*-polyacetylene. See Figure 6.5 for the notation, c is the chain direction, a is taken as the longest axis

Reference	a (Å)	b (Å)	c (Å)	Space group	ϕ_{set} (°)	β (°)
Akaishi *et al* [41]	7.37	4.06	2.45	—	53	90
Lieser *et al* -1 [45]	3.73	3.73	2.44	—	—	98 (γ)
Lieser *et al* -2 [45]	5.62	4.92	2.59	—	—	90
Baughman *et al* -1 [39]	7.41	4.08	2.47	$P2_1/a$	48	91.3
Baughman *et al* -2 [40]	7.38	4.12	2.47	—	53	98
Shimamura *et al* [42]	7.32	4.24	2.46	*Pnam*	24	—
Fincher *et al* [43,47]	7.32	4.24	2.46	$P2_1/n$	55	91.5
Kahlert *et al** [48]	7.34	4.18	2.46	$P2_1/a$	57	90.5
Weber [28]			Prefers Shimamara *et al* [42]			
	7.32	4.12	2.46			
Mizoguchi *et al* [22]	~ 7.38	~ 4.24	~ 2.47	$P2_1/a$	52 ± 5	—

* Durham polyacetylene was used
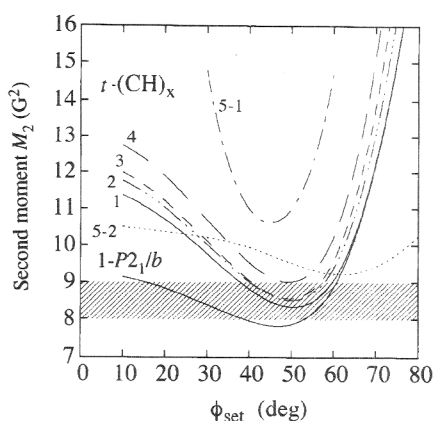
Figure 6.6. The calculated second moment M_2 for the model structures of *trans*-PA (Table 6.1) as a function of the setting angle ϕ_{set} [22]. The long broken curve, 4: Akaishi *et al* [41]; the dashed-dot, 5-1 and the dotted curves, 5-2: Lieser *et al* [45,46]; the broken curve, 3: Baughman *et al* [39,40]; the solid curve, 1: Shimamura *et al* [42] and Fincher *et al* [43] and the dashed-three dots, 2: Kahlert *et al* [48]. Data is not shown, but note that M_2 is insensitive to the change of the angle β. All the calculations were made for the $P2_1/a$ space group, except for the curve 1, where the $P2_1/b$ space group is also calculated. The hatched area indicates the expected range of the experimental value of M_2 for *trans*-PA.

200 Å and (2) the effect of the amorphous region. Since both the effects tend to reduce the observed M_2, the present corrections enhance the observed M_2. Finally, $M_2 = 8.5 \pm 0.5$ G^2 was obtained as shown by the hatched area in Figure 6.5 [22]. This magnitude of M_2 is compatible with the model structures by Baughman *et al*. [39,40], Shimamura *et al*. [42], Fincher *et al*. [43] and Kahlert *et al*. [48], with the setting angle $\phi_{set} = 50° \pm 5°$ which is compared with 48–57° estimated by x-ray studies [39–41,43,47,48]. It is noteworthy that Figure 6.6 implies a larger setting angle $\phi_{set} \approx 55$–60° for the space group $P2_1$/b. On the other hand, the model by Lieser *et al*. is incompatible with the second moment as reported earlier [22,30].

Figure 6.7 shows the thermal expansion Δ (=100 $[l(T) - l(0)]/l(0)$ (%), $l = a$ or b) in *trans*-PA [2,22] estimated by a similar method used in [2] with the relation $M_2(T) = M_2(0) - 0.041\Delta + 0.0016\Delta^2$. Here, $M_2(0)$ was estimated by extrapolating the solid curves shown in Figure 6.3 to $T = 0$. The expansion in *trans*-PA shows larger magnitude and rather more linear temperature dependence than in the case of polytetrafluoroethylene (PTFE) [55]. Providing the Grüneisen expression for the linear expansion coefficient [55], such linear behaviour is expected from its linear specific heat as reported in [56–58].
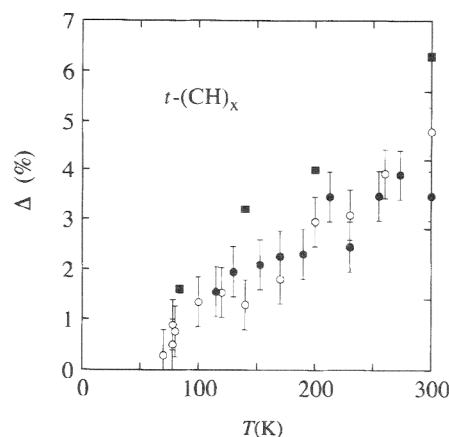
Figure 6.7. The thermal expansion, Δ (%), in *trans*-PA derived from the temperature dependence of the second moment M_2, shown in Figure 6.3 [2,22,28]. ○ [22], ● [22], ■ [28]. See text for further details.

Figure 6.8 indicates the dopant concentration dependence of the second moment M_2 in *trans*-PA and PPP [20,23,30,32]. The reduction of the second moment M_2 upon doping is clearly demonstrated in both *trans*-PA and PPP. Note that most of the reduction in M_2 occurs between 5 and 10% of doping. In the concentration, less than or more than in the range of doping, M_2, depends weakly on the dopant concentration. This observation suggests that, below 5% the effect of
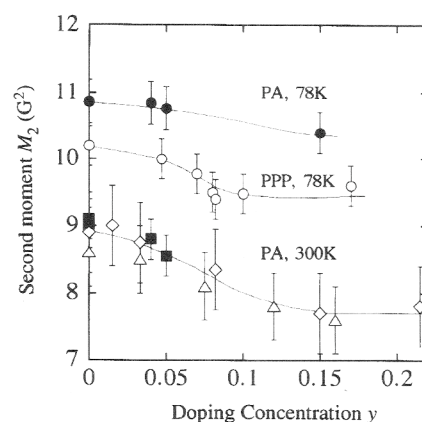
Figure 6.8. The seocnd moment M_2 for *trans*-PA and PPP as a function of various dopant concentrations. *Trans*-PA doped with AsF$_6$: ● at 78 K; ■ at 300 K [22]; *trans*-PA doped with Iodine, ◇ at 300 K [20]; △, at 300 K [32]; and PPP doped with AsF$_6$: ○, at 78 K [23]. The reduction of M_2 is clearly observed with increasing y. The solid curves are a guide for the eye.

doping is local, probably limited to the surface region of fibrils. Between 5 and 10%, a structural change takes place, leading to a volume expansion by the insertion of the dopant between chains, and above 10% the average distance of dopants reduces with concentration, then the volume change becomes weak again. This picture can be compared with the observation by X-ray analysis for Na doped PA [59]. The second moment in *cis*-PA shows a more pronounced change than in *trans*-PA upon doping because of a volume change caused by the *cis* to *trans* isomerization upon doping [20,30].

2.1.2 Highly oriented polyacetylene

To attain a better characterization of polymers, stretch-oriented films are highly useful [24,60–62]. Shirakawa polyacetylene (S-PA) has been known to be mechanically stretchable to a partially oriented film, up to three times with the electrical conductivity of several thousands of S/cm [60]. In 1986, two new routes of polymerization of highly oriented PA was reported to attain the conductivity of up to several tenth thousands of S/cm with liquid crystals (LC-PA) [63] and a precursor polymer (Durham route, D-PA) [64]. In 1987, Naarmann and Theophilou remarkably improved the conventional Shirakawa method (NT-PA) to obtain highly conductive, up to 10^5 S/cm comparable to that of copper, highly stretchable up to ten times, and high density PA by introducing a high temperature aging of catalyst [33]. In 1989 further modification linked with the high-temperature aging of catalyst called as non-solvent (NS) or solvent-evacuation (SE) polymerization, resulting in high density and mechanically strong film, was reported by Akagi and Shirakawa (SE-PA) [65]. In 1990 the highest conductivity of more than 10^5 S/cm was reproduced with the modification of the high-temperature aging of catalyst by Tsukamoto *et al.* (T-PA) [66,67]. Very recently, Akagi *et al.* reported an intrinsic non-solvent (INS) polymerization method suitable for a highly conductive and strong film (INS-PA) [68]. In this section a systematic analysis of the Naarmann and Theophilou type polyacetylene (NT-PA) with a magnetic resonance technique will be summarized [24].

The second moment of ^{1}H NMR in the six-fold stretch-oriented *trans*-NT-PA is demonstrated in Figure 6.9 as a function of an angle γ of the stretch direction with the magnetic field [24,34]. The dotted curve indicates the calculated second moment for the ideally oriented sample, where a partial averaging about the angle δ (see, Figure 6.10) was made to correspond to
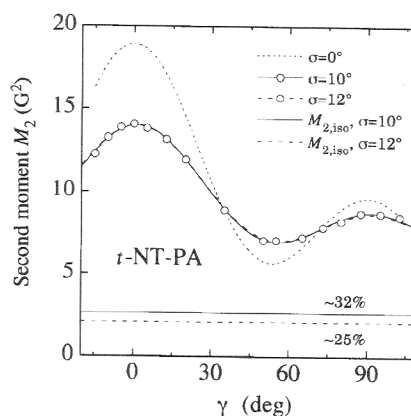
Figure 6.9. The angular dependence of the proton second moment in the six-fold stretch-oriented NT-PA [24]. γ is the angle of the stretched direction (chain axis) with the magnetic field. The dotted curve shows the expected behaviour calculated with the parameters, $a = 7.32$ Å, $b = 4.24$ Å, $c = 2.46$ Å, C-H = 1.09 Å and setting angle of 55°, for the perfectly aligned crystal. σ is a standard deviation of the Gaussian distribution assumed for the residual misorientation after mechanical stretching. Taking account of the randomness in the (a,b)-plane in Figure 6.5 for the substantial film, an averging of the second moment about the angle δ was made in these curves. The solid and the dashed curves are the best fit to the data, calculated with $\sigma = 10°$ and 12° and the residual isotropic contribution of 32% and 25% due to the amorphous region of the sample, respectively.
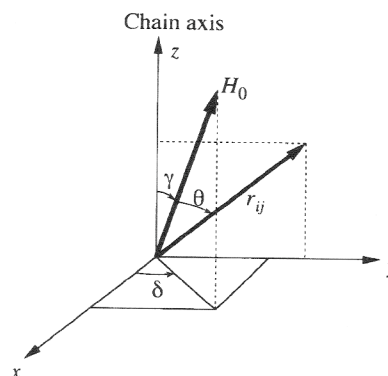
Figure 6.10. The relationships among the chain axis, the vector connecting two spins r_{ij} and the magnetic field H_0.

the actual system where directions of the a and b axes are random in the film. Furthermore, the presence of a residual misorientation in the actual film has been taken into account assuming a Gaussian distribution, to reproduce the experimental data. Although the result of such a calculation is not in Figure 6.9, the anisotropy

cannot be reproduced without a constant contribution independent of the angle γ. As shown by the solid and dashed curves, the data points are successfully reproduced with the standard deviation $\sigma \approx 10\text{--}12°$ and the constant of 25–32% which is probably due to an unoriented amorphous part of the film. Thus obtained, the crystallinity of 70–80% is consistent with that deduced by X-ray diffraction [69].

Using a structural study by magnetic resonance methods, ^{1}H NMR and ESR spin-lattice relaxation data, and the ESR linewidth in the same NT-PA sample as the second moment experiment were analysed [24,34]. The ESR linewidths of stretch-oriented *cis*-rich NT-PA [34] are plotted versus the angle γ in Figure 6.11, together with S-PA [54] and SE-PA [70]. The ESR linewidth in the case of the *cis*-isomer is dominated by the hyperfine broadening due to the proton nuclei [5,9,54]. A simplified fitting was tried using an anisotropy of the hyperfine coupling constant with a fitting parameter k, [9]

$$H_{\mathrm{hyp}} = k[A_\perp^2 + A_\parallel^2 \cos^2 \gamma]^{1/2} \qquad (6.3)$$

where the axial symmetric parameters $A_\parallel = -90$ MHz and $A_\perp = -45$ MHz are used since the alignment of

the chains is limited along the stretch oriented direction, [5,54] which should be proportional to the ESR linewidth. Here, $A_\parallel = A_y$ means the magnetic field parallel to the stretch direction of the c-axis, and $a_\perp$ is an average of A_x and A_z (Figure 6.18). The solid curve in Figure 6.11 shows (6.3) averaged out on the Gaussian distribution with $\sigma = 10°$. A remarkable point of this figure is in the larger isotropic contribution $\sim 40\%$ greater than 25–42% found in the second moment of the same but *trans*-form sample. This suggests that 40% of the paramagnetic spins were in the amorphous region, nevertheless the volume of amorphous region is 20–30% as estimated from the second moment.

The apparent contradiction of the amorphous size can be ascribed to an inhomogeneous distribution of the paramagnetic spins between the crystal and the amorphous regions, that is, the neutral soliton is preferably created in the amorphous region upon isomerization. Gibson and co-workers have proposed a model for the neutral soliton creation using FT-IR technique that about 6% of isolated *cis*-linkages remained in *trans*-PA chain are the source of such defects [71]. The remnant *cis*-linkages could also be a source of structural disorder. Several authors discussed the fact that in the bond alternation defect, the neutral soliton prefers structural disorder [72–74].

The spin-lattice relaxation rate T_{1e}^{-1} of ESR in *trans*-NT-PA is plotted in Figure 6.12 [24]. The origin of T_{1e}^{-1} comes mainly from the diffusional motion of the neutral soliton which induces the relaxation through modula-

Figure 6.11. The peak-to-peak ESR linewith in *cis*-rich-PA measured as a function of the angle γ at the X-band. γ is the angle between the chain axis and the magnetic field. ●, [54], for 90% *cis*-rich-S-PA stretched by 230%; , □ [70] for *cis*-rich-SE-PA stretched by 700%; ○ [34] for $\sim 50\%$ *cis*-rich-NT-PA stretched by 600%, that is the same sample as Figure 6.9. The dotted, the dash-dotted and the solid curves show the best fit to the hyperfine broadening described by (6.3) with the isotropic contribution due to the amorphous part that is $\sim 40\%$ for [34]. The broken line shows a powder average for [34]. Such a large magnitude of the isotropic part contradicts the 25–32% deduced from the second moment as shown in Figure 6.9.

Figure 6.12. The electron spin-lattice relaxation rate in the same *trans*-NT-PA as that of M_2 in Figure 6.9 as a function of the angle γ measured at 50 MHz [24]. The solid curve indicates the best fit of the model calculation (see text for details). The large isotropic contribution due to the amorphous part is required to reproduce this data.

tion of the dipolar and hyperfine couplings, including motional narrowed hyperfine width, as will be mentioned in Section 4.3. The model fit obtained by av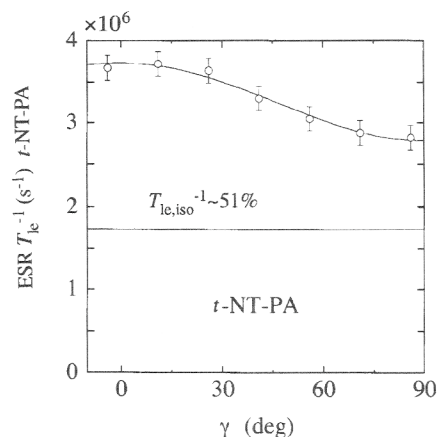eraging out the misorientation reproduces the data well, but requires about 50% of the isotropic contribution, due to the amorphous region. Such a large value is comparable with 40% for the ESR linewidth in *cis*-NT-PA, but is somewhat larger than 25–32% for the second moment. The tiny difference between 50% and 40% in *cis*-NT-PA is easily accountable for by the succeeding isomerization from *cis* to *trans*-isomer.

The ESR linewidth of *trans*-NT-PA measured at 50 MHz is shown in Figure 6.13, [24,34] together with that of *trans*-SE-PA [70] via Akagi's route and *trans*-D-PA [75] via the Durham route, measured at the X-band. A broader ESR linewidth than that (< 1G) in S-PA is a characteristic feature of *trans*-NT-PA [76,77]. The origins of the ESR linewidth in *trans*-PA is more complicated than the *cis*-case and also frequency dependent, as will be discussed in Section 4.3; the anisotropy pattern is a result of the counterbalance of two different mechanisms, the hyperfine broadening with the same pattern as *cis*-PA and the lifetime broadening due to the neutral soliton diffusion with the reversed pattern [6,34,61,62,78–82]. As demonstrated in Figure 6.13 the amplitude of the anisotropy in *trans*-$(CH)_x$ measured at the X-band is larger than that at

50 MHz, due to a decrease in the lifetime broadening, in agreement with the observation in stretched S-PA [61]. First the contribution due to the diffusive motion of spins was subtracted from the observed ESR linewidth and then a fit was made by (6.3) with averaging out of the misorientation, since the diffusion part can be estimated from the ESR spin-lattice relaxation rate which has the same origin as the ESR linewidth. Finally the data can be well reproduced by the solid curve in Figure 6.13, with $\sim 50\%$ of the amorphous part that is in good agreement with T_{1e}^{-1} case.

The above conclusions on the magnitude of the isotropic part (25–32% for the second moment of ^{1}H NMR and $\sim 50\%$ for both the ESR linewidth and T_{1e}^{-1} in *trans*-NT-PA) imply that the concentration of the neutral soliton in the amorphous part is higher by $\sim 7/3$, more than twice that in the crystalline region.

Finally ^{1}H NMR T_{1H}^{-1} in *trans*-NT-PA is mentioned briefly. The anisotropy pattern of ^{1}H NMR T_{1H}^{-1} in *trans*-S-PA has been reported to be basically understandable with neutral soliton diffusion [62]. Does it hold even for *trans*-NT-PA? The angular dependence of T_{1H}^{-1} is shown in Figure 6.14 [24]. It is noteworthy that the depression around $\gamma = 90°$ is deeper than that in *trans*-S-PA and the origin of such a depression cannot be expected from the diffusion mechanism of the neutral solitons as depicted by the solid curve B in Figure 6.14. To account for such a depression by another mechanism, spectral diffusion and localized spins as described in (6.18) (see, [8] p. 379) [8,83] it is

Figure 6.13. The ESR half-width at half intensity ($= T_{2e}^{-}$) in *trans*-PA as a function of the angle γ. ■ [75] are D-PA and ◆ [70] are SE-PA, measured at the X-band, and open circles [24] are NT-PA measured at 50 MHz. The ESR lineshape is always well represented by the Lorentzian lineshape [24]. The solid and the dashed curves indicate the best fit of the model calculation (see text for detail). The straight line shows the isotropic contribution resulting from the amorphous part of *trans*-NT-PA, which is comparable to, but a little larger than *cis*-NT-PA.

Figure 6.14. The ^{1}H NMR T_{1H}^{-1} in *trans*-NT-PA as a function of the angle γ at 50 MHz [24]. The solid curve A is a total of the three parts, B, C and the isotropic one. B is the neutral soliton diffusion mechanism via modulation of the dipolar, the hyperfine and their cross-couplings. C is the localized spin + spectral diffusion mechanism [8,83]. The straight line is the isotropic contribution.

attempted to fit the data together with the curve B. The misorientation of the samples has been, of course, averaged out for both the curves. As shown by the solid curve A, the overall feature of the data is successfully reproduced. A remaining problem is, however, that the magnitude of the isotropic part, $\sim 13\%$ is too small in comparison with $\sim 30\%$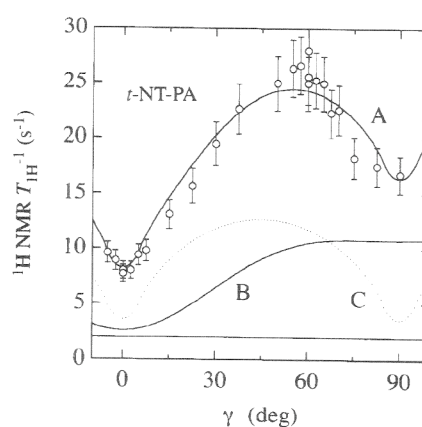 in the second moment as shown in Figure 6.9. One of the possible explanations is that the spectral diffusion is more efficient in the crystalline region than in the amorphous one. If the present interpretation is correct, the relaxation via the spectral diffusion and the localized paramagnetic spins give a sizable contribution, around 30% in trans-NT-PA and $\sim 20\%$ in trans-S-PA at 300 K. Here, note that the small difference of the fitting curves around $\gamma = 90°$ between Figure 6.14 and Figure 3 of [62] is caused by the inclusion of the cross-term between the dipolar and the hyperfine couplings for Figure 6.14.

2.2 Polyparaphenylene

PPP is a typical conjugated polymer with non-degenerate ground states in bond alternation. The crystal structure is orthorhombic/monoclinic similar to PA, but a degree of molecular motion in the crystal in particular the librational motion of the ring is reasonably larger than in the case of trans-PA [2,23].

The linewidth and the second moment of ^{1}H NMR in PPP is plotted in Figure 6.15 as a function of temperature [2,23,28,29]. Noticeable differences from

trans-PA are found in the large temperature dependence of the second moment and a disproportion of the second moment to the square of the linewidth. It is known that the motional narrowing does not affect the second moment [8,11]. Here, note that in the case of rotational motion about the molecular axis (normal to the molecular plane in the case of benzene and the chain axis in the case of PPP) a part of the second moment can apparently be eliminated, in the sense that it is difficult to observe, by a factor of $(3\cos^2\gamma - 1)^2/4$ where γ is the angle of the molecular axis about the axis connected two nuclei [8,11]. However, the librational motion of PPP does not have the case; the in-line (2,3 or 5,6) protons are ineffective because of $\gamma = 0$ and the protons in both sides (2,6 or 3,5) have a contribution only 0.5% of the maximum second moment for the nearest protons. Therefore, the temperature dependence of the second moment should be caused by the lattice expansion but not the rotational motion. In order to discuss the motional narrowing, both the linewidth and the second moment should be studied. In this case, an argument on the motional narrowing only with the second moment is inappropriate. Figure 6.15 demonstrates a deviation from the relation $M_2/(\Delta H_{pp})^2 = 0.143$ at 4.5 K starting below 100 K, which suggests that the motional narrowing takes place at even less than 100 K. Such a narrowing was suggested to be due to a librational motion of the rings [2,28,29]. If $M_2^{1/2} \ll 1/\tau_c$, the motionally narrowed linewidth is expressed as [8,11]:

$$\Delta H \approx \gamma M_2 \tau_c, \qquad (6.4)$$

where M_2 is in units of G^2 and τ_c is the correlation time of motion. The coefficient $\varepsilon = M_2/(\Delta H_{pp})^2$ is expected to increase as motional narrowing takes place, since a relation $\varepsilon \approx 1/\gamma \tau_c \Delta H_{pp}$ holds. At 4.5 K, ε is much smaller than 0.25 for the Gaussian shape, which means the lineshape is flat-top and box-shaped, as discussed in Section 2.1. While, at 300 K it increases steeply to $\varepsilon \approx 0.25$ equal to the Gaussian case and the lineshape would then approach the Lorentzian shape at higher temperatures. As a conclusion, the librational motion can be excited well below 100 K, which is consistent with the activation energy of 2.5 kJ/mole reported for p-terphenyl [84].

The second moment 7.5 ± 0.5 G^2 that is corrected by the same quantity ($+0.5$ G^2) as the PA case (see, Section 2.1.1) can be compared with that calculated based on the lattice parameters at 300 K shown in Table 6.2 [39,49–51] for the structure in Figure 6.16. This figure demonstrates a typical dependence of M_2 as functions of Θ_{twist} and ϕ_{set}. The total second moment
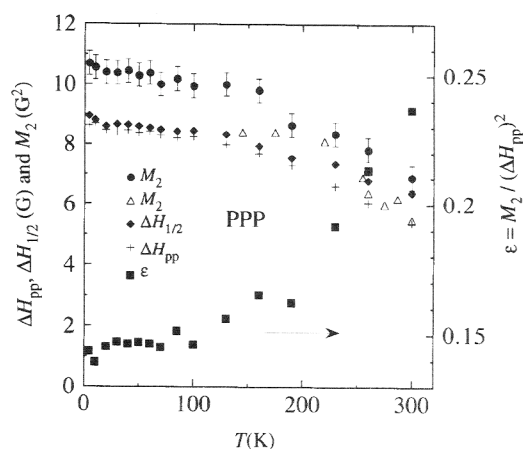
Figure 6.15. The peak-to-peak width ΔH_{pp} (+[23]); full width $\Delta H_{1/2}$ ($\blacklozenge$ [23]); the second moment M_2 of ^{1}H NMR ($\triangle$ [2,28,29], $\bullet$ [23]) and $\varepsilon = M_2/(\Delta H_{pp})^2$ ($\blacksquare$ [23]) in polyparaphenylene are plotted versus temperature. Change of ε means change of lineshape.
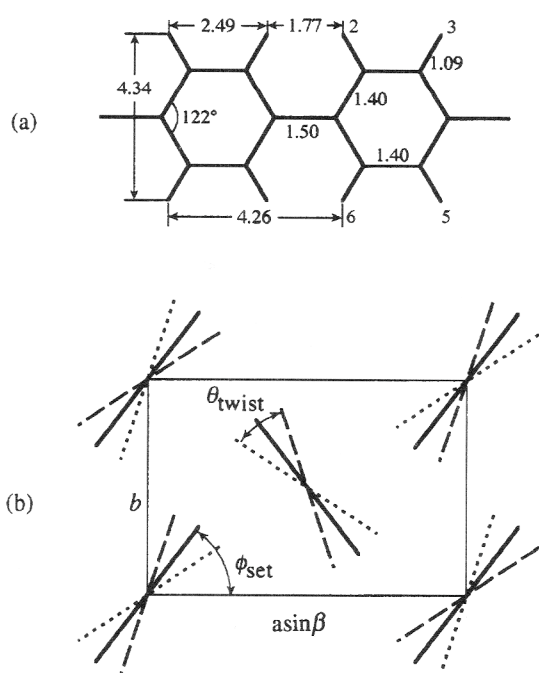
Figure 6.16. The simplified model structure for PPP: (a) the model structure of single chain; (b) the orthorhombic/monoclinic structure [49,51]. At low temperature each ring is twisted alternately by θ_{twist} around the setting angle ϕ_{set} to avoid steric hindrance between the protons facing each other in the neighbouring rings.

Figure 6.17. The calculated second moment M_2 for PPP [23]. The left half shows the twisted angle θ_{twist} dependence of M_2 at $\phi_{set} = 55°$ and the right half does the setting angle ϕ_{set} dependence of M_2 at $\theta_{twist} = 30°$. The broken curve shows the second moment due to the intrachain interaction and the dotted curve (Baughman *et al* [39,50]) and the dash-dot curve (Teraoka and Takahashi [51]) represents the second moment due to the interchain interaction. The sum of these is plotted as 'Total' shown by the solid curve (Baughman *et al* [39,50]) and the dash-three dots curve (Teraoka and Takahashi [51]). The hatched area indicates the expected range of the experimental data for PPP at 300 K.

shows a minimum around $\theta_{twist} = 40$–$45°$. The structure by Baughman *et al.* [39,50] gives a compatible value with the hatched area in Figure 6.17, yielding $\theta_{twist} = 45 \pm 5°$ and $\phi_{set} = 55 \pm 5°$ that suggest each ring librates between double well potentials separated by 45°. Here, Teraoka and Takahashi [51] studied PPP polymerized with $MoCl_5$, while $AlCl_3$-$CuCl_2$ is used in [23], and the second model by Kovacic *et al.* [49], $c = 2.46$ and $\beta = 100°$ was not studied in [23]. Thus,

the obtained $\theta_{twist} = 45°$ is remarkably larger than 17–26.6° reported for *p*-terphenyl and *p*-quaterphenyl [85–87]. With decreasing temperature, the interchain part increases in particular at the larger θ_{twist} region, resulting in a decrease of θ_{twist} where the second moment reaches its minimum. The observed second moment usually coincides with its minimum value, since the potential energy also takes its minimum value around a configuration which gives the largest 'minimum separation' of the protons.

Here, the second moment studies in the conducting polymers are summarized. To discuss structures using a

Table 6.2. The various lattice parameters of the model structures for PPP. See Fig. 6.16 for the notation, c is the chain direction, a is taken as the longest axis

References	a (Å)	b (Å)	c (Å)	Space group	ϕ_{set} (°)	θ_{twist} (°)	β (°)
Kovacic *et al* [49]	7.81	5.53	4.20	—	—	—	
			4.26	$P2_1/a$			100
Baughman *et al* [39,50]	8.16	5.66	4.26	$P2_1/a$	—	—	—
Teraoka *et al* [51]	7.78	5.62	4.26	$P2_1/a$	—	—	79
Weber, Helmle [2,28,29] (in the low T phase)	7.81	5.53	2.425	$P2_1/a$	55 ± 2	30 ± 4	95 ± 5
Mizoguchi *et al* [23]	8.16	5.66	4.26	$P2_1/a$	55 ± 5	45 ± 5	—

second moment it is necessary to have a basic knowledge of the structure; a definitive conclusion cannot be given with only the second moment as it can with x-ray and electron diffraction studies. In other words, the second moment study is useful to distinguish the rationality of a variety of conclusions given by diffraction studies. In the present case the second moment rules out the possibility of the structure by [4,45] for *trans*-PA and proposes the setting angles and the twisting angle both for *trans*-PA and PPP.

The oriented sample provides another parameter, the angle, which gives information on the amorphous region inevitable in the conducting polymers. In this case also the knowledge of the mechanism for ESR T_1, T_2 and NMR T_1 is useful. Furthermore a Pake doublet experiment to determine distances between the special pair of nuclei carrying nuclear magnetic moment is important, and is mentioned in the next section.

2.3   Other topics

If a special pair can be prepared, the precise distance between the nuclei in the pair can be obtained by analyzing the splitting of the resonance magnetic field due to the dipolar interaction. One of the important parameters in polyacetylene is the bond distance and alternation between the neighbouring carbon nuclei, since relates to the energy band-gap. Such an experiment has been done using high-resolution ^{13}C nutation NMR [88]. To provide a lone pair of ^{13}C, a mixture of 4% of doubly ^{13}C-enriched acetylene and 96% natural abundant (99% ^{12}C) acetylene were used as a source of synthesis. From typical splitting of the Pake doublets the C−C bond distances were determined as 1.37 Å for *cis*-PA and both 1.36 and 1.44 Å for *trans*-PA. The unique distance for *cis*-PA suggests a simple connection of acetylene molecules upon polymerization. The two different, single and double bonds for *trans*-PA requires the presence of the neutral soliton that exchanges the double bond to the single bond by passing through the pair. This conclusion was confirmed by the 2D NMR [89]. This magnitude of the bond alternation for *trans*-PA is comparable with 0.035 Å obtained by the x-ray diffraction analysis [43,47].

Polyaniline (PANI) has complicated chemical structures that are postulated [90,91]. To study such postulated structures Kaplan *et al.* [92] and Richter *et al.* [93] made solid state ^{13}C and ^{2}D NMR [92] and ^{15}N NMR [93] and an emeraldine base (EB), a leucoemeraldine base (LEB) and an emeraldine hydrochloride (ES), and revealed that EB is an alternating co-polymer of reduced and oxidized repeat units. Kaplan *et al.* [92] also pointed out that the primary chain motion is 180 degree flips of rings at temperatures from 300–400 K. Richter *et al.* [93] reported no observable signal from the chain ends within the sensitivity.

Recently, Kenwright *et al.* [94] improved the resolution of ^{13}C and ^{15}N NMR spectra with use of the solution state NMR in PANI and found that the majority of the material present in LEB and EB had the previously postulated structures, but that defects in the postulated structures might be present at concentrations up to 5 mol% of the repeat units. The nature of such defects could not be identified, but possibilities of end groups of the chain, an irregular distribution of amine and imine nitrogens along the chain, as well as the possibility of chain branching at amine nitrogens are assumed [94].

3   WAVEFUNCTION OF ELEMENTARY EXCITATIONS BY ENDOR/ESR

3.1   Double resonance

In this section, we focus on ENDOR (Electron Nuclear Double Resonance) and related techniques that are useful to observe spin density distributions of paramagnetic excitations in conjugated polymers. ENDOR detects the magnetic resonance of nuclear spins near an electron spin [95–97]. The observed ENDOR frequencies directly give the hyperfine coupling constants (hfc's) from which the spin density distribution can be determined. In the case of an electron spin of $S = 1/2$ interacting with a proton nuclear spin of $I = 1/2$, the ENDOR frequency is given by the following equation.

$$\nu_\pm = [\sum_i (\nu_p \pm A_{ii}/2)^2 l_i^2]^{1/2}. \tag{6.5}$$

Here ν_p, A_{ii} and l_i show the free proton frequency, principal tensor component along the ith axis and the direction cosine of the external magnetic field along this axis, respectively. This equation reduces to the conventional form,

$$\nu_\pm = |\nu_p \pm A_{ii}/2|, \qquad \text{for } i = x, y, z \tag{6.6}$$

when the external field direction is parallel to one of the principal axes of the hyperfine tensor. The second term of the right-hand side shows the frequency shift due to the hyperfine field and the $\pm$ sign corresponds to up and down electron-spin orientation. The major advantage of ENDOR over ESR in determining hfc's is that

for N nuclear spins of $I = 1/2$ interacting with an electron spin, only N pairs of lines are observed for ENDOR through (6.5) or (6.6), while 2^N hyperfine lines result in ESR spectra that make ESR analyses difficult. Another advantage is that the frequency resolution of ENDOR is that of NMR, which is much higher than that of ESR in solids.

In the case of the π-electron, the spin density ρ on the carbon $p\pi$ orbital gives rise to the hyperfine coupling of magnitude $-\rho \mathbf{A}$ with the proton bonded to the carbon atom [5]. Here $\mathbf{A}$ is the hyperfine tensor characteristic of the π-electron, whose principal components are given as follows.

$$A_{xx} = -(1 - \alpha)A, \, A_{yy} = -(1 + \alpha)A \text{ and } A_{zz} = -A.$$
(6.7)

Here A is the so called McConnell's constant, having the magnitude of 56–84 MHz (or 20–30 gauss in the magnetic field unit), α represents the relative magnitude of anisotropic coupling. The definition of the coordinate axes are shown in Figure 6.18, where the x and z-axes are taken parallel to the C–H bond axis and the $p\pi$ orbital axis, respectively. Among these tensor components in (6.7), A_{yy} has the largest component. The y-axis becomes the conjugated chain axis in the case of *trans*-polyacetylene [7,54,98].

By combining (6.6) and (6.7), the ENDOR frequencies of the proton of the carbon site having the spin density ρ are given as,

$$v_{\pm} = v_p \pm (1/2)\rho A_{ii}, \qquad i = x, y, z \qquad (6.8)$$

for the principal axes. Thus if we observe the distribution of ENDOR frequency shifts, we can determine the spin density distribution.

The ENDOR signals are detected as the change of the ESR signal when the frequency of the RF field applied to the sample in the ESR cavity coincides with one of the above frequencies. The change in the ESR signal is caused either by a ΔT_1 mechanism or the

packet-shifting mechanism in the cw-ENDOR detection method, where the ESR signal is detected by a conventional cw-ESR spectrometer [95–97]. ENDOR signals can be also detected by pulsed ESR spectrometers and various pulse schemes have been devised to observe ENDOR transitions by their effects on the echo signal formation [99].

As pointed out above, the most accurate and reliable information obtained by ENDOR is the resonance frequency that directly gives the hyperfine coupling constant. In this respect, the frequency-derivative ENDOR spectra obtained by cw-ENDOR detection by employing the frequency modulation scheme, are particularly important because of high-frequency resolution. Combined with ENDOR-induced ESR, the maximum ENDOR frequency, important in identifying the peak value of the spin density distribution, can be determined very accurately [7]. Specific examples are discussed in the cases of solitons in polyacetylene and polarons in poly(paraphenylene vinylene) in Sections 3.2 and 3.3.

It is seen from (6.5) or (6.6) that the sign of the hyperfine coupling cannot be determined from the ENDOR spectra. The sign determination is possible by use of so called TRIPLE (electron nuclear-nuclear triple resonance) technique [96,97]. This method applies to cases of more than two nuclear spins. ENDOR transition of one nuclear spin is observed while the ENDOR transition of another nuclear spin is saturated by employing another RF frequency source. The relative sign of hyperfine couplings of these two nuclear spins can be determined whether the pumping of the ENDOR transition of another nuclear spin enhances or negatively enhances the ENDOR signal of the first nuclear spin. TRIPLE experiments are performed using cw or pulsed ESR spectrometers. Examples are discussed in the case of the soliton in polyacetylene in Section 3.2.

3.2 Polyacetylene

3.2.1 Soliton wavefunction and electron correlation

Figure 6.19 shows the spin density distribution of the soliton in the case of finite electron correlation. The filled circles represents individual carbon sites. The spin density distribution reflects the soliton profile, the observation of which is essential in examining the reality of the soliton. It should be pointed out that the most important and clear information relating to the
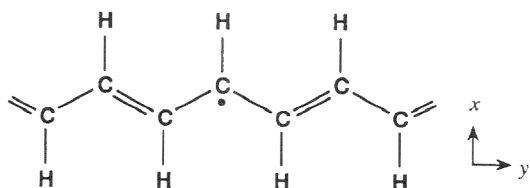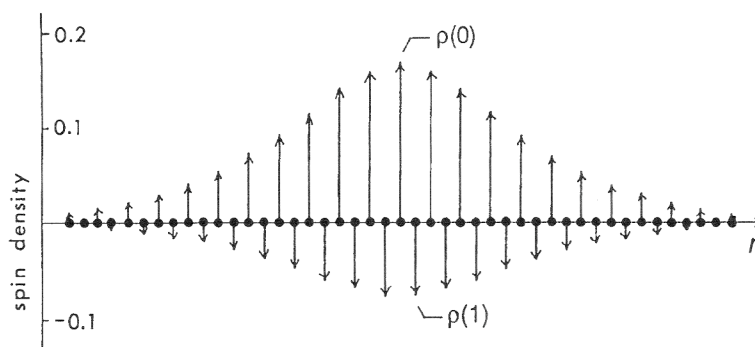

Figure 6.18. Soliton in *trans*-polyacetylene. The definition of the molecular axes is also shown where the x-axis and the z-axis are taken parallel to the C–H bond axis and the $p\pi$ orbital axis, respectively.

Figure 6.19. Spin density distribution of the soliton in the case of a finite electron correlation.

soliton profile is the maximum spin density $\rho(0)$ at the centre of the soliton. The quantity is nearly inversely proportional to the spatial extension of the soliton.

Another important piece of information contained in the soliton spin distribution is the effect of electron correlation. In the original Su-Schrieffer-Heeger model, where electron correlation is neglected, the spin density appears at every even carbon site from the centre of the soliton [100]. It is well known that this results from the non-bonding character of the wave function of the soliton. On the other hand, in the case of finite electron correlation, positive spins grow at even sites and negative spins are induced at odd carbon sites, for which $\rho(\pm 1)$ gives the peak value [101]. The magnitude of these excess spin densities directly provides the strength of the electron correlation energy of the system. Thus the observation of the excess densities, in particular the detection of negative spin densities crucially probes the occurrence of electron correlation in the system, that is a fundamental problem. This is another important aspect in the study of the soliton spin density.

As schematically shown in Figure 6.18, an unpaired π-electron is associated with the soliton in *trans*-polyacetylene. In this case, ENDOR spectroscopy can directly measure the spin density distribution of the soliton by the study of hyperfine coupling [98], according to the discussion in the preceding section. In fact ENDOR observations of the spin density distribution close to those predicted theoretically in the case of finite electron correlation have been reported independently for stretch-oriented *cis*-rich samples prepared by the conventional Shirakawa method [102–105] and for stretch-oriented *trans* samples prepared by the Durham route [99,106,107].

The first clear soliton shape, which has a comparable extension to theoretical prediction, has been observed by ENDOR using stretch-oriented *cis*-rich samples at 4 K [102–104]. In *cis*-rich samples, the motion of the soliton in *trans* segments in the *cis* matrix tends to be frozen at lower temperatures, avoiding the motional averaging of the intrinsic hyperfine coupling observable in the static limit [53,54,108]. Enhanced spectral resolution in this study with the use of stretch-oriented *cis*-rich samples has made it possible, for the first time, to resolve a spectral turning point in the stretch direction and it has been postulated to be intrinsically associated with the negative spin sites arising from electron correlation effect [102,103]. The occurrence of negative spin sites has been predicted [101], as pointed out above, and its importance has been discussed in the ENDOR analysis [98] as well as in the ESR simulation study of the soliton profile [109]. The validity of the interpretation has been further confirmed by the ENDOR studies using ENDOR-induced ESR [104] and electron-nuclear-nuclear triple resonance techniques [105].

ENDOR frequency determination with the aid of ENDOR-induced ESR in *cis*-rich samples gives the half-width of the spin distribution of 18 carbon sites and the ratio of the peak value of the negative density to that of the positive density of $\rho(1)/\rho(0) \approx 0.44$ [104,105]. Similar results to those in *cis*-rich samples, that is similar spectra with resolved structures for the stretch direction and similar spectral frequencies, have been reported for stretch-oriented *trans*-polyacetylene prepared by the Durham route using pulsed ENDOR techniques [99,106,107]. The unpaired electrons observed in Durham samples were conjectured to be trapped solitons from nearly temperature-independent ENDOR spectra. In the studies of this system the first successful application of TRIPLE resonance in polyacetylene has been reported [99,107]. Readers can find reviews on the results of Durham samples [2,99] as

well as those of other early ENDOR results [110]. In this chapter, we focus on the ENDOR results obtained in *cis*-rich samples [7].

3.2.2 ENDOR spectra of the soliton in stretch-oriented cis-rich (CH)$_x$ at low temperatures

Prior to ENDOR analyses of the soliton spin density, the π-electron nature of the soliton has been confirmed from the studies of the anisotropy of ESR and ENDOR spectra in stretch-oriented samples, [54,98] by noticing that π-electron shows characteristic anisotropy of g value and hyperfine coupling in solids [5]. The results have justified the use of the theory of π-electron in subsequent ENDOR and other magnetic-resonance analyses.

Figure 6.20 shows the orientation dependence of the frequency-derivative ENDOR spectra of a 190% stretched *cis*-rich sample at 12 K [104]. The *trans* concentration of the sample was measured to be less than 10% by the infra-red method. Since the spectra are nearly symmetrical around the free proton frequency,
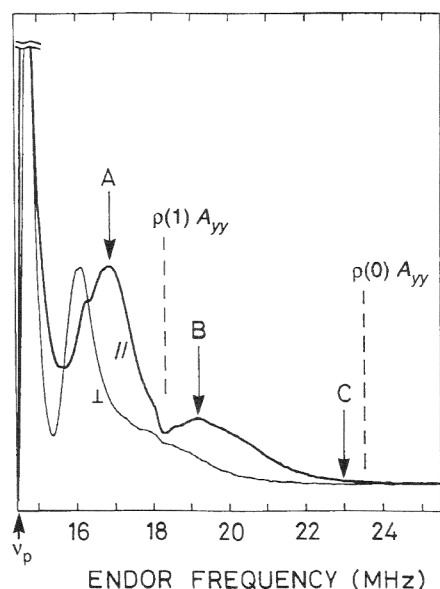

Figure 6.20. Anisoptropy of the frequency-derivative EN-DOR spectra of a stretch-oriented *cis*-rich sample for v_+ branch [104]. The external field is parallel and perpendicular to the stretch direction of the sample for the thick- and thin-line curves, respectively. Positions A–C show the frequencies at which ENDOR-induced ESR are shown in Figure 6.22. Dashed lines show the frequencies corresponding to the hyperfine tensor components as indicated. (after ref. [104])

only the frequency region higher than v_p is shown. The spectra with the external field parallel and perpendicular to the stretch direction are marked with $\parallel$ and $\perp$, respectively. The characteristic anisotopies of the spectra have been shown to be consistent with the spin density distribution of the form shown in Figure 6.19. The functional form of the spin density is given as follows:

$$\rho(n) = \begin{cases} \rho_1 \ \text{sech}(n/l) & n = \text{even} \\ -\rho_2 \ \text{sech}(n/l) & n = \text{odd}, \end{cases} \quad (6.9)$$

Here $\rho_1 = \rho(0)$ and $-\rho_2 \approx \rho(1)$ characterize the peak values of the positive and negative spin sites, respectively, and l represents the width of the soliton.

There are a few important features of the spectra in Figure 6.20. Firstly, it is clearly seen that the spectrum of the stretch direction shows the larger coupling. This is a direct consequence of the anisotropic coupling of the π-electron, which should show the maximum value along the chain axis, as pointed out in the preceding section. In stretch-oriented samples, the chain axis may be preferentially oriented along the stretch direction and thus the largest coupling is expected when the external field is parallel to the stretch direction. Therefore the observed ENDOR anisotropy provides direct evidence for the π-electron nature of the soliton. Secondly, the broad distribution of spectral frequency up to about 24 MHz, directly shows the distribution of the spin density on the conjugated chain from (6.8). As discussed below, the maximum ENDOR shift determines the value of the peak spin density $\rho(0)$. The sharp peaks around v_p, denoted as matrix signals, are signals coming from the protons of neighbouring chains and can be neglected in the discussion of the spin density determination.

Another striking feature of the spectra is the appearance of a distinct structure at 18.4 MHz in the spectrum of the stretch direction. Care is necessary in determining the frequency of the above structure, because a small structure overlaps at 18.05 MHz (the sum frequency of the proton and ^{13}C nuclear frequencies) at low temperatures due to the interaction between the proton and ^{13}C nuclei, to be discussed later in this section. This structure has been proposed to be associated with the peak spin density of the negative spin sites $\rho(1)$ ($=\rho(-1)$) as shown in the figure [102,103]. The physical origin of the structure is explained as follows. Figure 6.21(b) shows the ENDOR frequencies of the positive and negative spin densities expressed by (6.9) for the y-axis, which are the ENDOR frequencies of the parallel direction in the
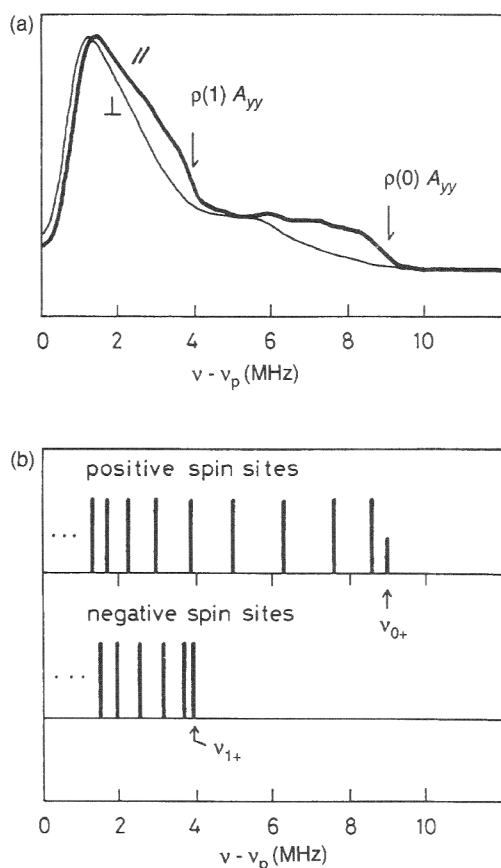
Figure 6.21. (a) Calculated ENDOR lineshapes of the soliton spin density for the parallel and perpendicular directions of preferentially oriented polymer fibrils for the v_+ branch. The abscissa shows the ENDOR frequency measured from v_p. The arrows show the frequencies of corresponding hyperfine tensor components of the y-axis as indicated. (b) Explanation of the origin of the spectral turning points of the parallel direction. Upper and lower stick diagrams show ENDOR frequencies along the chain axis (y-axis) for the positive and negative spin densities of Figure 6.19. These individual components are washed out in partially aligned systems, but the distinct spectral turning point arises at the frequency v_{1+}, associated with the peak value of the negative spin density $\rho(1)$ (after [103]).

completely aligned limit. Due to the partial alignment of the chain axis, structures expected from the sharp resonance lines of the y-axis are nearly washed out. However, a distinct structure arises at the frequency due to $\rho(1)$ at which the contributions from the negative spin sites start to overlap with those from positive densities [$\rho(0)$, $\rho(\pm 2)$, $\rho(\pm 4)$, $\cdots$], as the frequency goes to v_p from the higher frequency side.

This situation is seen in the calculated ENDOR spectra of a partially oriented system for the soliton spin density, as shown in Figure 6.21(a). More detail is described in [103]. Thus the frequency of the turning point, defined as v_{1+}, is given as,

$$v_{1+} = v_p + \tfrac{1}{2}|\rho(1)A_{yy}| \qquad (6.10)$$

Since the envelope of the spin density distribution is smoothly varying over the CH chain segments, no such distinct structure is expected from the SSH spin density, without negative spin densities.

3.2.3 Spin distribution parameters by ENDOR-induced ESR

In this respect the confirmation of the fact that the observed structure is associated with the signal of the *single* spin species is essential, otherwise the possibility of the apparent structures arising from the overlapping of ENDOR signals from different spin species is not excluded. The ENDOR-induced ESR technique is especially suited for this purpose. In this method, the frequency of the RF wave for the ENDOR transition is fixed at a particular value and the ENDOR signal intensity is recorded as a function of the external magnetic field. This provides the ESR spectrum of the spin species giving rise to the ENDOR signal at the fixed frequency. The top and the second curves in Figure 6.22 show ENDOR-induced ESR signals obtained at the positions marked by A and B in the ENDOR signal of the stretch direction in Figure 6.20. Both curves are identical with each other and also coincide with the cw ESR spectrum. Similar ENDOR-induced ESR signals were confirmed for other regions of the ENDOR spectrum. Therefore, it is concluded that the above distinct structure of the stretch direction is associated with the same spin species as that observed by cw ESR. These facts provide strong support for the occurrence of the negative spin sites in the system.

Thus the observed frequency of v_{1+} of 18.4 MHz determines $\rho(1)A_{yy}$ to be 7.9 MHz using (6.10) with $v_p = 14.43$ MHz in the present case. As for the sign of the spin density, TRIPLE resonance provides direct evidence that the spectral turning points are associated with the negative sign of the spin density, to be described later.

The other important quantity determined by experiment is the maximum ENDOR frequency of the
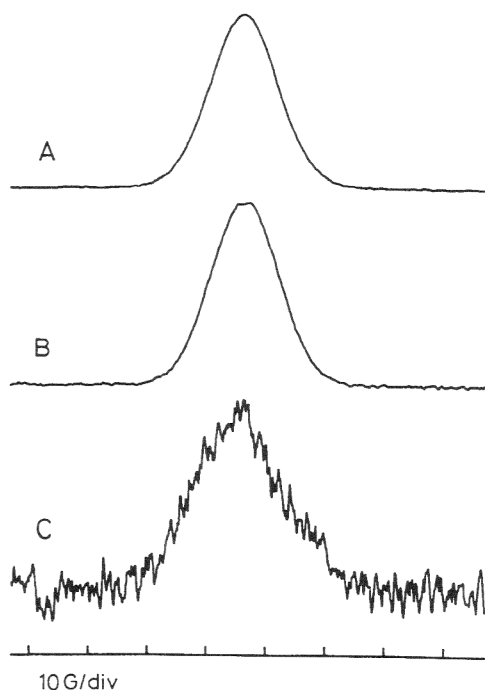
Figure 6.22. ENDOR-induced ESR signals at the ENDOR frequencies shown in Figure 6.20 as: A(16.8 MHz); B(19.2 MHz); and C(23.0 MHz). (after [104])

system, defined as v_{0+}. Obviously, this quantity gives the peak spin density $\rho(0)$ and is given as,

$$v_{0+} = v_p + \tfrac{1}{2}|\rho(0)A_{yy}| \qquad (6.11)$$

It should be pointed out that this quantity gives the direct measure of the width of the spin distribution, regardless of the detail of the distribution form, because $\rho(0)$ is nearly inversely proportional to the full width of the half-maximum of the spin density distribution. [100,111].

ENDOR-induced ESR is also indispensable in determining the maximum ENDOR frequency to high accuracy. This quantity is determined from the wing of the spectra. In Figure 6.20 it is seen that the wing in the spectrum of the stretch direction nearly reaches 24 MHz; however, the exact determination may suffer from a possible deviation of the background level. The ENDOR-induced ESR technique plays an important role in the confirmation of the wing, because the maximum frequency is obtained as the largest frequency where the ENDOR-induced ESR signal can be detected. The bottom curve in Figure 6.22 shows the ENDOR-induced ESR signals obtained at the frequen-

cies marked by C($v_+ = 23$ MHz) in Figure 6.20, which shows that the wing is still present at 23 MHz. Because these spectral regions are mainly associated with the fraction of the spins with their y-axis completely aligned along the stretch direction, in a partially oriented system, the resultant ENDOR-induced ESR signal comes close to that for the y-axis, which has a larger linewidth than that of cw-ESR [102,103]. Using this method, an ENDOR frequency as large as 23.4 MHz was confirmed. Using (6.11) with $v_p = 14.43$ MHz in the present case, $\rho(0)A_{yy}$ is obtained as about 18.0 MHz.

Thus the ratio $\rho(1)A_{yy}/\rho(0)A_{yy} = \rho(1)/\rho(0)$, is determined to be -0.44, because $\rho(1)$ is negative. This quantity is the direct measure of the strength of the electron correlation in the system. The absolute values of $\rho(0)$ and $\rho(1)$ in (6.9) depend on the magnitude of $A_{yy} = -(1 + \alpha)A$. Here, as introduced in (6.7), A is the so called McConnell's constant which represents the magnitude of isotropic coupling and typically takes a value between 20 and 30 gauss (or between 56 and 84 MHz in the frequency unit) and $\alpha \sim 0.5$, represents the relative magnitude of the anisotropic coupling. Although the exact value of A in polyacetylene is not known yet, the average value of $2\pi A/\gamma_e = 25$ gauss is used for the later discussions. This value is in fact close to the theoretical estimation of $2\pi A/\gamma_e = 26$ gauss in polyacetylene by White $et\ al.$, using the local-density-functional method [112]. Using $2\pi A/\gamma_e = 25$ gauss and $\alpha = 0.5$, that is $A_{yy} = 105$ MHz, the spin density values are obtained as $\rho(0) = 0.17$ and $\rho(1) = -0.075$. Once the values of $\rho(0)$ and $\rho(1)$ are given, the value of l in (6.9) is determined by the relation which requires the total sum of the positive and the negative spin densities to be unity. This condition gives $l = 6.7$, which correpsonds to the full width at half maximum of the spin density of 18 lattice constants. The validity of the parameter values is further examined by the ESR simulation method [109] by confirming that the obtained spin desnity well reproduces the observed ESR spectra. Thus the obtained parameter values are summarized in Table 6.3. It should be also pointed out that the above value of $\rho(0)$ has been shown to be consistent with the estimated value of $\rho(0)$ of the soliton in $trans$-polymer from the analysis of the frequency dependence of the ESR linewidth, to be discussed in section 4.3.3.

The values of $\rho(0)$ and $\rho(1)$ and their ratio are in comparable magnitude with those predicted theoretically for a moderate on-site Coulomb energy of several eV [1,112–115]. Moreover, they are quantitatively reproduced by the calculation incorporating the

Table 6.3. Spin density distribution parameters of the soliton in polyacetylene determined from the ENDOR spectra of stretch-oriented *cis*-rich samples at low temperatures with the aid of ENDOR-induced ESR measurements [104]

Observed values[1]			Parameters of (6.9)			Half width[2]
$\rho(0)$	$\rho(1)$	$\rho(1)/\rho(0)$	$\rho 1$	$\rho 2$	l	l_{hw}
0.17	0.075	0.44	0.17	0.076	6.7	18 CH sites

[1]Values of $\rho(0)$ and $\rho(1)$ are calculated from the observed coupling values of $\rho(0)A_{yy} = 18.0$ MHZ and $\rho(1) A_{yy} = 7.9$ MHz. $A_{yy} = (1+\alpha)A$ is the y-axis component of the hyperfine tensor of π-electron. $A = 70$ MHz (or 25 gauss in field units) and $\alpha = 0.5$ are assumed.
[2]Full width at half maximum of the distribution.

fluctuation effect in the Hartree–Fock approximation by Yonemitsu *et al.* [111]. According to their results, on-site and near-neighbour Coulomb interactions of $U = 1.6t_0$, $V = 0.8t_0$ fit the observed results well by assuming a dimensionless electron–phonon interaction parameter of $\lambda = 0.1$. Here t_0 shows the transfer integral whose magnitude is ~ 3 eV in polyacetylene.

3.2.4 TRIPLE resonance

Thus the remaining important problem in the ENDOR analysis of the soliton spin density is to confirm that the intrinsic structure observed in the ENDOR spectrum in the stretch direction is really associated with the negative sign of the spin density, as indicated by the above analysis. This point can be adequately studied by electron-nuclear-nuclear triple resonance (TRIPLE) technique [96,97] which can detect the existence of the spin densities of opposite sign in the system. In TRIPLE measurements, additional rf pumping is applied to normal ENDOR experiments. Here we confine our discussion to the case of the observing and pumping frequencies belonging to the same ENDOR branch, for example, the v_+ ($> v_p$) branch of the ENDOR frequencies. In this case, the ENDOR intensity decreases by pumping when the observing and pumping frequencies arise from spin densities of the same sign. On the other hand, ENDOR intensity *increases* by pumping when the observing frequency arises from spin density of the opposite sign. Thus this effect can be used to distinguish the relative signs of spin densities.

According to the discussion of Figure 6.21, the ENDOR frequency region higher than the turning points, i.e. $v > v_{1+}$, arises solely from the positive spin sites. Thus, if we set the pumping frequency at this region, the intensity due to the positive sites will decrease while that due to the negative sites will increase in v_+ branch, resulting in an enhanced increment of the ENDOR intensity at v_{1+}.

Figure 6.23 shows the comparison between the ENDOR spectrum (dotted line) along the stretch direction with the TRIPLE signal, with pumping at 18.3 MHz in the range $v > v_{1+}$, as indicated by an arrow. Both the ENDOR and TRIPLE signals were recorded without frequency modulation to detect directly the change of signal intensity caused by the TRIPLE effect. In this case $v_{1+} = 17.9$ MHz with $v_p = 14.0$ MHz. The detail of experimental condition is given in [105]. As clearly seen from Figure 6.23, the expected change of ENDOR intensity is observed, that is, the TRIPLE signal shows an enhanced increment at the turning point. While the TRIPLE intensity is lower than the ENDOR intensity for most of the higher frequency region, it is higher in a certain range for $v_p < v < v_{1+}$. This situation never happens without the presence of the spin density of opposite sign compared with that at the pumping frequency. Further details are given in [105]. These TRIPLE observations establish that the negative spin densities are associated with the
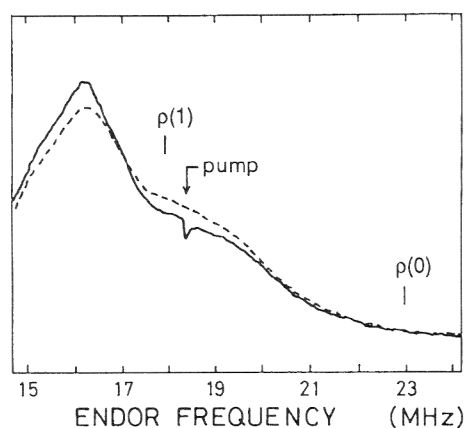

Figure 6.23. Detailed comparison of TRIPLE and ENDOR spectra at 4 K in a 190% stretched *cis*-rich polyacetylene with the external field parallel to the stretch direction [105]. The solid line shows the TRIPLE signal obtained with pumping at 18.3 MHz and the dashed line shows the ENDOR signal obtained without pumping. (after [105])

turning point as proposed in the preceding ENDOR works of stretched *cis*-rich samples.

In the case of *cis*-rich polyacetylene, the narrowing of ESR and ENDOR spectra observed at higher temperatures [54,98] clearly shows the presence of the motion of spins at higher temperatures, indicating that the spins in *cis*-rich samples at low temperatures are trapped solitons [53,108]. This picture is discussed in more detail in section 4. It is therefore concluded that the ENDOR studies of polyacetylene described in this section provide strong evidence for the existence of the soliton through the direct confirmation of its spin density distribution.

As pointed out in [103], the small structures due to the spin densities other than $\rho(0)$ and $\rho(1)$, such as $\rho(\pm 2)$, $\rho(\pm 4)$, etc. are expected in the spectra, that can be recognized as weak structures in the calculated spectrum along the stretch direction in Figure 6.20. These structures, if detected, may be useful in determining the functional form of the spin distribution. In this respect, it is interesting to notice that the detailed frequency-derivative spectral lineshape along the stretch direction shown in Figure 6.20 has certain weak deviations from the monotonic variation of the lineshape for the $v > v_{1+}$ region. These deviations may be related to the relevant structures. Of course, extreme care would be necessary for their unique assignment, which will be assisted by the further improvement of the resolution, for example, using highly-oriented samples developed recently.

3.2.5 *cis*-rich ($^{13}CH)_x$

For the rest of this chapter we compare the above results with other ENDOR studies of polyacetylene. A spin density much more delocalized than that of the soliton theory was proposed from the studies of unoriented ^{13}C-enriched *cis*-rich sample [110,116,117]. The proposed spin density consists of only two kinds of spin densities: 0.06 and −0.02, the results being quite different from those obtained in stretched *cis*-rich samples. The small magnitude of the proposed spin density of $\rho(0) = 0.06$ could result from the fact that the apparent frequency span of the ^{13}C-enriched system, giving v_{0+} is much smaller than that of the pristine system. Proposed spin densities were deduced by the assignments of the structures of the observed lineshape to ^{13}C or proton hyperfine components. Later comparison between pristine and ^{13}C-enriched systems, however, revealed that the structures of the spectra of ^{13}C-enriched system resulted from the

overlapping of the second harmonic signal of ^{13}C nuclear frequency and other signals at frequencies related to ^{13}C and proton nuclear Larmor frequencies [105,118,119].

Figure 6.24 shows the temperature dependence of the frequency-derivative ENDOR spectra of an unstretched ^{13}C-enriched *cis*-rich sample. Spectra show a clear temperature dependence, where the structures of the lineshape become more prominent as the temperature is lowered. Some structures clearly show the feature of single resonance lines. The spectral lineshapes at higher temperatures are close to those reported in [116]. The detailed measurements of the frequencies of these signals have revealed that the frequencies of the structures are given by the multiple or fractional sum or difference of free proton and ^{13}C nuclear Larmor frequencies, v_p and v_c, as marked in the figure.
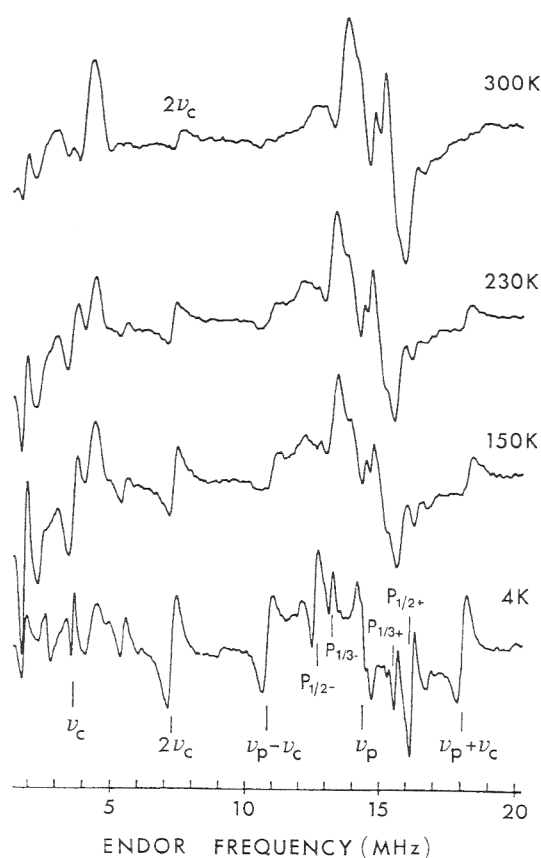

Figure 6.24. Temperature dependence of the frequency-derivative ENDOR spectra in an unstretched ^{13}C-enriched *cis*-rich polyacetylene containing 10% *trans* isomer. v_p and v_c show proton and ^{13}C nuclear Larmor frequencies, respectively (after [105]).

For example, the structure around 7.3 MHz, which was assigned to the spectral turning point due to a ^{13}C hyperfine tensor component in [116], has been found to be the second harmonic of the ^{13}C frequency, $v_c + v_c = 2v_c$. This has been confirmed from the detailed field dependence of the resonance frequency of this line [105]. If the line is assumed to be a $+$ branch of the ^{13}C ENDOR line as in [116], the shift of the resonance frequency due to the field difference should be equal to the shift of v_c. This is because the frequency of the ENDOR line is given by the following equation as discussed in section 3.1,

$$v_\pm = v_c \pm \tfrac{1}{2} A_c. \qquad (6.12)$$

Here $\pm$ shows the two branches of the ENDOR frequency and A_c shows the hyperfine coupling constant of the ^{13}C nuclear spin. In the course of the study of the shift of the structure it has been found that the frequency of this line is exactly the second harmonic of the ^{13}C frequency, $2v_c$ [105,118,119].

Two other prominent lines at 4 K are those around 11 and 18 MHz, and structures due to these lines at higher temperature were assigned to a pair of proton ENDOR lines in [116]. The frequencies of these lines have been found to be the difference and the sum of v_p and v_c, that is, $v_p - v_c$ and $v_p + v_c$ as shown at the bottom of Figure 6.24. These sums or differences of nuclear frequencies can arise from nuclear dipolar coupling in a ^{13}C–H pair in magnetic resonance [11]. Similary, $2v_c$ can arise from a ^{13}C–^{13}C pair. Although the detailed mechanism of the observation of these transitions in ENDOR is not clear yet, ENDOR intensity may be de-saturated at these frequencies by the cross-relaxation effects between the nuclear energy levels of ENDOR and these multiple NMR transitions of the free nuclear spins around the soliton. Acutally, the phases of these lines correspond to 'holes' in the spectra.

There are also other sharp lines at 4 K and they may be related to the above transitions because of the similarity of the temperature and rf power dependence. The frequencies of these lines have been found to be shifted either from v_p or v_c by fractional integers of v_c. For example, the prominent lines marked by $P_{1/2\pm}$ correspond to the frequencies of $v_p \pm (1/2)v_c$ according to the notation in [105]. A possible explanation of the observed frequencies proposed in [105] is that the cross-relaxation occurs between the following multiple ENDOR and nuclear transitions.

$$m(v_p + \tfrac{1}{2}A') = mv_p + nv_c. \qquad (6.13)$$

The left-hand side represents the multiple ENDOR transitions and the right-hand side shows the multi-quantum nuclear transitions involving nuclear spin clusters. If we see $m = 2$ and $n = 1$, for example, $v_p + (1/2)A'$ becomes $v_p + (1/2)v_c$, giving $P_{1/2+}$ and $m = 3$ and $n = 1$, for $v_p + (1/3)v_c$, giving $P_{1/3+}$. Of course, intensities of the lines become weaker for higher-order transitions as seen in the figure.

These overlapping structures mask the intrinsic ENDOR lineshape due to the spin density distribution of the soliton, which can be observed in pristine *cis*-rich samples [105]. The above discussion of multiple and fractional quantum transitions in ^{13}C-enriched samples is further supported by the fact that the structures due to the interaction of ^{13}C and H nuclear spins are also weakly observed in the pristine samples because of the non-zero natural abundance of ^{13}C. Figure 6.25 shows the frequency-derivative ENDOR spectra at 12 K in a 230% stretched pristine *cis*-rich sample, which are the same spectra shown in Figure 6.20 for the v_+ branch. The external field is parallel and perpendicular to the stretch direction of the sample in the upper and lower curves respectively. In the figure, small structures other than distinct turning points at $v_{1\pm}$ are resolved and it has been found that their frequencies exactly
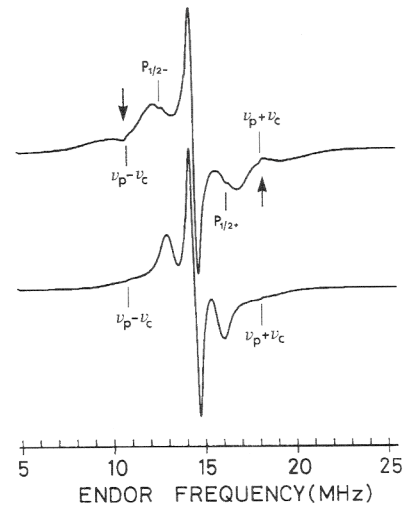
Figure 6.25. Anisotropy of the frequency-derivation ENDOR spectra at 12 K in a 230% stretched pristine *cis*-rich polyacetylene containing 10% *trans* isomer [105]. The external field is parallel and perpendicular to the stretch direction of the sample in the upper and lower traces, respectively. Arrows in the upper curve show the spectral turning point due to $\rho(\pm 1)$. Small structures marked by the symbols arise from the interaction of proton and 1.1% natural abundant ^{13}C nuclei in the pristine system. (after ref. [105])

coincide with those observed in the ^{13}C-enriched system in Figure 6.24 as marked by the corresponding symbols.

According to the above discussion, $P_{1/2\pm}$ and $v_p \pm v_c$ involve the transitions of proton and ^{13}C nuclear spins. This supports the above interpretation that these transitions are related to the interaciton of proton and ^{13}C nuclear spins because the pristine system also contains ^{13}C nuclei with a natural abundance of 1.1%. On the other hand, the second harmonic signal, $2v_c$, which has a comparable intensity to those of $P_{1/2\pm}$ and $v_p \pm v_c$ in the ^{13}C-enriched system in Figure 6.24, completely lacks it in the pristine system, as seen in Figure 6.25. This is reasonably expected because the probability of a ^{13}C $-$ ^{13}C pair in the pristine system is only about 1% of that of a ^{13}C–H pair. From these results it can be concluded that the ^{13}C-enriched system is not adequate for observing the soliton spin density because the lineshape distortion is caused by the overlap of the structures related to multiple and fractional nuclear quantum transitions. Further studies of the origin of these transitions would be interesting.

3.2.6 Stretch-oriented Durham t-(CH)ₓ

On the contrary, the pulsed ENDOR results reported for the stretch *trans*-polyacetylene samples prepared by the Durham route by Mehring and co-workers [99,106,107] coincide well with those of stretched *cis*-rich polyacetylene prepared by the Shirakawa method, described above. The unpaired electrons detected in this system have been conjectured to be trapped solitons from weak temperature dependences of the observed ENDOR spectra. The reported spectral lineshapes of this system are quite similar to those of stretched *cis*-rich samples at low temperatures. That is, the spectra of the stretch direction show similar spectral turning points. The frequencies of the turning points as well as the maximum ENDOR frequency are close to those of *cis*-rich samples. This coincidence results in a similar spin density obtained by the analysis with fitting the observed spectra using simulation methods, although a slightly different functional form, sech^2 form compared with sech form of equation (6.9) has been adopted. The actual difference, however, is not large. For the value of $\rho(1)/\rho(0)$, or ug in their terms, which does not depend on the functional form, they reported $\rho(1)/\rho(0) = 0.43$. This value coincides very well with the value of 0.44 obtained in the *cis*-rich samples using an ENDOR-induced ESR technique. The half-width of the spin distribution is also close to the value in *cis*-rich

samples. The coincidence supports the conjecture that the immobile spins in *trans*-polyacetylene prepared by the Durham route are trapped solitons.

The observed ratio $\rho(1)/\rho(0)$ is an important quantity for estimating the electron correlation energy. The magnitude of the correlation energy estimated using ENDOR results of course depends on the theoretical models fitting the experimental results. For example, a value of $U = 7$ eV with $t_0 = 2.5$ eV is suggested [2,18]. It should be emphasized that $\rho(1)/\rho(0)$ and the absolute value of $\rho(0)$ are important quantities for comparison with theories. In this respect, as already pointed out, the results by Yonemitsu, Ono and Wada, taking into account the fluctuation effect around the Hartree-Fock solution up to the second order, quantitatively reproduce the observed values of $\rho(0)$ and $\rho(1)/\rho(0)$ with $U = 4$–5 eV and $V \sim 2$ eV [111]. The unique determination of the functional form of the soliton spin density distribution may be difficult unless structures due to the spin densities other than $\rho(0)$ and $\rho(1)$ can be resolved [103].

Other studies carried out on Durham polyacetylene by using pulsed ENDOR experiments are those of multi-quantum ENDOR and TRIPLE resonance [99,107]. In particular, the first successful TRIPLE signals in polyacetylene have been reported in this system. An enhancement at the spectral turning point for the pumping at the $v > v_{1+}$ region, similar to those observed in *cis*-rich samples, has been reported. According to the detailed comparison of an ENDOR spectrum with a TRIPLE spectrum shown in Figure 21 of [99], contrary to the results of the *cis*-rich sample in Figure 6.23, the intensity of TRIPLE signal is smaller for the whole region of the v_+ branch. This may be ascribed to larger efficiency of the pumping that can result from different samples and experimental conditions. It is noted that similar situations can occur in the case of *cis*-rich samples depending on the observing and pumping rf power levels. Thus the ENDOR results in *cis*-rich polyacetylene prepared by the Shirakawa method and *trans*-polyacetylene prepared by the Durham method are in good agreement with each other.

3.3 Poly(p-phenylene vinylene) PPV

3.3.1 ENDOR of stretch-oriented undoped PPV

Contrary to the case of *trans*-polyacetylene with a degenerate ground-state structure, most other conju-

gated polymers have non-degenerate ground-state structures. In this case polarons and bipolarons become primary charged excitations. These excitations give rise to characteristic absorptions in the optical, magnetic resonance and other spectroscopic measurements [1,120–125]. Among those polymers with non-degenerate structures, poly(paraphenylene vinylene), PPV, and its derivatives have been extensively studied [120,123–125] in relation to the role of polarons, excitonic polarons and bipolarons in determining the mechanism of the intense electro-luminescence [126,127] observed in this system. These studies as well as others have indicated the existence of the polarons in PPV and the stability and electronic states of them have recently been studied theoretically [128,129]. To identify the existence of polarons, their spatial extension is another essential microscopic quantity. Since polarons carry unpaired electrons, this problem may be adequately studied by ENDOR spectroscopy as in the case of the neutral solitons in polyacetylene.

Recently, the first high-resolution ENDOR spectra of a paramagnetic species existing in the dark state of undoped PPV have been observed using stretch-oriented samples [130,131]. The spectra have shown a clear anisotropy of a π-electron on the conjugated chain. The maximum value of the spin density reaches 0.09, which corresponds to the half-width of the spatial extension of the spin over several phenyl rings. The resemblance between the dark and photo-induced ESR signals at low temperatures strongly suggests that the observed π-electron spins are trapped polarons. Moreover, the observed ENDOR spectra have been well reproduced by a theoretically calculated spin density distribution of a polaron incorporating the effect of electron correlation [132]. In this section the ENDOR results of PPV are discussed as the first typical example of an ENDOR observation of polaron spin distribution in non-degenerate conjugated polymers.

Figure 6.26 shows the chemical structure of PPV. Block letters from A to F show the eight carbon sites in one PPV monomer unit. The principal axes of proton hyperfine coupling of an unpaired π-electron, defined in Figure 6.18, are also shown for two proton sites of inequivalent bond orientations. ESR spectra of stretch-oriented undoped PPV films have shown anisotropic lineshapes with an average g value of 2.003 and a spin concentration of about 1 spin/10^6 PPV monomer units. The observed anisotropic behaviour of the g value and the linewidth, both larger for the stretch direction, are qualitatively similar to those found in stretch-oriented polyacetylene films mentioned in Section 3.2 and
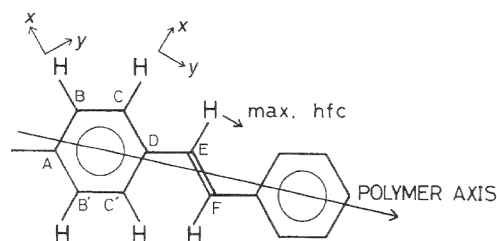
Figure 6.26. Chemical structure of poly(p-phenylene viny-lene), PPV. Principal axes of proton hyperfine coupling of a π-electron are also shown for two inequivalent C–H bond orientations

understood as that of a π-electron on the polymer chain [133].

The samples used were prepared with a new precursor polymer containing cyclic sulphide [134] instead of the originally developed one [135]. The ESR spectra of the new samples completely lacked the unknown structure observed in films prepared by the original method [130]. This difference may be reasonably attributed to the improved quality of the films obtained by the new synthetic method, which almost completely eliminates the sp^3 defects that possibly give rise to unknown signals with different g values. The observed linewidth anisotropy suggests the dominance of the unresolved proton hyperfine structures of a π-electron, which can arise from the interactions of the distributed π-electron spin with the protons on the polymer chain. This situation has been shown to be exactly the case by direct measurement of the hyperfine coupling using ENDOR spectroscopy.

Figure 6.27 shows the anisotropy of the proton ENDOR spectra at 4 K in a 10-times stretched undoped PPV film. The external magnetic field is parallel to the stretch direction for the curves in (a) and perpendicular to the stretch direction for those in (b). In each figure the thick curve represents the spectrum, which was obtained by integrating the observed frequency-derivative spectrum shown by a dotted line. The broad distribution of the spectral frequency up to 19.5 MHz directly shows the distribution of the spin density on the polymer chain from equation (6.8). An important feature of the spectra in Figure 6.27 is that the spectrum taken with the field parallel to the stretch direction shows the larger hyperfine coupling. This provides direct evidence for the π-electron nature of the spin, similar to the case of polyacetylene. As discussed in section 3.1, the proton coupling of a π-electron shows the maximum value along the y-axis. Figure 6.26 shows that the y-axis is more inclined to the direction

Figure 6.27. Proton ENDOR spectra at 4 K in a 10 times stretched undoped PPV film [130]. The external magnetic field is parallel to the stretch direction for the curves in (a) and pe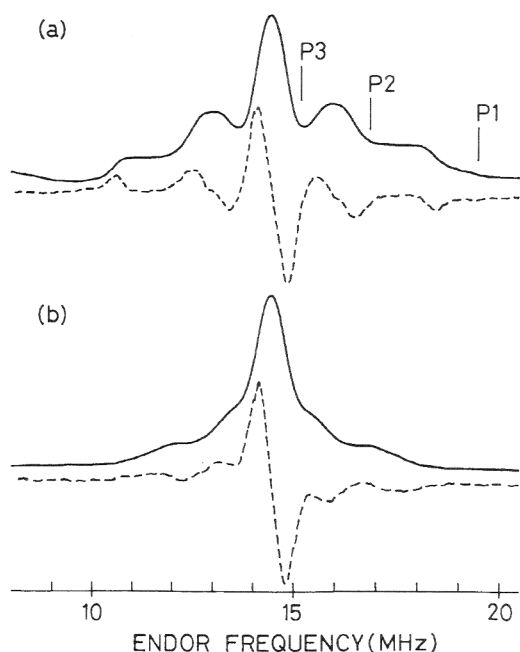rpendicular to that direction for those in (b). In each figure the solid curve represents the spectrum, which was obtained by integtating the observed frequency-derivative spectrum shown by a dotted line. Three distinct spectral turning points are marked as P1, P2 and P3 in the spectrum of the stretch direction (after [130])

of the polymer axis for the four protons (B′, C, E, F), while it points mid-way between the polymer axis and the direction perpendicular to it for the two protons (B, C′). Therefore, as a whole, larger proton coupling will be expected for the stretch direction, along which the polymer axis may be preferentially oriented.

Another important feature of Figure 6.27 is that the spectrum along the stretch direction has three distinct

spectral turning points, P1 to P3 as marked in the figure. These spectral turning points have been confirmed to be intrinsic structures associated with the single spin species observed by cw ESR, using the ENDOR-induced ESR technique [130,131]. The coupling constants corresponding to these turning points are summarized in Table 6.4 together with the values of the spin density deduced from them by assuming a McConnell's constant of 70 MHz (25 gauss). The largest spin density, determined from the largest coupling at P1, reaches 0.09. This quantity, defined as ρ_{max}, is nearly inversely proportional to the full width at the half maximum of the spin density distribution, defined as l_{hw}. In the case of the soliton in Shirakawa polyacetylene, ρ_{max} reaches 0.17 (with $A = 70$ MHz) corresponding to the l_{hw} of about 18 carbon sites (see Table 6.3). In polyacetylene the value of ρ_{max} is enhanced due to the electron correlation effect compared with the bare value of ρ_{max} in the limit of no electron correlation. Thus, if we assume that the electron correlation in PPV is of comparable strength to that in polyacetylene, l_{hw} of the present species comes close to 40 carbon sites, corresponding to several PPV monomer units.

The appearance of the structures at P2 and P3 shows that there are three distinct groups in the magnitude of spin density, the largest one with the peak value given by ρ_{max}, the intermediate one with the peak value (nearly half of ρ_{max}) obtained from P2, and the group with small spin densities with the peak density obtained from P3. In the case of the soliton in polyacetylene, the peak value of the second group of the spin density is associated with the negative spin density because of the non-bonding character of the soliton wavefunction as discussed in section 2.2. On the contrary, the peak value of the second group of the spin density would be positive for polaron excitation in conjugated polymers, as shown by the theory [132]. Experimentally this point would be confirmed by TRIPLE resonance in PPV, although it has not been observed in good S/N ratio so far because of the

Table 6.4. Hyperfine coupling and spin density associated with the three distinct spectral turning points resolved in the ENDOR spectra of PPV for the stretch direction shown in Figure 6.27 [130]

Spectral turning points in Figure 6.27	Hyperfine coupling (MHz)	Spin density[1]
P1	9.8	0.09
P2	5.1	0.05
P3	1.3	0.01

[1]Values calculated using the relation, $A_{obs} = \rho A_{yy}$, between the observed hyperfine coupling, A_{obs} and the spin density ρ. $A_{yy} = (1+\alpha)A$ shows the y-axis component of the hyperfine tensor of a π-electron radical. $\alpha = 0.5$ and $A = 70$ MHz (or 25 gauss in field units) are assumed.

sensitivity limitation due to the small concentration of the unpaired electrons.

3.3.2   Polaron spin distribution in PPV

These features of the ENDOR spectra of stretch-oriented undoped PPV have been successfully reproduced by the recent theoretical calcualtion of the polaron wavefunction, in the case of finite electron correlation, by Shimoi *et al.* Figure 6.28 shows the calculated spin density distribution of the polaron in a PPV chain based on the Pariser–Parr–Pople (PPP) model. The parameter values, such as electron–phonon and electron–electron interactions were adjusted so as to reproduce the observed ENDOR spectra well, by assuming $\lambda = 0.16$, an on-site Coulomb interaction of $U = 2.5t_0$ and near-neighbour interaction of $V = 1.3t_0$ and more long-range Coulomb interactions of Ohno-type potential. Further details are given in the paper. The centre of the spin density is located at the vinylene site. The spin density can be divided into three groups of relevant magnitudes. The largest spin density of 0.09, residing on the two vinylene bonds next to the central one. The second group is associated with the positive density and the third group with small densities including negative spin sites. The half-width of the spin distribution corresponds to about four PPV monomer units, as expected. Using this spin distribution, the observed anisotropic spectral lineshapes have been well reproduced with an ENDOR spectrum simulation method for a partially oriented system by taking the existence of the above two inequivalent sites of the C–H bond orientation into account. On the other hand, it was difficult to reproduce the observed spectra using spin

Figure 6.28. Spin density distribution of the polaron in PPV calculated by PPP model [132] Reprinted from Solid st. Commun. **95** (1995) 137–41.

densities calculated for no electron correlation. The agreement obtained, strongly supports the possibility that the observed dark spins in PPV are polarons trapped in the dark state of the polymer.

It is interesting to note that the above obtained extension of the spin density, i.e., the maximum value of the hyperfine coupling, is comparable to, but slightly smaller than, that observed for the radical anion (negative polaron) in solutions of oligomers of phenylene vinylene with the longest case of 7 monomer units, studied by ENDOR spectroscopies [136,137]. Although the detailed shape of the spin distribution in the reported oligomer naturally does not coincide with the present results obtained in the polymer, the approximate coincidence of the spatial extension further supports the possibility of the polaron.

3.3.3   Light-induced ESR

To invesitage the possibility of the trapped polarons as the origin of the dark spins, photo-induced ESR measurements at low temperatures would be useful, since it is highly possible that the light-induced ESR signal results from positive and negative polarons generated by photo-induced charge transfer between the polymer chains. Figure 6.29 shows an orientation dependence of the photo-induced ESR signal recorded at 4 K under the illumination of visible light (not monochromatic) in a stretched PPV sample. The external field is parallel to the stretch direction for the upper curve and perpendicular to it for the lower curve. As is clearly seen, the observed photo-induced signal shows a similar spectral span to the dark ESR signal. The light-induced signal shows clear anisotropy in linewidth and larger width for the stretch direction, which confirms that the light-induced species are π-electrons on the conjugated chain.

The anisotropic ESR spectra of the dark spins responsible for the ENDOR signals, detected by ENDOR-induced ESR, coincide well with that of light-induced ESR spectra, giving more detailed confirmation of the resemblance between the dark and light-induced species. [131]. It is also interesting to note that the spectral lineshape of these dark and light-induced ESR spectra are close to the reported $g = 2$ ODESR spectra [138], which have been assigned to recombination of the distant polaron pairs. More detailed discussion is given elsewhere [131].

Thus it would be highly possible that the presently observed dark species are trapped polarons, although the detailed generation mechanism of polarons in the
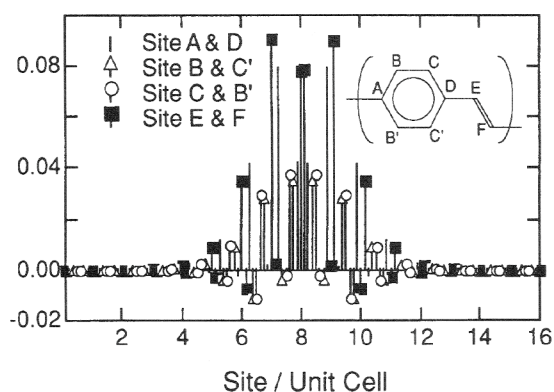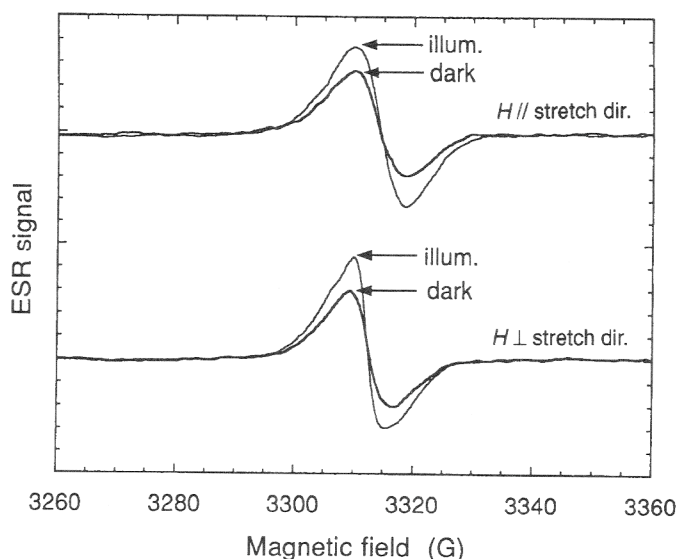
Figure 6.29. Orientation dependence of the ESR spectra at 4 K with and without illumination of visible light in a 10 times stretched undoped PPV film. The external field is parallel to the stretch direction for the upper curve and perpendicular to it for the lower curve [131] (after ref. [105])

dark state, such as accidental doping by oxygen, thermal generation etc., is not yet clear at present. The trapped sites of the polaron would be the defects such as chain-ends or remaining sp^3 defects in the polymer [128]. Further studies of photo-induced signals, such as the signal dependence on the excitation wavelength might provide more detailed information concerning the discrimination of the positive and negative polaron signals and their relation to the dark signal.

3.4 Pernigraniline

Pernigraniline base is the highest oxidized state of the three isomers of polyaniline. It has a degenerate ground-state structure that possibly generates neutral solitons, as in the case of *trans*-polyacetylene [139–141]. The degenerate ground state results from the alternation of benzenoid (B) and quinoid (Q) rings connected with conjugated nitrogen atoms (N), accompanied by bond-length and ring-torsion dimerization. The theoretically expected structure of the soliton is the neutral soliton of benzenoid-nitrogen-benzenoid (BNB) structure [140]. The wavefunction is centred on a nitrogen site and localized to two adjacent rings.

Although no ENDOR studies were made on this system, a solution EPR technique has been employed as

an alternative to observe the spin density distribution of the neutral soliton [142]. The reported ESR spectra of this polymer dissolved in dioxane is dominated by a triplet structure, each of the triples being associated with resolved peaks of smaller splittings. The dominance of the triplet shows that the largest spin density resides on the nitrogen site giving rise to a triplet hyperfine splitting due to the ^{14}N nucleus, as predicted. This is also consistent with the obsevation of the similar triplet feature in the powder of the polymer. The advantage of the solution spectra compared with the powder spectra is the much higher spectral resolution due to motional averaging of the g and hyperfine anisotropies. The structures of each triplet of the solution spectrum result from the hyperfine splittings of the proton of adjacent rings, the analysis of which yields the spin densities on the carbon bonded to the hydrogens, as discussed in section 3.1.

The observed ESR spectrum has been well reproduced by simulation using hyperfine splitting due to a single ^{14}N and four equivalent ^{1}H. The spin densities determined for respective sites are $\rho_N \approx 0.36$ and $\rho_C \approx 0.125$, that is, most of the spin densities reside on these sites and the densities on other sites are much smaller. The observed proton splittings should be ascribed to the spin densities on the four carbons meta to the central nitrogen (the second nearest carbon to nitrogen), bonded to protons. On-site Coulomb energy

U of about 2.5 eV was proposed to account for the observed spin-density distribution. The existence of the resolved hyperfine structures of the ESR spectra shows that the motion of the spin is much slower than the timescale of hyperfine coupling, which was attributed to the role of ring motion.

4 DYNAMICS OF NEUTRAL SOLITON IN PRISTINE TRANS-POLYACETYLENE

One of the controversial topics in conjugated polymers is the existence of a paramagnetic conjugational defect (neutral soliton is the common name) in trans-PA and its dynamics, if it diffuses with the veolcity as rapid as phonons in trans-PA at room temperature [61,62,77–82,143–165]. Goldberg and co-workers have proposed the presence of a neutral kink-soliton with spin 1/2 but no charge as a zone-boundary of the bond alternation from the observations; the ESR g-shift suggesting π-electron character, and lineshape and temperature dependence that indicates typical motional narrowing behaviour [166]. Subsequently, Weinberger and co-workers suggested the existence of charged solitons carrying charge but not spin, especially in a lightly doped regime of polyacetylene less than 2–5% in which the measured susceptibility was remarkably small in comparison with that expected from the number of injected charges by doping [167,168], implying the storage of charges as the charged solitons. Such solitons [100,169], polarons and bipolarons [170] have unique characters as summarized in Table 6.5.

On the dynamics of the neutral soliton, in 1980 Nechtschein and co-workers have demonstrated the evidence for the rapid diffusion of the neutral soliton along a one-dimensional chain from the observation of the pure Overhauser effect (OE) in trans-PA using a dynamic nuclear polarization (DNP) experiment and from the $1/\sqrt{\omega}$ frequency dependence of the ^{1}H NMR spin-lattice relaxation rate T_{1H}^{-1} [143]. These observations give quantitative estimations that the pure OE implies the condition $\tau_c^{-1} \gg \omega_e \approx 10^{11}$ rad/s for the

correlation time of motion τ_c, where ω_e is the Larmor frequency of the electron spin, and that the diffusion rate along the chain is $D_\parallel \approx 10^{13}$ rad/s [171] from a slope of proportionality between T_{1H}^{-1} and $f^{-1/2}$. These two estimations are consistent with each other. On the other hand, Weinberger and co-workers obtained a value of $\tau_c^{-1} \approx 10^{11}$ rad/s for the correlation time [53] somewhat smaller than 10^{13} rad/s obtained by ^{1}H NMR [143], analyzing the ESR linewidth at 300 K with the formulation by Hennessy et al. [172]. This is the first disagreement about the correlation time between NMR and ESR. In this chapter an evolution of interpretations on the neutral soliton will be followed.

4.1 DNP in undoped polyacetylene

Good evidence for the rapid motion and trapping of the soliton is demonstrated by a DNP experiment as shown in Figure 6.30 [146,173]. The dynamic nuclear polarization (DNP) experiments are carried out at ≈ 9 GHz between 1.5 and 300 K in cis [143,174] and trans PA [143,145,146,173,174]. At room temperature the pure Overhauser effect (OE) was observed in all-trans-PA without air or oxygen but a mixed solid state effect (SSE) together with OE was found in cis-rich PA without air [143,174] and all-trans-PA with air [146]. In particular, below 150 K, the mixed effect was observed, even in all-trans-PA without air [145,173]. The OE is characteristic of dynamic interaction between nuclear spins and electron spins, with rapid motion. On the other hand, the SSE is of the static interaction between them. In other words, observation of the pure OE is clear evidence for the electron spin for motion with an inverse of the correlation time τ_c^{-1} comparable with or larger than ω_e. At 300 K, the pure OE observed in all-trans-PA, is consistent with the conclusions for the neutral soliton to diffuse rapidly compared with $1/\omega_e$ as concluded from the ESR linewidth narrowed by motion [53] and the proton NMR T_{1H}^{-1} [143] as a function of frequency over a broad range.

Table 6.5. The elementary excitations in the polymers with degenerate and non-degenerate ground states

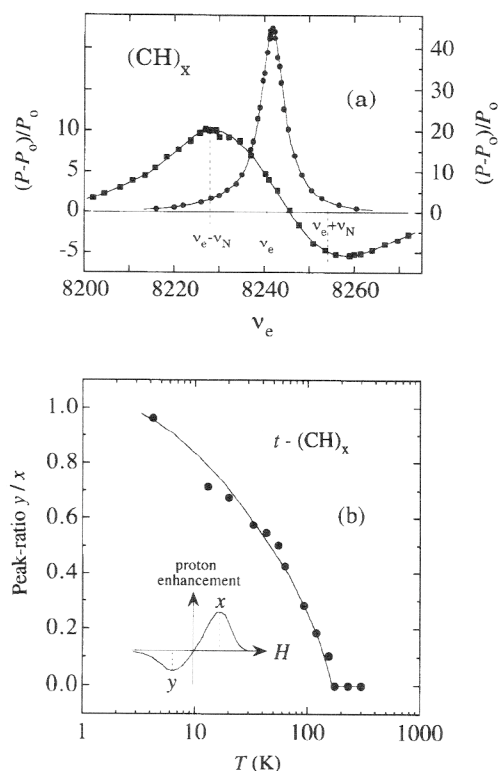|	Degenerate ground state		Non-degenerate ground state	
	Neutral soliton	Charged soliton	Polaron	Bipolaron
Spin	1/2	0	1/2	0
Charge	0	$\pm e$	$\pm e$	$\pm 2e$

Figure 6.30. Enhancement of the proton NMR signal amplitude (P/P_o-1) is shown as a function of microwave frequency ν_e as taken by the dynamic nuclear polarization experiments, where P and P_o are the signal amplitude with and without microwave pumping, respectively [143,146,173,174]. The Overhauser effect (OE) typical to the mobile spins makes a sharp peak at the Larmor frequency ω_e of the electron spin but the Solid State Effect (SSE) shows two extrema separated by $\pm\omega_n$ from ω_e characterictic with the fixed paramagnetic spins [8]. The solid curves are a guide for the eye. (a) , trans-(CH)$_x$ ($\Delta H_{pp} \approx 0.8$ G) and ■, cis-rich (CH)$_x$ ($\Delta H_{pp} \approx 7.8$ G) [174]. (b) The temperature dependence of the peak-ratio in trans-(CH)$_x$ [173]. $y/x = 0$ means pure Overhauser enhancement and $y/x = 1$, the solid state effect [173]. Note the change from the mobile above 150 K to the trapped below 150 K. Most of the solitons are trapped below 10 K. (after (a) [174] and (b) [173])

Clark and co-workers measured the temperature dependence of a DNP experiment and succeeded in obtaining OE and SSE independently as shown in Figure 6.30 [173], indicating a characteristic crossover from pure OE above 150 K to the mixed effect below 150 K. The OE and the SSE can be distinguished by the ESR frequency at which the maximum enhancement would be obtained (and equivalently by the peak-ratio y/x as shown in Figure 6.30); the same frequency as the usual ESR peak for the OE, but at $\omega_e \pm \omega_n$ for the SSE. Namely, in the SSE a required energy $\hbar(\omega_e \pm \omega_n)$ for

simultaneous spin flip in both nuclear and electron spins could be supplied by the rf irradiation instead of the spectral density of spin motion in OE. Then, when τ_c^{-1} of the electron spin motion becomes smaller than ω_e, the OE starts to disappear due to diminution of the spectral density at $\omega_e \pm \omega_n$ and, at the same time, the SSE starts to increase. Similarly, the SSE will disappear because of decoupling caused by spin motion and the OE starts to increase when τ_c^{-1} increases more than $\gamma_c\Delta H_e \approx 10^8$ rad/s. Therefore, the appearance of the SSE below 150 K corresponds to τ_c^{-1} decreasing from ω_e to less that $\gamma_c\Delta H_e$, that is, slowing down of soliton diffusion, perhaps trapping by the oxygen potential [147,175], residual catalyst [77,158], disorder [72], interchain coupling [176–178] and the remnant cis-linkages [71,179] proposed experimentally and theoretically. With the trapping effect and theoretical consideration on OE and SSE they obtained a temperature dependence of the number of diffusing solitons and the diffusion rate that is proportional to $T^{1/2}$ [173]. Recently, however, it has been suggested that such a conclusion has to be corrected [82], nevertheless the above consideration remains valid.

4.2 ^{1}H and ^{13}C NMR T_{1H}^{-1} in undoped polyacetylene

Many investigations on NMR T_{1H}^{-1} have been reported at various frequencies ranging from less than 20 kHz to 200 MHz and temperatures from 0.3 K to 295 K, [143,144,146–154,180,181], as summarized in Figure 6.31. Not all the authors, however, came to the same conclusions. An entirely different mechanism from rapid spin motion for T_{1H}^{-1} was proposed to be the modulation of the nuclear dipolar coupling due to thermal libration of the chain, based on the very small value of $T_{1H}^{-1} \approx 5$ s^{-1} [150]. Such a possibility for the mechanism is ruled out as a predominant one in most of the other data, since their data on T_{1H}^{-1} are as small as one-tenth of others.

The basic idea of deriving the diffusion rate from T_{1H}^{-1} came from the frequency dependence of T_{1H}^{-1} proportional to $1/\sqrt{\omega}$ in the wide frequency range from 0.1 to 100 MHz [143,144,146–149], as predicted by a 1-D spin diffusion model,

$$T_1^{-1} = k_B T\chi[\tfrac{3}{5}\,d^2\phi(\omega_n) + (a^2 + \tfrac{7}{5}d^2)\phi(\omega_e)], \quad (6.14)$$

where $\phi(\omega) = 1/\sqrt{2D_\parallel\omega}$ is the spectral density [182,183] induced by modulation of hyperfine coupling due to the diffusion of the electron spins. Here, χ is the normalized spin susceptibility, a and d are the
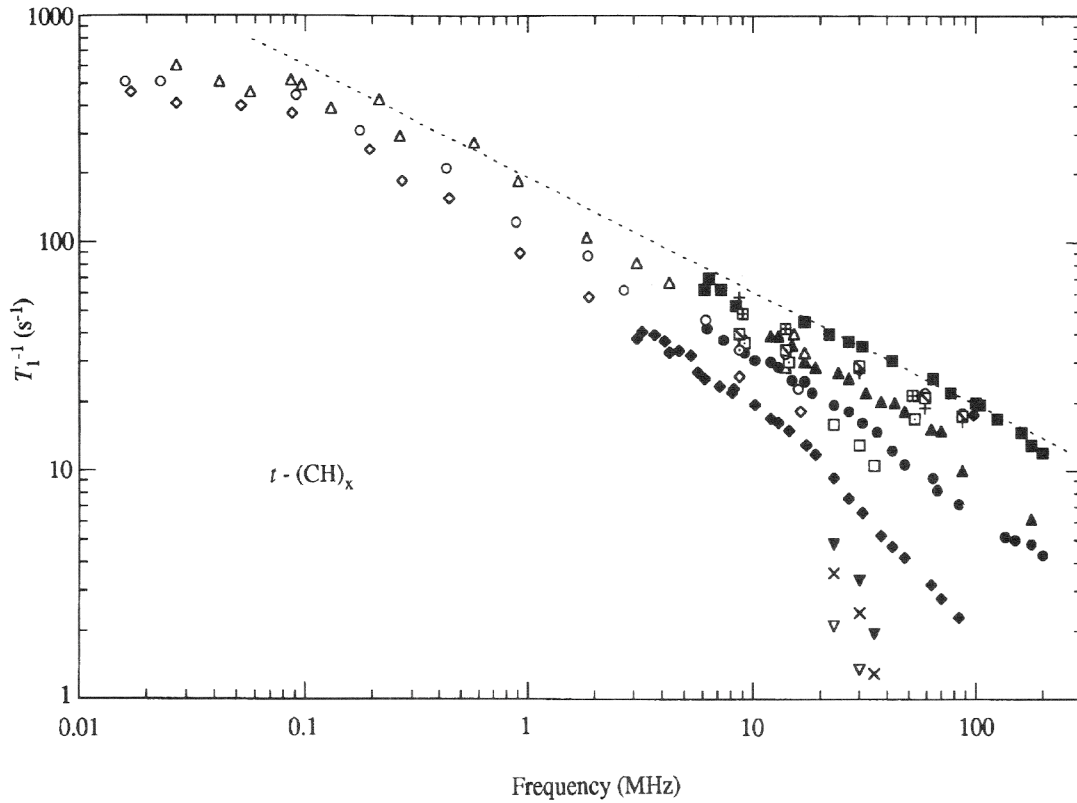
Figure 6.31. The proton spin-lattice relaxation rate T_{1H}^{-1} as a function of proton frequency: at 295 K (■); at 77 K (▲); at 30 K (●); at 4.2 K (◆) [147]; at 150 K (△); at 35 K (○); at 7 K (◇) [151]; at 295 K (⊞); at 77 K (□)[187]; at 300 K (+); at 260 K (⊠); at 140 K (⊙) [149]; at 4.5 K (□); 1.0 K (▼); 0.85 K (×); 0.6 K (▽) [153]. The dotted line shows $1/\sqrt{\omega}$ dependence. Reproduced from 'Magnetic Properties of Conjugated Polymer in Conjugated Conducting Polymers', *Springer Series in Solid State Sciences* **102**, 256, P. K. Kahol, W. G. Clark and M. Mehring. Copyright 1992 Springer-Verlag, Heidelberg.

isotropic and dipolar electron–proton hyperfine couplings in units of s^{-1}, respectively. It is seen in Figure 6.31 that the formula (6.14) fails to reproduce the data at $T < 295$ K and $f > 10$ MHz, where T_{1H}^{-1} does not follow $f^{-1/2}$ but a negative constant in addition to $f^{-1/2}$, that is, $f^{-1/2}$-const [147,153,184]. Such a discrepancy with the simple 1-D diffusion model was wiped out by taking account of extension of the soliton wavefunction instead of a point picture at a single carbon atom, assumed in (14) [147,185]. In the case of the extended soliton the spectral density is modified to [6,185]

$$\phi(\omega) = (1/\sqrt{2D_\parallel \omega}) - (L_{\text{eff}}/D_\parallel), \qquad (6.15)$$

where L_{eff} is the effective full length in units of the carbon–carbon distance and equal to γL in [147,185] valid for $L > 5$. Here, L is the soliton length, $\gamma = 0.33$ for a box-shaped soliton, $\gamma = 0.36$ for an alternated

soliton [147,185] and $\gamma = 0.5$ for the SSH soliton [6]. Using the intercept $-L_{\text{eff}}/D_\parallel$ and $D_\parallel = 5.7 \times 10^{10}$ rad/s estimated at 4.2 K, the soliton length was estimated as $L/2 = 8.5$ [147] which is compared with $l_{\text{hw}} = 18$ in Table 6.3.

Other problems to be resolved, revealed by further experimental studies, are: (1) that the temperature dependence of ^{1}H NMR; T_{1H}^{-1} yields a temperature variation of the diffusion rate that is inconsistent with the motional narrowing of the ESR linewidth and the DNP results; (2) that ^{13}C NMR T_{1C}^{-1} does not follow (14) [148,150,152,181]; and (3) that a variety of ESR measurements gave conclusions inconsistent with each other both qualitatively and quantitatively [160, 161,164,165,186].

Problem (1) is as follows. If one applies (6.14) to T_{1H}^{-1}, the temperature dependence of the diffusion rate can be obtained as $D_\parallel \propto T^{-1/2}$ as demonstrated in

[148], which agrees with a theoretically predicted variation caused by 3-D acoustic phonons. [176] but the ESR motional narrowing suggests $D_\parallel$ goes to zero at $T = 0$. To settle this problem a two-spin species model was proposed by analyzing the ESR lineshapes in different samples, including treatment by air, with memory function formalism [146]. The model assumes a coexistence of mobile and trapped spins specified by the presence of an effect of the oxygen potential; the mobile spin is responsible for the relaxation mechanism of (6.14) but the trapped spin makes a negligible contribution to T_{1H}^{-1}. These spins must couple each other by an exchange interaction to keep consistency with the observation of only a single ESR line. If the mobile spins decrease with decreasing temperature, the above inconsistency between T_{1H}^{-1} and the ESR linewidth can be accounted for. This model was further refined [147] to reproduce both the temperature dependence of T_{1H}^{-1} and the ESR linewidth for both the samples in vacuum and air as a diffuse/trap model that takes account of the kinetics of oxygen with polyacetylene [175], in which single spin is assumed both to diffuse and to be trapped in time-sharing instead of a two-spin species assumed in the former model [146]. The ESR linewidth is described by

$$\Delta H = C\Delta H_L + (1 - C)\Delta H_D, \qquad (6.16)$$

where ΔH_L and ΔH_D are the linewidths for trapped and diffusive spins, respectively, and C is the relative trapped spin concentration represented by

$$C = \frac{p}{p + (1 - p)\exp(-E/kT)}, \qquad (6.17)$$

where p is the concentration of the trap and E is the trapping energy that was assumed to be distributed from 0 to 650 K to account for the observed ESR linewidth [147]. It is noteworthy that this model is consistent with the observations in T_{1H}^{-1} [147], the DNP results [173] and the ESR T_{1e}^{-1} [78,187] and also the linewidth as a function of frequency over broad range [6,61,62,79–82,156] (see section 4.2).

Problem (2) is that the spin-lattice relaxation rate of ^{13}C NMR, T_{1C}^{-1}, should obey (6.14) as ^{1}H NMR T_{1H}^{-1} does, if the neutral soliton diffuses whole the sample. To investigate a role of spin flip/flop diffusion through ^{1}H and ^{13}C Scott and Clarke have measured T_{1H}^{-1} and T_{1C}^{-1} in the samples enriched by various ratios of ^{13}C to ^{2}D: (1) 98:0; (2) 90:98; and (3) 20:98 [152]. They observed:

(a) the frequency dependence of ^{1}H NMR T_{1H}^{-1} was 45, 37 and 18 s^{-1} at 11.5, 23 and 90 MHz, respectively,

for the sample (1) consistent with the reported results [147].

(b) the frequency independence $T_{1C}^{-1} \approx 1.9$ s^{-1} for (1) and 0.9 s^{-1} for sample (3) at both ~ 12 and 23 MHz, and

(c) a sizeable frequency dependence with the shortest values 2.6 and 2.3 s^{-1} at 12 and 23 MHz, respectively, for sample (2), as shown in Figure 6.32 together with data from [148,150,181].

From the above observations the other relaxation process—to a fixed paramagnetic spin via the spin flip/
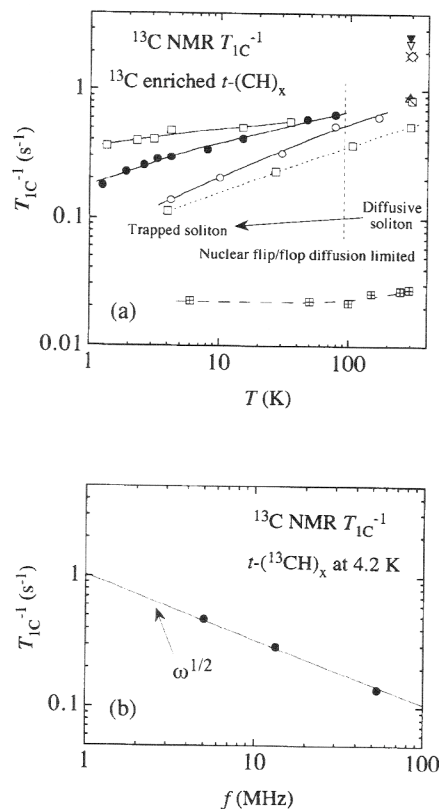
Figure 6.32. The spin-lattice relaxation rate of ^{13}C NMR in plyacetylenes with a variety of (^{13}C/^{2}D) isotope enrichment as functions of (a) temperature and (b) frequency. The degree of enrichment is represented by (% of ^{13}C / % of ^{2}D). □, (90/0)/5 MHz; ●, (90/0)/13.3 MHz; ○, (90/0)/53 MHz with solid curves [148]; ▼, (90/98)/12 MHz; ▽,(90/98)/23 MHz; ◇, (98/0)11.5 MHz; ×, (98/0)/23 MHz; △, (20/98)/12 MHz; ×, (20/98)/23 MHz [152]; ⊞, (50/0)/42 MHz with the dashed curve [150]; ☐, (45/0)/42 MHz with the dotted curve [181]; ◨, (45/0)/50.3 MHz [154]. The curves are guides for the eye.

flop diffusion due to the nuclear dipolar interaction—was considered, which is given by [8,83]:

$$T_{1H}^{-1} = 4\pi N_e C^{1/4} D_n^{3/4} \propto N_e N_n^{1/4} \gamma_n^2 \omega_n^{-1/2} T_{2e}^{-1/4} \quad (6.18)$$

valid in the diffusion-limited situation, where $C = (3/10)g^2\mu_B^2\gamma_n^2/\omega_n^2\tau$, D_n is the nuclear spin flip/flop diffusion constant that is independent of the Larmor frequency, N_e and N_n are the concentrations of the electron spins and the nuclear spins, respectively, and T_{2e} is the electron transverse relaxation time [152]. It should be noted that (6.18) has the same frequency dependence as the 1-D spin diffusion case (6.14).

Finally, they proposed a model to account for T_{1C}^{-1} together with T_{1H}^{-1} that only 1/30 of the chains carry one neutral soliton and that the nuclear magnetization flows to a cylindrical relaxation core due to a soliton diffusion, through the nuclear flip/flop diffusion. An interpretation of the above observations with this model is as follows. On ^{1}H NMR T_{1H}^{-1} it is reasonable that the non-deuterated sample (1)(98/0) shows $1/\sqrt{\omega}$ dependence due to the soliton diffusion, but not for the fully deuterated samples (2)(90/98) and (3)(20/98) in which the flip/flop diffusion rate of ^{1}H is slower than a sink rate of the relaxation cores. On ^{13}C NMR T_{1C}^{-1} a situation is more complicated. In the samples (1)(98/0) and (3)(20/98), the observed frequency independency of T_{1C}^{-1} can be reasonable understood by a diffusion limited situation where T_{1C}^{-1} is dominated only by the ^{13}C flip/flop diffusion rate D_n smaller than the sink rate of relaxation cores because of detuning due to large and random local field by protons for (98/0) and because of increased nuclear distance between ^{13}C nuclei for (20/98). On the other hand, in the sample (2)(90/98), since the absence of detuning due to proton local fields, ^{13}C NMR T_{1C}^{-1} shows a weak but similar frequency dependence to that of T_{1H}^{-1}. Contrary to such a successful interpretation, the magnitude of the relaxation rates T_{1C}^{-1} are an order of magnitude smaller than that of T_{1H}^{-1}, although T_{1C}^{-1} and T_{1H}^{-1} are expected to have a similar magnitude provided that the hyperfine coupling constants are the same order, as suggested by the ENDOR experiment [188]. This suggests that T_{1C}^{-1} is still under the control of the nuclear flip/flop diffusion process.

Kume and co-workers reported the temperature dependence of T_{1C}^{-1} for the sample (90/0) at 5, 13.3 and 53 MHz as shown in Figure 6.32 [148]. Above 100 K, T_{1C}^{-1} can be classified to the diffusion limited criteria where T_{1C}^{-1} is independent of the frequency, as observed in sample (1), (98/0) in [152]. Below 100K, the frequency dependence turns upwards and gradually

approaches $1/\sqrt{\omega}$ behaviour below 10 K as indicated in Figure 6.32(b). This is, however, not an indication of the 1-D diffusion represented by (6.14) but the fixed paramagnetic spins by (6.18), i.e. a conventional mechanism of the nuclear spin flip/flop diffusion to the fixed paramagnetic spins (fixed solitons) dominates T_{1H}^{-1}, since most of the solitons would be fixed to the trapping centres below 10 K, according to the conclusion of DNP experiments [173,174] and T_{1H}^{-1} [147]. Another implicating point of Figure 6.32 is the focussing behaviour from a small as $T_{1C}^{-1} \approx 0.1$ s^{-1} at low temperatures to $T_{1C}^{-1} \approx 1$ s^{-1} at increasing temperature at all the frequencies, 5, 13.3 and 53 MHz, which implies that the limited nuclear flip/flop diffusion rate is around 1 s^{-1} in these samples, as estimated by Scott and Clarke [152]. Masin and Gusman also studied T_{1C}^{-1} versus temperature for the sample (45/0) at 42 MHz, [181] and obtained a result consistent with the above consideration.

Masin and co-workers reported an extremely small $T_{1C}^{-1} \approx 0.025$ s^{-1} as shown in Figure 6.32, together with very small $T_{1H}^{-1} \approx 5$ s^{-1} [150]. From these observations it is implicative that the mobile spins are lacking in their sample as discussed by Ziliox et al. [154].

Kahol and co-workers have formulated the idea by Scott and Clarke successfully to reproduce T_{1H}^{-1} and T_{1C}^{-1} in the whole frequency range from 0.02 to 200 MHz, yielding a value of $\tau_\parallel^{-1} \approx 5 \times 10^{12}$ rad/s and 170 c$_\parallel$ as the length of the cylindrical confinement area [2,189,190].

4.3   ESR in undoped polyacetylene

A variety of ESR experiments: ESR linewidth; free-induction decay; spin-lattice relaxation rate T_{1e}^{-1}; phase memory time T_{2M} and multiple quantum coherence (MQNMR) have been measured in *trans*-PA to study the dynamics of the paramagnetic spin [61,62,78,79,82,155,156,159–165,186,191] and a variety of conclusions have been reached:

(1) From the experiments on the ESR T_{2M}, the linewidth and the electron free-induction decay (FID), equivalent to the linewidth, it is concluded that the paramagentic spins are diffusive but its rate might be three orders of magnitude smaller than that from ^{1}H NMR T_{1H}^{-1}, (159–161,163].

(2) From the experiments on the ESR T_{1e}^{-1} and the linewidth as a function of frequency in a broad range, the diffusion rate is concluded to be very similar to that obtained by ^{1}H NMR T_{1H}^{-1} both

qualitatively and quantitatively, [61,62,78,79,82, 155,156].

(3) From the experiments on the ESR T_{1e}^{-1} at X-band, a rapid diffusion of spins is found but the temperature dependence is contrary to that of ^{1}H NMR T_{1H}^{-1}, that is, $D_\parallel$ decreases with increasing temperature, [164,191].

(4) From the experiment on the multiple quantum NMR technqiue, a distinguishable conclusion is that all the paramagnetic spins and the neutral solitons are fixed in the sample even at room temperature [165,186].

The origin of these discrepencies is a lack of basic knowledge of dynamics of spins; diffusion and trapping. Different underlying assumptions has been used to reach the above conclusions. Here, we try to follow one possible route to interpret the above experimental data in the following chapters [6,82].

4.3.1   ESR linewidth versus frequency

One of the basic parameter of magnetic resonance is the linewidth. Information obtained from the linewidth is limited when the linewidth is measured at a fixed frequency. If one has a frequency axis in addition to the temperature, one can get more information for analyzing the origin of the linewidth. In Figure 6.33 the frequency dependence of the ESR linewidth is demonstrated at a variety of temperatures, [6,79–82] which shows characteristic behaviour in two respects; the peak-to-peak ESR linewidth is proportional to the $1/\sqrt{f}$ and saturates around at $1/\sqrt{f} \sim 0.2$, typical of the quasi-1-D (Q-1-D) diffusive motion of the neutral soliton described by [6,81,82]:

$$\Delta H(T, \omega) = \Delta H_{\text{trap}}(T) + \Delta H_{\text{diff}}(T, \omega), \qquad (6.19)$$

$$\frac{\sqrt{3}}{2}\gamma_e \Delta H_{\text{diff}} = T_{2e}^{-1} = \gamma_e^4 \hbar^2 S(S+1) c \Sigma_I [0.3\phi(0) + 0.5\phi(\omega_0) + 0.2\phi(2\omega_0)] \qquad (6.20)$$

for the electron–electron dipolar interaction and;

$$\phi_{\text{Q1D}}(\omega) \approx \frac{1}{\sqrt{4D_\parallel/\tau_\perp}} \sqrt{\frac{1 + \sqrt{1 + (\omega\tau_\perp/2)^2}}{1 + (\omega\tau_\perp/2)^2}} \qquad (6.21)$$

for the Q-1-D diffusion, which can be simplified by $1/\sqrt{2D_\parallel\omega}$ at $\omega\tau_\perp \gg 1$ and $1/\sqrt{2D_\parallel/\tau_\perp}$ at $\omega\tau_\perp \ll 1$. Here, ΔH_{trap} is the frequency independent part, which is interpreted as the linewidth due to trapping of the
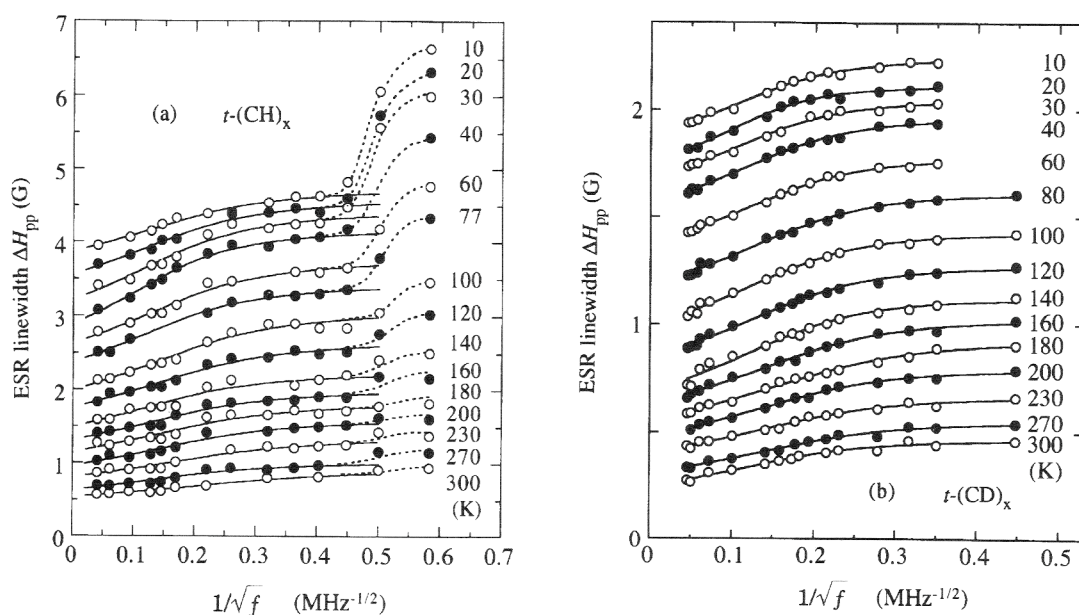
Figure 6.33. The frequency dependence of the ESR linewidth for: (a) *trans*-(CH)$_x$ and (b) *trans*-(CD)$_x$ as a function of $f^{-1/2}$ with the implicit parameter of the temperature [6,79–82]. The solid curves indicate a fitting to (6.19). Note that the anomalous line broadening is found at lower frequency than 5–6 MHz ($1/\sqrt{f} \approx 0.4$) only in *trans*-(CH)$_x$. The dotted curves are a guide for the eye. Reproduced from (a) Synth. Met. **28** (1989) D393-8 and (b) Synth. Met. **17** (1987) 439–45.

neutral soliton, ΔH_{diff} the linewidth due to a diffusive motion of the neutral soliton, which is composed of the lifetime broadening $T'^{-1}_{1e} \propto 0.5\phi(\omega_0) + 0.2\omega(2\omega_0)$, and the motional narrowed width $T'^{-1}_{1e} \propto 0.3\omega(0)$ independent of frequency [8], Σ_l is the lattice sum, c the electron spin concentration, $D_\parallel$ the diffusion rate along the chain and $\tau_\perp^{-1}$ the cut-off frequency of the 1-D diffusive motion. ΔH_{diff} is the homogeneous broadening, but whether ΔH_{trap} is homogeneous or inhomogeneous depends on the nature of 'trapping' as will be mentioned in section 4.3.4. For the *trans*-$(CH)_x$ ΔH_{diff} is largely contributed by the hyperfine interaction [6,78,82]. The solid curves in Figure 6.33 indicate the model fitting by (6.19) that well reproduces most of the data, excluding the frequencies lower than 5–6 MHz ($1/\sqrt{f} \sim 0.4$) uniquely for *trans*-$(CH)_x$.

There is an arguement that, with the temperature and frequency dependence of T^{-1}_{1e} estimated at 9 and 16 GHz, assuming a validity down to the very lowest frequencies, ^1H NMR T^{-1}_{1H} could be accounted for by the fixed paramagnetic spins and the nuclear flip/flop diffusion as represented in (6.18) [161]. However, the linewidth in Figure 6.33 is difficult to explain only by the fixed spins, and a similar mechanism to T^{-1}_{1H} through the flip/flop diffusion, which does not hold for the ESR case here no relaxation centre as the fixed electron spin in the NMR case exists.

4.3.2 Assignment of ESR relaxation mechanism

Assignment of the relaxation mechanism described by (6.20) is carried out using T^{-1}_{1e} as a function of the electron spin concentration and frequency as shown in Figure 6.34 and its inset [6,78,82,164]. T^{-1}_{1e} varies linearly with the spin concentration c, which indicates that the relaxation mechanism is due to the diffusive motion of the neutral soliton, that is, the probability c of finding a spin at any lattice site is definitive in this mechanism, as contrasted with the fixed spin mechanism being proportional to $r^{-6} \propto c^2$. The intercept of the inset also demonstrates the existence of the hyperfine interaction that is proportional to $\gamma_n^2 I(I+1)$ which gives a ratio of ≈ 16 for ^1H to ^2D in agreement with the inset. Such a large relaxation rate $\approx 10^6$ s^{-1}, due to the hyperfine coupling with the proton, could not be accounted for by the static coupling between the fixed spins and protons, but by the dynamic diffusive motion of the neutral solitons which have a chance to interact with a lot of protons. Although such a hyperfine contribution is an orgin of the difference in T^{-1}_{1e} for *trans*-$(CH)_x$ and *trans*-$(CD)_x$, Robinson and co-workers reported no difference in T^{-1}_{1e}s between *trans*-$(CH)_x$ and *trans*-$(CD)_x$ at the X-band [164]. Denis and co-workers, however, suggested more complicated behaviour for isotope enriched polyacetylenes at the X-band [191].
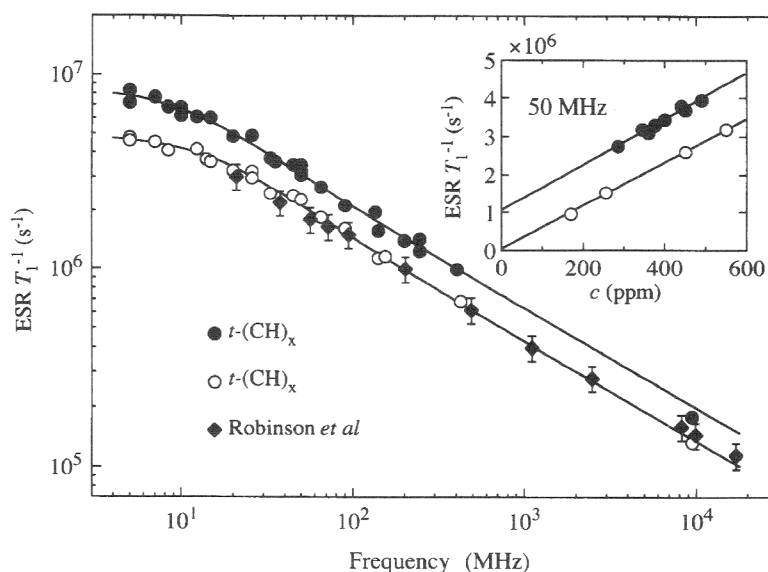
Figure 6.34. The frequency dependence of the spin-lattice relaxation rates at room temperature in *trans*-$(CH)_x$ (●) and *trans*-$(CD)_x$ (○) measured by the saturation technique [78]. ◆, from Robinson *et al* [164]. Inset: T^{-1} as a function of spin concentration c (ppm) for both *trans*-$(CH)_x$ and *trans*-$(CD)_x$. Note the well-defined difference at $c = 0$ between *trans*-$(CH)_x$ and *trans*-$(CD)_x$, which comes from the hyperfine interaction with the proton or deuteron [78].

T_{1e}^{-1} shows consistent behaviour with the linewidth, T_{2e}^{-1}, as a function of frequency described by [6,8,80,82]:

$$T_{1e}^{-1} = \gamma_e^4 \hbar^2 S(S+1) c \Sigma_l [0.2\phi(\omega_0) + 0.8\phi(2\omega_0)].$$

(6.22)

The calculated diffusion rates $\approx 10^{13}$ rad/s from all of the T_{1e}^{-1}'s independently for both the electron–electron dipolar and the hyperfine interactions, and from T_{2e}^{-1}, are consistent with ^{1}H NMR T_{1H}^{-1} as shown later [6,61,78, 81,82,164].

The ESR linewidth as a function of frequency is summarized schematically in Figure 6.35 based on the diffuse/trap model. The upper two areas indicate ΔH_{diff} and the lower one ΔH_{trap}. It can be assumed that the first term in (6.19) is caused by a static hyperfine interaction from the consideration of the phase of anisotropy pattern in both trans-(CH)$_x$ and trans-(CD)$_x$ [61]. According to the diffuse/trap model (see section 4.2) the neutral soliton experiences two different states, diffusing and trapped, as a time sharing. A ratio of trapping time to the unit period, c_{tr} is defined by $c_{tr} = \tau_{trap}/(\tau_{trap} + \tau_{diff})$ and $c_{diff} = 1 - c_{tr}$, which determines the average behaviour of the soliton. Here, τ_{trap} is the average time at the single trapping site and τ_{diff} is the time diffusing among the normal sites between succeeding trappings. The width due to trapping, ΔH_{trap} can be written by $c_{tr}\Delta H_{hyp} + c_{tr}^2 \Delta H_{dip}$, where $\Delta H_{hyp} = 0.87$ G for trans-(CD)$_x$ and 3.16 G for trans-(CH)$_x$ and $\Delta H_{dip} = 0.54$ G are the hyperfine and electron–electron dipolar broadenings in the trapped state, respectively [6,82]. Here, the coefficient of the second term c_{tr}^2 is due to a
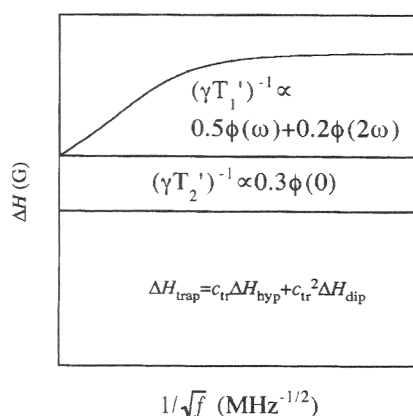

Figure 6.35. A schematic figure for the ESR linewidth with the diffuse/trap model.

requirement of at least two solitons in the trapped state. By analyzing the data in Figure 6.33 one obtains several parameters: the effective number of the solitons c_{tr} in the trapped state, the on-chain diffusion rate $D_\parallel$, the cut-off frequency $\tau_\perp^{-1}$, the motional narrowed width $(\gamma_e T_{2e}'^{-1})$ and the maximum spin density of the neutral soliton ρ_{max}.

4.3.3 Anomalous broadening in trans-(CH)$_x$

The diffuse/trap model can explain the anmalous extra broadening below 5–6 MHz in particular in trans-(CH)$_x$ as shown in Figure 6.33. At first, a conclusion is given; the anomalous broadening comes from a cross-over from unlike spins under $f \gg |A\rho m_H| = |A\rho|/2$ to like spins under $f \ll |A\rho|/2$, where $A\rho$ is the effective hyperfine coupling constant described by the spin density ρ and the average hyperfine constant A in units of frequency, and $m_H = \pm 1/2$ is the directional quantum number for the proton nucleus. The solitons in the trapped state couple with the protons statically via only an $aS_z I_z$ term conserving Zeeman energy under high-field conditions $f \gg |A\rho|/2$ which defines 'unlike spins'. Under the low-field $f \ll |A\rho|/2$ the spin flip/flop term $bS_\pm I_\mp$ becomes effective in addition to $aS_z I_z$ because of overlapping of both the spectra, which means that both the electrons and protons are of 'like spins'. In this limit the ESR spectrum is homogeneous. To render this mechanism effective, the condition between the duration at the trapping site and the effective hyperfine constant $\tau_{trap} \gtrsim 2/|A\rho| (\sim 10^{-7}$ s) should be satisfied.

Such a conclusion predicts the same phase of anisotropy as in cis-PA (Figure 6.11) for the excess broadening, as found in Figure 6.36 [6,80,82]. This figure also demonstrates that in trans-(CD)$_x$ with the hyperfine constant as small as one-tenth in trans-(CH)$_x$ such an anomaly is not found down to 3 MHz, in agreement with the above conclusion. Another prediction is that the ratio of enhancement by an addition of a $bS_\pm I_\mp$ term to the $aS_z I_z$ term is found to be 0.5 which agrees very well with 0.56 ± 0.09 estimated by Figure 6.36. Finally, let us estimate the maximum spin density in the neutral soliton distribution from the cross-over frequency of 5–6 MHz. One gets $A\rho_{max} = 10$–12 MHz, then, $\rho = 0.15$–0.17 spins/carbon [192] at the central spin density using the same value $A = -70$ MHz as for the ENDOR experiment (see, section 3.2.3), which is in close agreemnt with $\rho_{max} = 0.17$ estimated by the ENDOR experiment [7,104]. The above good agree-
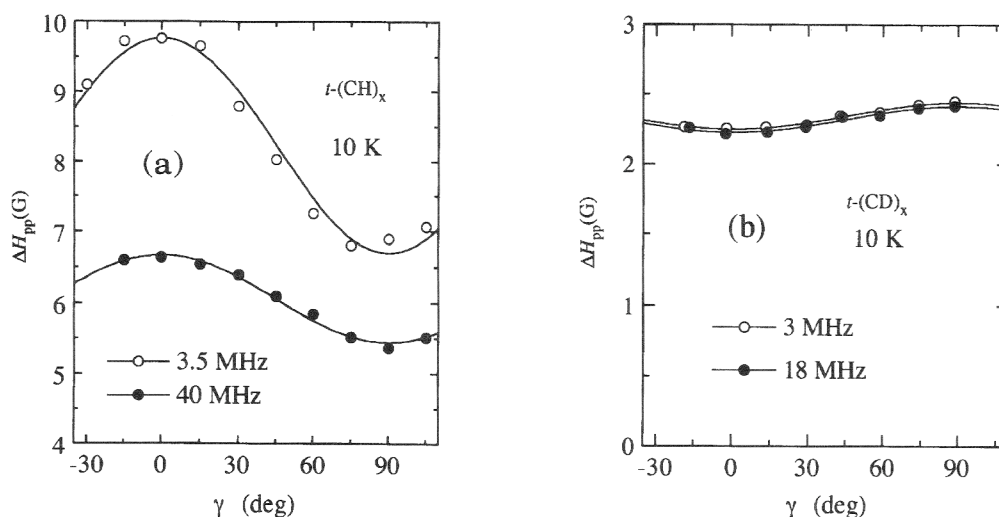
Figure 6.36. The angular dependence of the ESR linewidth in (a) *trans*-(CH)$_x$ at 10 K, 40 MHz (●, without the excess width) and 3.5 MHz (○, with the excess width) and (b) and *trans*-(CD)$_x$ at 10 K, 18 MHz (●) and 3 MHz (○) [6,80,82]. Note that the excess linewidth shows the same phase of pattern as that for *cis*-(CH)$_x$, the same as the width due to trapping (compare with Figure 6.11). Reproduced from Synth. Met. **28** (1989) D393–8.

ments support the validity of the analysis of ESR linewidth as a function of frequency.

4.3.4 Phase memory time T_M and motional narrowed width $(\gamma_e T'_{2e})^{-1}$

The spin-echo decay (phase memory) rate T_M^{-1} [159–161,193,194] at the X-band in units of G is shown for *trans*-(CD)$_x$ in Figure 6.37 together with the motional narrowed secular linewidth $(\gamma_e T'_{2e})^{-1}$ [6,82] obtained by fitting the ESR linewidth in Figure 6.33 to the relation (6.19). By definition, $(\gamma_e T'_M)^{-1}$ is expected to equal $(\gamma_e T'_2)^{-1} + (\gamma_e T'_1)^{-1}$. Substantially, $(\gamma_e T'_M)^{-1} = (\gamma_e T'_2)^{-1}$ holds at the X-band, since $(\gamma_e T'_1)^{-1}$ at the X-band is less than one-tenth of $(\gamma_e T'_2)^{-1}$ at all the temperatures measured [6,82]. Such a condition looks likely to hold below 100 K as found in Figure 6.37. The interpretation of the frequency independent width, ΔH_{trap} in (6.19), is consistent with such an observation, that is, ΔH_{trap} is an inhomogeneous broadening due to the trapping and then it can be eliminated by the pulse sequence to measure $(\gamma_e T'_M)^{-1}$. However, Figure 6.37 demonstrates a marked deviation from such an expectation. $(\gamma_e T'_2)^{-1}$ shows a broad peak around 100 K and monotonously decreases up to 300 K. However, the two different data sets of $(\gamma_e T'_M)^{-1}$ grow over $(\gamma_e T'_2)^{-1}$ above 100 K and approach the cw ESR linewidth consisting of ΔH_{trap} in addition to $(\gamma_e T'_2)^{-1}$,

as shown by the solid curve in Figure 6.37. Here, let us consider the reasons for such a deviation from the expected.
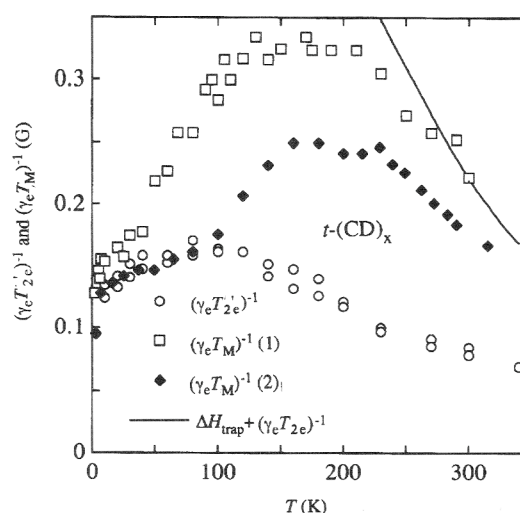
Figure 6.37. The temperature dependence of the motional narrowed secular width $(\gamma T_2')^{-1}$ (○) [6,82] and the phase memory time T_M (taken at X-band) in *trans*-(CD)$_x$ obtained by (1) Shiren *et al* (□) [159–161] and (2) Isoya (●) [193]. The solid curve shows typical behaviour for $(\gamma T_2')^{-1} + \Delta H_{trap}$. At temperatures lower than 100 K, $(\gamma T_M)^{-1}$ coincides with the secular width $(\gamma T_2')^{-1} \sim (\gamma T_2)^{-1}$ at X-band. At temperatures higher than 200 K however, $(\gamma T_M)^{-1}$ is governed not only by the secular width $(\gamma T_2')^{-1}$, but also by ΔH_{trap}. (after [82])

Below 100 K it is natural to interpret that the average time at the trapping site τ_{trap} is longer that T'_{2e}, which is a required condition for T_M to eliminate a static local field. On the other hand, around 300 K, it is also reasonable to consider that τ_{trap} becomes fairly shorter that T'_{2e}. Such a short τ_{trap} makes $\Delta H_{trap}(T)$ a time-dependent random field that cannot be cancelled out by the pulse sequence for T_M. Therefore, the condition $\tau_{trap} \approx T'_{2e} \approx 1$ μs would be realized at the cross-over temperature below 100 K. Such a criterion is consistent with the appearance of the anomalous broadening below 5–6 MHz where the other criterion $|\Delta\rho|/2 \approx 2 \times 10^7 \gg 1/\tau_{trap} \approx 10^6$ s^{-1} is required to hold. Finally, there is no discrepancy between the secular width $(\gamma_e T'_2)^{-1}$ and the spin-echo decay rate T_M^{-1} and these are fully consistent with the diffuse/trap model.

4.3.5 Multiple-quantum spin coherence experiment

Thomann and co-workers have reported that all of the spins are localized in 99% ^{13}C enriched trans- and cis- (accurate composition is cis/0.8–trans/0.2) polyacetylene, studied by the multiple quantum NMR (MQNMR) detected by the ESE-technique [165,186]. This is, however, clear experimental evidence demonstrating the validity of the diffuse/trap model [6,82].

Three pulses $\pi/2$-τ-$\pi/2$-τ_1-$\pi/2$-τ_2 were applied to the electron spin, i.e., the neutral soliton, to induce a ^{13}C MQNMR transition only in nuclei coupled to the soliton. They have found qualitatively the same spectra for trans-(CH)$_x$ and cis-(CH)$_x$ at 4 and 298 K, as shown in Figure 6.38, demonstrating that the observed spins coherently coupled with about 13 carbon nuclei

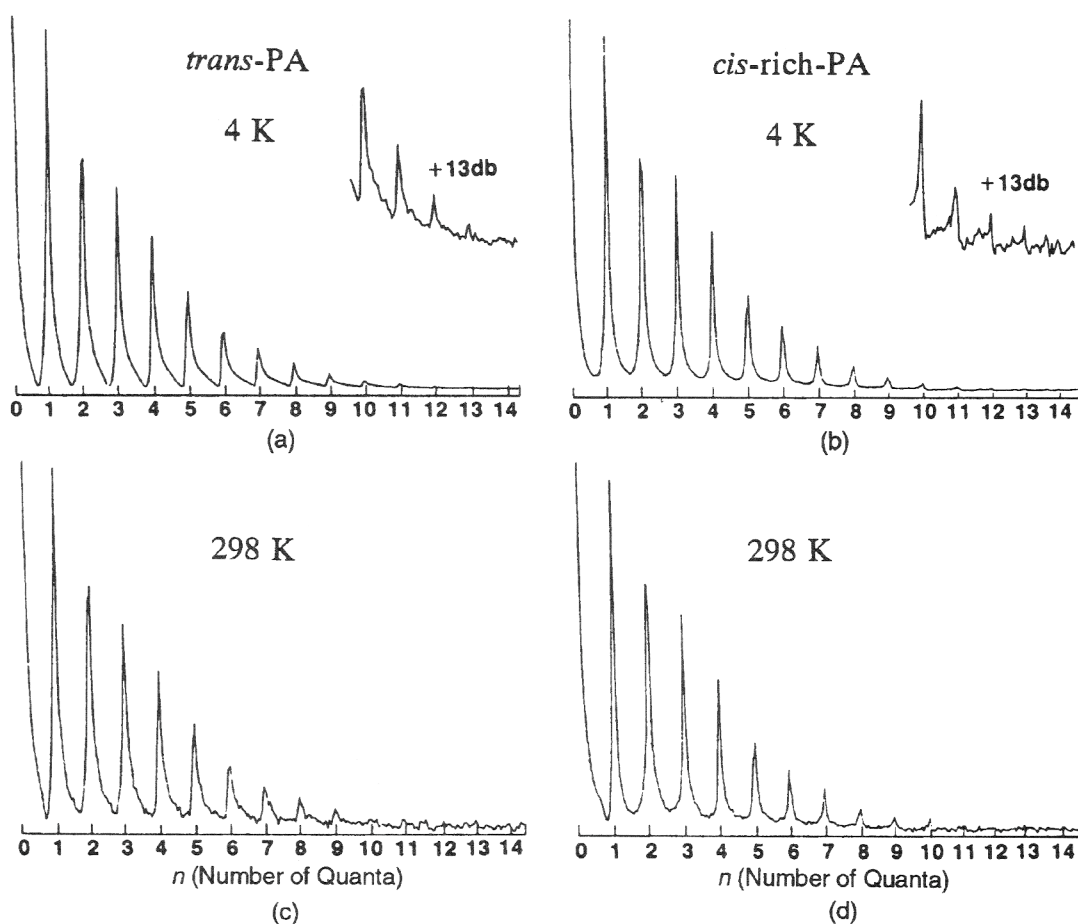
Figure 6.38. ^{13}C multiple-quantum (MQ) NMR excitation spectra for 99% ^{13}C-enriched trans-(CH)$_x$ at: (a) 4 K; and (c) 298 K and for cis-(CH)$_x$ composites (cis: 0.8 and trans: 0.2) at: (b) 4 K and (d) 298 K [165,186] (after [165])

under all the studied conditions and that as a result the shape of the neutral soliton is concluded to be the same as in each isomer. Another point concluded from this experiment [6,82] is that the diffusive spins do not contribute to the MQNMR spectra if the correlation time of motion is shorter than the hyperfine constant, since the hyperfine coupling is decoupled by rapid motion with short correlation time, that is, they need to couple each other longer than the inverse of the coupling constant.

The reason why the authors of [165,186] concluded that 'all' the spins were trapped, instead of the above fact, was that the ESR signal composed of only a single species, which requires that 'the observed' MQNMR signal should be 'all' of the present spins. However, the diffuse/trap model is required to interpret the ESR linewidth as a function of both frequency and temperature [6,82]. Such a model is compatible with the MQNMR result, namely, 'all' of the spins have a chance to contribute to the MQNMR signal in terms of a time sharing between the diffusing and the trapped states. Then, MQNMR data does not demonstrate that 'all' the solitons are trapped, but shows the existence of the trapped solitons even at 298 K, as expected from the diffuse/trap model. It is concluded from $\Delta H_{trap}(T)$ that around 10% of the neutral solitons are in the trapped state even at 298 K as shown in Figure 6.39 [6,82]. To account for the temperature dependence of the ΔH_{trap}, a trapping potential as large as up to 650 K was

Figure 6.39. The temperature dependence of the width due to trapping ΔH_{trap} (the constant contribution in Figure 6.33) in trans-$(CH)_x$ (●) and trans-$(CD)_x$ (○) and the correction factors Q of the trapping for T_{1e}^{-1}; the broken curve, $c_{diff} = 1 - c_{tr} = Q_h$ for the hyperfine interaction and the solid curve, $Q_d = 1 + 0.83c_{tr} - 1.83c_{tr}^2$ for the electron–electron dipolar interaction [6,82].

proposed [147], which assures that the solitons stay for long enough in the deepest trapping potential to join the MQNMR signal even at room temperature.

Thus, the MQNMR technique is shown to be useful as another way to determine the number of solitons in the trapped state at each temperature, to check the diffuse/trap model quantitatively. Actually, the reported MQNMR in trans-$(CH)_x$ has a higher signal-to-noise ratio than in cis-$(CH)_x$ at 4 K, consistent with a probably higher spin concentration in trans-$(CH)_x$ than cis-$(CH)_x$ as shown in Figure 6.38. At 298 K, however, trans-$(CH)_x$ shows lower signal-to-noise ratio than cis-$(CH)_x$, suggesting rapid diffusion for more than 90% of the neutral solitons, in other word, for 90% of the time ratio in trans-$(CH)_x$.

Therefore, the MQNMR result, together with the DNP, T_{1H}^{-1}, T_{1C}^{-1}, ESR $\Delta H(T,H)$, FID and T_M^{-1} are consistent with the diffuse/trap model.

4.3.6 ESR spin-lattice relaxation rate T_{1e}^{-1} at X-band

Robinson and co-workers have analyzed ESR T_{1e}^{-1} as a function of temperature measured at 9.5 and 16 GHz and as a function of frequency at rt, as shown in Figure 6.34 [164]. They assumed a model that the mechanism for T_{1e}^{-1} is the modulation of the electron–electron dipolar interaction due to scattering of the spins by acoustic phonons. They also assumed two levels of diffusion: (1) almost free rapid motion within a domain of ~ 50 carbons as proposed by the ENDOR analysis in an unoriented ^{13}C enriched sample [117], which dominates the ESR T_{1e}^{-1} at the X-band; and (2) slow migration of such a domain which assures compatibility with the motional narrowing of the ESR linewidth. The rapid diffusion within the domain is not of activation type and the diffusion rate increases with decreasing temperature. On the contrary, the migration is of activation type. However, such an analysis of the ENDOR data [117] was pointed out to be incorrect in section 3.2.5 [105]. Then, it is probable that this model will give rise to some inconsistency with other observations as follows.

This model is incompatible with anomalous broadening below 5–6 MHz in trans-$(CH)_x$ [6,80,82] and the previously mentioned MQNMR result [165,186]. On the ESR linewidth in trans-$(CH)_x$ as shown in Figure 6.33, the anomalous excess broadening ascribable to the hyperfine coupling as the 'like spin' (see, section 4.3.3) appears below 5–6 MHz and yields the estimation of the maximum spin density of the soliton as
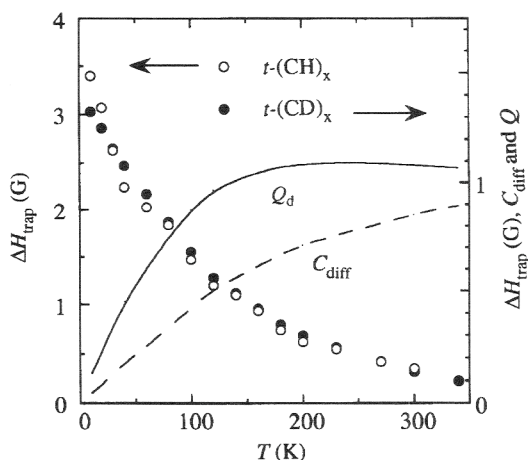
$\rho \approx 0.15–0.17$, in close agreement with the ENDOR estimation [7,104]. Provided that the spin dynamics are similar in $(CH)_x$ to $(CD)_x$ (as will be mentioned in the next section) such an anomalous broadening meets the requirements of a long coupling time, more than 0.1 µs, between the election and the proton spins and larger effective coupling constant, more than 5–6 MHz, filled up by the diffuse/trap model. Free motion within 50 carbons yields only $|A\rho m_H| \approx 70/2/50 \approx 0.7$ MHz ($m_H = \pm 1/2$) at maximum, which is too small compared with $5 \sim 6$ MHz, and the required duration to interact between them, 0.1 µs, is too slow to explain the extremely rapid ballistic-like motion at 4 K as a metal. Similarly, MQNMR data also requires static coupling between the electron spin and the proton nuclear spin for a longer time than the hyperfine coupling strength, the same as the anomalous broadening case below 5–6 MHz. These two data predict that T_{1e}^{-1} will die out at low temperatures because of disappearance of diffusing spins due to trapping, on the contrary, this model predicts because of increasing motion.

As a conclusion, the whole temperature dependence of T_{1e}^{-1} at the X-band cannot be ascribed to only the Q-1-D diffusive motion or the model by [164]. Denis and co-workers suggested more complicated relaxation mechanisms for $trans$-$(CH)_x$ at the X-band [191]. Thus, a complete interpretation of T_{1e}^{-1} at the X-band in the whole temperature range is still open to question. From the situation of the diffuse/trap model one can predict T_{1e}^{-1} behaviour below 100 K and at high frequencies, such as at X-band that the effect of the finite extension of the soliton severely suppresses the relaxation following the $\exp(-1/T^n)$ rule [6,185]. Such a suppression and the observation that $T_{1e}^{-1} \propto \omega^{-1}$ at the X-band and low temperatures [151] implies that far enough below 100 K the Q-1-D relaxation dies out and other relaxation mechanisms, for example via phonons, dominate the observed relaxation.

4.4 Diffusion rates and cut-off frequency

The on-chain diffusion rate $D_\parallel$ obtained by ^{1}H NMR T_{1H}^{-1} [147,189,190,195] and ESR linewidth in $trans$-$(CH)_x$ and $trans$-$(CD)_x$ [6,79,80,82,156] are shown in Figure 6.40 as a function of the temperature, obtained by the analysis in terms of the diffuse/trap model. Here, the solid curves shows $D_\parallel$ without a correction for the trapping effect obtained from the ESR linewidth, whereas the other symbols include it. Note that $D_\parallel$ above 100 K is almost free from the trapping effect. A power-law behaviour T^n with $n \sim 2$ is a common
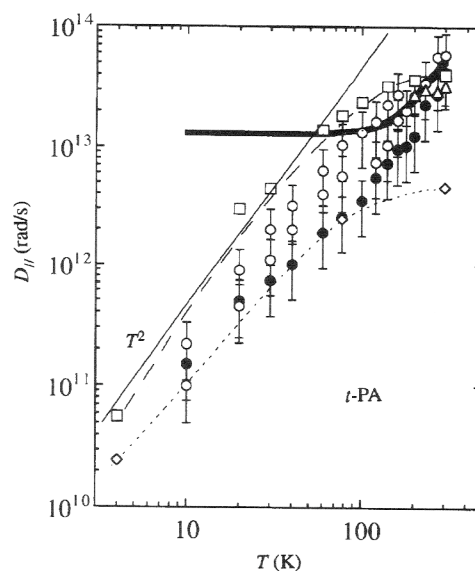
Figure 6.40. The temperature dependence of the diffusion rate along the chain, $D_{//}$, obtained by ESR for: $trans$-$(CH)_x$ (●) [80]; and $trans$-$(CD)_x$ (○) [79]; (△) [156]; by ^{1}H NMR for: $trans$-$(CH)_x$ (□ and the broken curve) [147]; (◇ and the dotted curve) {189,190,195] and the theory [197]. The solid curve, indicating $D_\parallel$ for $trans$-$(CD)_x$ before the trapping correction, shows a negligibly small contribution due to trapping above 100 K

feature of these data sets, at least at low temperatures, in spite of large scattering of the data. The positive coefficient of the temperature dependence $\partial D_\parallel/\partial T > 0$ suggests that the diffusion is not a free ballistic motion at low temperature and that there is some weak but finite localizing potential for the neutral soliton and that the driving force of the neutral soliton diffusion is of phonon scattering. At high enough temperatures where the energy of the soliton exceeds that of the phonons, soliton motion would be limited by a momentum exchange between the soliton and phonons which works as a viscosity [196]. Detailed theoretical considerations of the neutral soliton diffusion in the $trans$-polyacetylene have been reported from different approaches [176–178,197–199].

It is important to know that the result from proton NMR is consistent with that from ESR. If we take into account a quantitative large ambiguity induced from the diffuse/trap model (especially in proton NMR, almost the entire temperature dependence is governed by the trapping effect), this consistency is satisfactory and suggests that both methods detected the same phenomenon, in spite of the criticism that $1/\sqrt{\omega}$ dependence observed by proton NMR could come from a relaxation

mechanism other than the neutral soliton diffusion [159,160].

Spin dynamics studies of the neutral soliton in *trans*-PA with limited conjugation length have been carried out [200,201]. The effective conjugation length was modified by introduction of artificial sp^3 defects and was confirmed by ^{13}C NMR. The ESR linewidth and T_{1H}^{-1} are found to increase with increasing sp^3 concentration, which is interpreted as an indication of slowing down in the diffusion rate. Qualitative change of spin dynamics was clearly demonstrated but it is noteworthy that the effect of trapping was not taken into account in the analysis, whereas such a high concentration of sp^3 defects makes the trapping model unambiguous in these materials, that, is, the soliton always sits on the sp^3 defects or diffuses along the chain with the sp^3 defects, since the full width at half height of the neutral soliton reaches 18 CH units as concluded in section 3.2.3.

Figure 6.41 shows the temperature dependence of the cut-off frequency $1/\tau_\perp$ obtained by NMR $T_{1\rho}$ [146], T_1 [151,190] in *trans*-$(CH)_x$ and ESR in *trans*-$(CH)_x$ [80] and *trans*-$(CD)_x$ [79]. The cut-off frequency $1/\tau_\perp$ shows a weak temperature dependence with a minimum around 200 K. Since the diffusion rate $D_\perp$ across the chains is equal to or smaller than the cut–off frequency, an anisotropy of the diffusion rate is fairly large, ranging from $\geqslant 3 \times 10^3$ at 4.5 K to $\geqslant 8 \times 10^5$ at 300 K. Such an anisotropic diffusion in *trans*-polyacetylene is consistent with the topological nature of the neutral soliton. Although highly one-dimensional diffusion looks to be inconsistent with the observed Lorentzian lineshape, which is usually expected for the three-dimensional system, it can be shown to be consistent with the observed Lorentzian in the case of a larger cut-off frequency than the ESR linewidth [172].

It is interesting to consider the origins of the cut-off frequency, because a topological kink of the neutral soliton is essentially localized on the chain. Possible origins are due to (1) an exchange interaction between the electron spins [202] and (2) soliton hopping from the neutral soliton to the charged soliton proposed by Kivelson [203].

The temperature dependence of $1/\tau_\perp$ is explainable qualitatively as follows. In the temperature range below 100 K, the exchange interaction between the solitons would govern $\tau_\perp$: at the lowest temperature, almost all of the neutral solitons are trapped, probably several solitons gather around the absorbed oxygen on the surface of a fibril, which enhances the exchange interaction between them as an origin of the $1/\tau_\perp$ [202]. With increasing temperature, the neutral solitons start to diffuse rapidly, which decreases the efficiency of the exchange interaction between the neutral solitons. In the higher temperature range, the neutral soliton hopping via the charged solitons, assisted by a phonon, would become dominant. Kivelson has suggested a strong temperature dependence for the conductivity $\sigma \propto T^{13}$ in this mechanism, which is similar to the rapid increase of $D_\perp$ around room temperature. However, a serious question of the validity of this model has been raised [18].
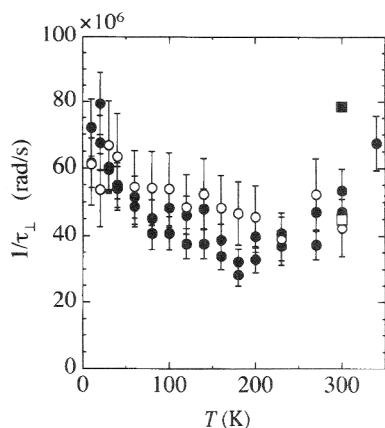
Figure 6.41. The temperature dependence of the cut-off frequency τ^{-1} by NMR: $T_{1\rho}$ (□) [146]; T_1 (■) [151,190]; in *trans*-$(CH)_x$ and ESR in *trans*-$(CH)_x$ (○) [80], and *trans*-$(CD)_x$ (●) [79]. The definition of $\tau_\perp^{-1}$ is given by (6.21)

5 SUSCEPTIBILITY IN DOPED POLYMERS

In conducting polymers, usually both the temperature-dependent Curie and the temperature-independent Pauli spins (mole susceptibility), $\chi = \chi_c + \chi_p = C/T + N_0 \mu_B^2 N(E_F)$, are observed, where N_0 is Avogadro's number, μ_B the Bohr magneton, C the Curie constant per mole-C/mole-monomer and $N(E_F)$ the density of states per unit energy (eV) for both spin direction per atom/monomer unit. The Curie spins are a clear indication of non-interacting localized spin species such as: (1) neutral solitons [169] in the degenerate ground state polymers represented by *trans*-PA; (2) polarons and bipolarons (see Table 6.5) playing a main role [170,204,205] in the non-degenerate ground state polymers such as polyparaphenylene (PPP), polypyrrole (PPy) and poly(phenylenevinylene) (PPV); and (3)

other magnetic impurities in the samples. The Pauli spins are generally an indication of degenerate spin systems as in the simple metals. Here, it is worth noting that the Pauli susceptibility is not necessarily temperature independent, in particular narrow band systems and strongly electron/lattice interacting systems [206,207]. In this chapter, the density of states at the Fermi level per unit energy for both spin directions defined by $N(E_F) = \chi_p/N_0\mu_B^2$ is used. It should not be confused with an alternative definition of the density of states for one spin direction: $N(E_F) = \chi_p/2N_0\mu_B^2$ (N.B. the former definition for the calculated values [208,209], but the latter in the formula).

There are several methods of measuring the susceptibility: susceptometers (microbalance, SQUID and so forth) and ESR and Schumacher–Slichter (ESR-NMR, S-S) techniques [210]. When using these methods, it is important to know their advantages and shortcomings. Since the susceptometers measure total susceptibility including para, ferro, antiferro and diamagnetic susceptibilities, arising from several possible origins, contributions other than specific spin species need to be subtracted, which limits the accuracy of the resulting spin susceptibility. In particular, residual oxygen molecules yield a paramagnetic contribution of around 30–50 K as an anomalous peak that sometimes causes a misleading interpretation of the susceptibility as a function of temperature. On the other hand, the latter two methods give the spin susceptibility uniquely but they also risk missing signals with broad linewidths (more than the limit of detection) as in the case of polyacetylene doped with iodine [211]. In ESR studies with an external reference, the lineshape should be noted, such as Dysonian, a characteristic of the metallic samples caused by short skin depth [212,213], and mixing of the dispersion mode, because they cause a definite error in the integrated intensity. Since the last S-S technique uses an internal reference, ^1H or ^{19}F in the sample itself [210], the spin susceptibility can be obtained with no knowledge of the mass of the sample. This technique, however, requires the measurement of NMR and ESR at the same and at low frequency, such as several tenths MHz, which limits the ESR sensitivity. Therefore, the method of measuring the susceptibility should be selected to match the characteristics of the samples.

Finally, it is important to note that Helium gas is needed for thermal contact between samples and coolant for experiments low enough below liquid nitrogen temperature and that other kinds of gas (Air, N_2, Ar, etc.) are ineffective enough below their boiling point for thermal exchange.

5.1 Susceptibility upon doping: degenerate ground state

In *trans*-PA, the Curie spins attributable to the neutral soliton rapidly decrease upon doping through conversion of the netural solitons to the charge solitons [168,206,211,214–216], whereas the Pauli susceptibility remains very small for values up to several % of the dopant concentration and then abruptly increases to approach about $\chi_p \approx 3 \times 10^{-6}$ emu/mole C or $N(E_F) \approx 0.1$ states/eV C as found in Figure 6.42 for a variety of dopants: AsF_6^- [167,168,217]; I_3^- [206]; Na^+ [214,215,218,219]; ClO_4^-[220]; and Br_3^- [221]; Naarmann and Theophilou-PA (NT-PA) doped by I_3^- [222] and Tsukamoto-PA (T-PA) doped by I_3^- [66,67,223].

It is noteworthy that for *trans*-PA-AsF_6^- doped with a special procedure for a homogeneous doping [167,168], and for Na^+ and ClO_4^- doped with an electrochemical technique [214,215,218,219], χ_p steeply rises up around 5%, but gradually does for I_3^- [206] and Br_3^- [221]. This tendency is further enhanced in the case of *cis*-PA doped with AsF_6^- where χ_p increases proportionally with the dopant concentration y, ascribed to inhomogeneous and percolative doping [224]. In the *trans*-PA-I_3^- case [206], as shown by the open circle with $y = 4.4\%$ in Figure 6.42, the small χ_p was obtained also applying the special procedure for the homogeneous doping [168,216,217], in agreement with the AsF_6^- [167,168], Na^+ and ClO_4^- [214,215,218,219] cases. Thus, it is believed that below about 5% of dopant the electrical conduction is carried by the spinless charged carriers, and the observed lower threshold than 5% for the appearance of the Pauli spins is resulted from such an inhomogeneous doping [206,225]. The authors in [214,215,219] proposed a presence of first-order phase transition from semiconductor to metal; from the spinless charged soliton in the intermediate doping range below 5% to the polaron lattice with the Pauli susceptibility in the heavily doped range above 5% [226–228]. However, the infrared-active vibrational (IRAV) modes experiment yielded no evidence for such a polaron lattice, but for no simple metal with an optical gap of 0.2 eV [225,229,230].

For *trans*-PA doped with I_3^-, χ_p shows particularly large values up to three times larger than the others, which is interpreted as a suggestion of some modification in the electronic states, that is, the density of states increased by a factor of three [223], and/or of the possibility of more homogeneous doping (less material remaining in the soliton doping level regime)
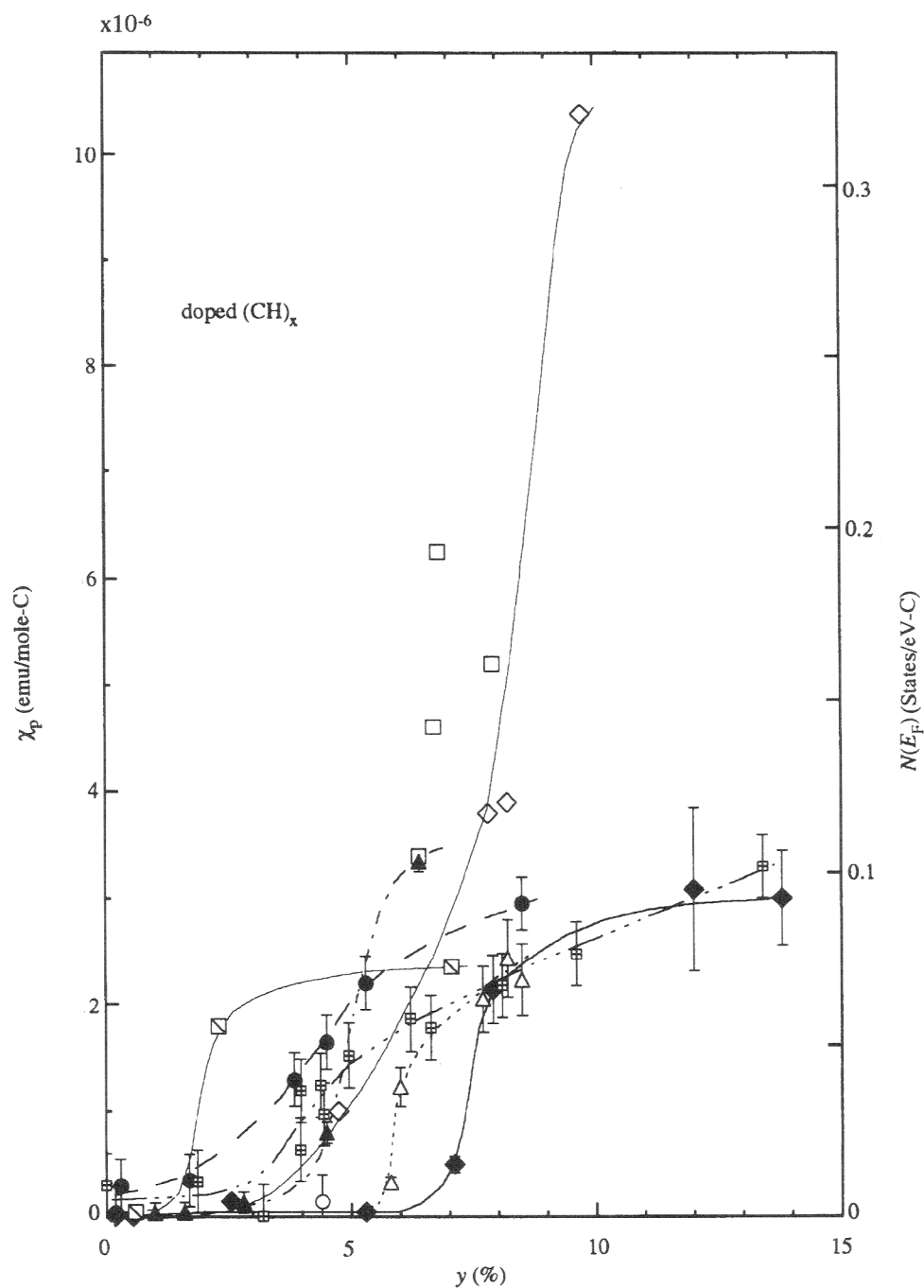
Figure 6.42. The Pauli susceptibility χ_p per mole-carbon and the density of states $N(E_F)$ at the Fermi energy per carbon atom for both spin directions: $N(E_F) = \chi_p/N_0\mu_B^2$, where N_0 is Avogadro's number. S-PA doped by AsF_6^- homogeneously ($\blacklozenge$ and the solid curve) [167,168], I_3^- rapidly ($\bullet$ and the broken curve) and homogeneously ($\bigcirc$) [206], Na^+ electrochemically ($\diamondsuit$ and the dotted curve) [215,219], ClO_4^- ($\blacktriangle$ and the dash-dot curve) [220] and Br_3^- ($\boxplus$ and the dash-3 dots curve) [221], Naarmann and Theophilou-PA (NT-PA) doped by I_3^- ($\boxdot$ and the thin solid curve) [222] and Tsukamoto-PA (T-PA) doped by I_3^- ($\diamondsuit$ and the thin solid curve) [223], ($\square$ squares) [67].

[66,67,231]. If the former is the case, a simple consideration shows us that the thermoelectric power, inversely proportional to the density of states, would give smaller values by a factor of up to three than N-PA and S-PA, but not [67] and the thermoelectric power data favours the latter. The other point to which attention should be paid, is the measurement itself. Generally speaking, the SQUID susceptometer requires caution, that is, it measures total susceptibility including the diamagnetism of both the polymer and the dopant which should be subtracted from the observed to obtain the spin susceptibility.

In the case of cis-PA, the number of Curie spins shows a peak around 1 mole % of doping due to the sum of increasing and decreasing contributions [232]. The increase results from doping induced cis-to-trans isomerization that produces the neutral solitons and the decrease results from the conversion of the neutral solitons to the charged solitons.

5.2 Susceptibility upon doping: non-degenerate ground state

In the non-degenerate polymers, the susceptibility as a function of doping concentration is complex and controversial, which correlates to the evolution of the elementary electronic excitations upon doping. At low doping concentration the Curie spins increase with dopant concentration if the polaron has stable elementary excitation, but less Curie spins will be observed if the bipolaron does [128,129,170,233–237]. A variety of observations were reported for various polymers with various dopants, probably due to a counterbalance of several effects: the formation energy of polarons and bipolarons; the electron correlation effect; the interchain coupling strength; the dopant species and the effect of disorder.

In PPy-ClO_4^-, Scott et al. found a strong sharp (0.2 G) ESR in as-grown film, but no spins in conducting form aftrer cycling up to five times, electrochemically, without a change of conductivity, ~15 S cm [238–240]. Kaufman et al. Reported a gradual decay of ESR intensity with a long time constant of 10^3s, suggesting a metastable nature of the spin carriers, contributing to structural disorders and defects [241,242]. However, a maximum number of spins, ≈1/10 of the pyrrole ring, was found at around 17% of ClO_4^- with a shorter time response of the order of 1s by Genoud et al. [243]. Such a peak behaviour as a function of dopant concentration, indicating a change from polaron nature at low doping to bipolaron at high

doping, was interpreted by a statistical model of the polaron and bipolaron [244,245]. To understand the PPy-ClO_4^- system, it is important to take into consideration that not only severe disorder including α–β linkages compared with PT [246–248], but also reactivity of the N site, dehydrogenation and oxygenation reactions [246], and instability of the ClO_4^- ion resulting in addition of the Cl^- ion to the polymer backbone [249–251]. Recent observation of higher electrical conductivity could be achieved by controlling conditions to suppress such side reactions and selection of a more stable dopant [252,253].

Kaneto et al. obtained a maximum number of spins at around 3% of BF_4^- dopant by an ESR study in PT, suggesting a cross-over from polaron to bipolaron around 3% [254]. On the other hand, a fairly small number of spins was reported in PT doped by iodine [255,256]. Chen et al. found only a vanishingly small ESR signal in PT doped electrochemically with ClO_4^- up to 14%, suggesting a bipolaron ground state [257].

Schärli et al. Reported a thorough study of ESR in polymethylthiophene (PMeT) doped with BF_4^-, and stressed that the number of Curie spins increases linearly with the number of charges injected by up to 10% of the dopant concentration [258]. However, such a conclusion leads us to an unrealistically large value for the Pauli susceptibility in 25% doped PMeT; $\chi_p \approx 4 \times 10^{-5}$ emu/mole C (deduced by the present authors assuming 1 g/cm^3 for the specific density of PMeT) that corresponds to the density of states at the Fermi level of more than 1 state/eV C, (about ten times larger than the other conducting polymers as shown in Table 6.6. Kume et al. also found a linear increase in the number of Curie spins in PPP doped with AsF_6^-, but a rather smaller value of 0.3%/ring at maximum was obtained at 10% doping level [259]. In unstretched PPV film doped with AsF_6^-, a linear relationship between the number of spins and the doping concentration was also reported and the number of spins was 2.5% per ring at maximum, around 50% doping [260].

In PANI protonated with HCl (protonation is a kind of doping; an imine of the polymer backbone makes a bond with a proton, resulting in a free charge on the backbone locally neutralized by a chlorine ion near the chain, keeping the number of electrons on the backbone constant), morphology and crystalline form were found to affect the evolution of susceptibility upon protonation [261]. In a powder form of PANI, called EB-I (emeraldine base) for the insulating base form and ES-I (emeraldine salt) for the conducting salt form, both the Curie and Pauli susceptibilities are found to increase

Table 6.6. The density of states at the Fermi level, $N(E_F)$, in heavily doped conducting polymers in units of states/eV/(C+N) for two spin directions. (C+N) means to divide by total number of carbons and nitrogens, except for side chains, in the monomer unit. $\chi_P = N_0\mu_B{}^2 N(E_F) = 3.24 \times 10^{-6}$ emu/mole-C corresponds to $N(E_F) = 0.1$ sts/eV/(C+N), where N_0 is Avogadro's number and μ_B is the Bohr magneton

Dopant	PA	PPP	PPy	PT	P3AT	PANI	PPV
$AsF_6{}^-$	0.1 [168]	0.05 [259] 0.03 [319]	0.09 [282]	0.23 [255] 0.05 [279] 0.11 [282]			
$I_3{}^-$	0.09 [206]			⩽ 0.02* [255]	0.01 [297]		
$PF_6{}^-$			0.18 [281] 0.13 [282]		0.08 [282]		
$ClO_4{}^-$	0.12 [220]		0.10 [282]	0.12 [296]	0.09 [282]		
$BF_4{}^-$			0.05 [279] 0.08 [282]		∼ 1.5 [258]	0.14 [266] 0.12 [266]	
TsO^-			0.05 [281] 0.08 [282]				
Cl^-						0.08 [261] 0.20 [278]	
CSA^-						0.04 [209]	
$HSO_4{}^-$			0.06 [282]			0.19 [303]	0.05 [307]
$Br_3{}^-$	0.1 [221]						
$Na^+(K^+)$	0.07 [218]	(⩽ 0.03*) [316]					

* The maximum value estimated by the present authors. The underlined values were obtained by SQUID or microbalance and the others were by ESR.

proportionally with the protonation level, suggesting a percolative protonation [262,263]. While in EB-II and ES-II prepared by casting from N-methylpyrrolidinone (NMP) solution of PANI, mainly the bipolaron was observed at the low protonation regime, which is interpreted as doping in the amorphous region, and at high protonation regime the Pauli susceptibility step likely appear around $y \approx 0.2$–0.3 which is ascribed to the polaron lattice formed by doping into the crystalline region [261].

On the other hand, in the electrochemical redox study the number of spins was reported to show a peak as a function of redox potentials that corresponds to the doping concentration, which was explained by a crossover from the polaron to the bipolaron states [264]. Curiously, the behaviour depends strongly on the thickness of the films at higher protonation levels than such a peak; the thinner the film, the faster the decrease of the number of spins. The authors in [264] interpreted such results as the polaron states being stabilized by the

presence of higher disorder in thick films and the bipolaron states being stabilized with lower disorder in thin films [264]. Recently, two similar *in-situ* electrochemical studies were reported [265,266]. Genoud *et al.* found no Pauli susceptibility at the heavily doped state in the PANI-HCl system and concluded that the polaron and bipolaron equilibrium model based on their statistics was compatible with their data [244,245,265], whereas Mizoguchi *et al.* reached the conclusion that a cross-over from the polaron state at low doping regime to the Pauli-like state takes place in the PANI-HBF$_4$ system [266].

5.3 Temperature dependence of susceptibility

From the temperature dependence of the susceptibility, the nature of spins can be studied; isolated spins give the Curie-law as inversely proportional to the tempera-

ture, degenerated electrons show the Pauli susceptibility as independent of temperature and triplet pairs of electrons give thermally activated susceptibility. In most cases both the Curie χ_C and Pauli χ_P susceptibilities are observed. Possible origins for such behaviour are: (1) the coexistence of the neutral solitons/polarons and the Pauli spins due to inhomogeneous doping, as observed in powder PANI protonated by HCl [267]; (2) the same as (1), but due to the smallness of each metallic region, giving rise to the possibility of containing an odd number of electrons, as considered for PT, PMeT and PPy to be probable (also see Section 7); and (3) the single-spin species shows a cross-over from Curie to Pauli-like behaviour due to the effect of electron–electron correlation and disorder [209,235,268–270]. In the early stages of research on non-degenerate conducting polymers, the absence of the Pauli susceptibility is emphasized [271,272]. This is actually controversial in the lightly doped regime, as mentioned above, but it seems to be confirmed that the Pauli-like susceptibility is observed in most fully-doped conducting systems. Here, the Pauli-'like' susceptibility means 'temperature-independent' susceptibility but does not necessarily mean the presence of a well-defined Fermi surface. Polymer systems that show temperature-independent suscptibility are listed in Table 6.6, with the density of states calculated from the Pauli-like susceptibility.

Polyacetylene, having high crystallinity (70–80%), shows Pauli-like susceptibility with many species of dopants as demonstrated in Figure 6.42. In such cases other experiments which support metallic conduction are observed: almost linear thermoelectric power and (though in the limited range around 200–300 K) metallic temperature dependence of the dc conductivity with dopant of AsF_6^-, $FeCl_4^-$, $FSO_2OOSO_2F^-$, I_3^- and ClO_4^- [60,273–277]. However, since the non-degenerated polymers do not necessarily have enough high crystallinity, the Pauli-like susceptibility does not provide convincing evidence for the metallic electronic states. Temperature-independent susceptibility could be observed not only in the conventional metals, but also in a system having no delocalized electronic states at the Fermi energy, due to the Coulomb correlation and disorder [235,268–270]. They could be considered as a Fermi glass. In effect non-degenerate polymers involve the presence of disorder, that is, a disordered metal and a disordered semiconductor.

In the case of PPy the observation of the temperature-independent susceptibility has been controversial; some report its absence [241–243,248,278] and others its presence [208,251,279–282]. The origin of this dis-

crepancy is not clear yet, but probably depends on conditions for preparation of the samples [253,283] which can control the extent of disorder and does not depend on the magnetic field strength measured, as will be demonstrated in section 5.4. Examples of temperature-independent susceptibility are shown in Figure 6.43 for PPy doped with PF_6^- [208,281,282]; AsF_6^- [282]; ClO_4^- [282]; BF_4^- [282] and TsO^- (p-toluenesulphonate ion) [208,281,282] as a function of $1/T$. These systems show several indications of metallic electronic states: the electrical conductivity as high as 3000 S/cm [253]; the negative dielectric constant [208,281]; the small and linear thermoelectric power versus temperature [284,285]; a finite density of states at the Fermi energy studied by XPS and UPS [251] and the metallic temperature dependence of the ESR linewidth [282,286,287] ascribable to the Elliott mechanism [288] (see also section 7), in agreement with the metallic electrical conductivity obtained by a voltage-shorted-compaction (VSC) method [285,289], while it is also pointed out, for PPy-PF_6^-, to be a disordered metal near the M–I transition when synthesized at $-40°C$ or a Fermi-glass when synthe-
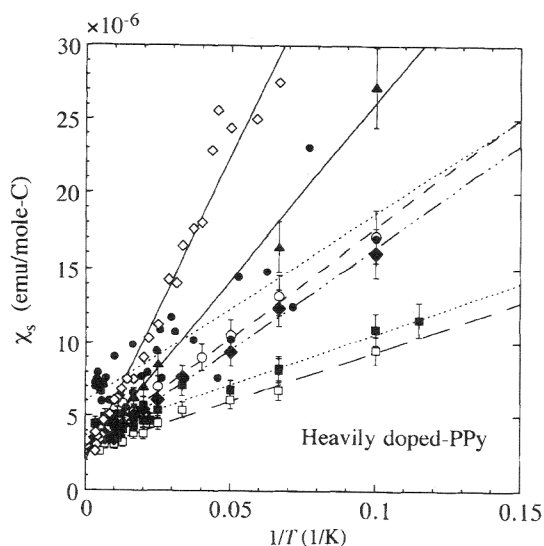
Figure 6.43. The spin susceptibility in PPy doped heavily with various dopants as a function of $1/T$. PF_6^- (SQUID, ● and the dotted line) [281]; p-toluenesulphonate (TsO^-) (SQUID, ◇ and the solid line) [281]; PF_6^- (S-S, ■ and the dotted line) [282], TsO^- (S-S, ▲ and the solid line) [282]; ClO_4^- (S-S, ○ and the short dashed line) [282]; BF_4^- (S-S, ◆ and the dash-3 dots line) [282]; and AsF_6^- (S-S, □ and the broken line) [282], where S-S means Schumacher–Slichter method [210]. The slope of the lines corresponds to the Curie constant and the intercept to the Pauli susceptibility.

sized at rt, from the reflectance measurement [283]. Therefore, most of the temperature-independent susceptibilities in PPy systems prepared at low temperatures are likely to exhibit the Pauli susceptibility. The densities of states at the Fermi level, $N(E_F)$ for the polymers appear in Figure 6.43 and are summarized in Table 6.6. The number of Curie spins is in the range of one spin per 300 (PPy-TsO$^-$, [281]) $\sim$ 2000 (PPy-PF$_6$$^-$, [282]) monomers. The observed single Lorentzian lineshape of ESR would not support an inhomogeneous doping hypothesis for the Curie susceptibility. In PPy-PF$_6$$^-$, as one possibility, the authors consider that, taking account of its metallic nature in the resistivity (in the meaning of small temperature dependence, less than about a factor of 2) down to the lowest temperature measured [290] and in the ESR linewidth dominated by the Elliott mechanism typical for metals (see section 7), the origin of the Curie spins is not due to localized states, but to the single unpaired electron created with the probability of 1/2 in metallic domains containing 1000 monomers on average, as observed in fine metallic particles [291,292].

The ESR susceptibility in PPy doped with polyanions, sulphated poly(β-hydroxyether), sulphated poly(butadiene) and benzene sulphonate ions, as an example of disordered conducting polymers, was reported by Chauvet et al., to show approximately a sum of the Curie and Pauli-like temperature dependence, but a small upturn above 200 K in some samples [293]. This behaviour is interpreted in terms of the thermal activation of the single bipolarons into their triplet state and such bipolarons are stabilized by bridging of adjacent chains through dopants [294], rather than of the usual interpretation in terms of the temperature dependent Pauli susceptibility [206]. The thermoelectric power of these systems shows small positive values, several μV, and square-root-like temperature dependence, typical for hopping systems with degenrate electronic states around the Fermi level [293].

At least in heavily doped polymers, the temperature-independent susceptibility is observed in PT and P3AT (poly(3-alkylthiophene)) doped with AsF$_6$$^-$ [255,279, 282]; PF$_6$$^-$ [282]; SO$_3$CF$_3$$^-$ [295]; ClO$_4$$^-$ [282,296]; and BF$_4$$^-$ [258], except for PT/P3AT-I$_3$$^-$ [255,297]. Possible reasons why it is not observed in PT/P3AT-I$_3$$^-$ are: (1) the ESR linewidth from the Pauli spins is too broad to observe by ESR; and (2) the charge transfer from iodine to polymer is insufficient to fill a band gap. The situation with these systems is similar to the case of PPy on the metallic electronic states; the electrical conductivity reaches 500 S/cm [298–300], the small

and linear thermoelectric power [289,301] and the metallic temperature dependence of the ESR linewidth [258,287,289,296,301] (see section 7), is also in agreement with the metallic conductivity found by VSC measurements [287,289,301]. Then, most of the temperature-independent susceptibilities in these systems also arise from the Pauli susceptibility in metallic electrons.

In PANI-CSA, Sariciftci et al. [209] measured the ESR susceptibility in samples sealed off under high vacuum; PANI-CSA film cast from an m-cresol solution; PANI-CSA powder and dilute solid solutions with PMMA (poly(methyl methacrylate)). They reported that in the ESR susceptibility the Curie law was predominant in PANI-CSA powder, on the other hand in the PANI-CSA film cast from m-cresol solution with the same powder, they observed the Pauli-like behaviour down to 50 K and then a change to a Curie-like increase below 50 K. They attributed the appearance of the Pauli term to the reduced extent of disoder in PANI-CSA film and interpreted the susceptibility of the film in terms of a model for doped semiconductor, obtaining 4–5 meV for the on-site Coulomb energy. Such a model [268,302] predicts a cross-over from the Curie-like behaviour at low temperatures to the Pauli-like one at high temperatures, resulting from the interplay between the effects of electron–electron interaction and disorder in the regime of Anderson localization. They claimed no Curie contribution above 50 K instead of the conventional Curie plus Pauli behaviour, that is, the unique spin species changes its electronic state from Curie to Pauli spins [209]. It is, however, generally difficult to conclude the definite absence of a Curie contribution, since it is not necessarily a special case for the Pauli susceptibility to depend on the temperature in strongly electron-lattice coupled system; [207]. This is one of the possible interpretations for susceptibility in conducting polymers.

In other PANI systems protonated with HBF$_4$ [266], HCl [261,278] and H$_2$SO$_4$ [303], temperature-independent susceptibility is observed. In PANI-CSA the electrical conductivity σ behaves as a metal, that is, $\sigma \propto 1/T$, above 200 K [304] and in PANI-HCl the microscopic conductivity obtained from the spin dynamics showed the semiconductor-to-metal transition around 150 K [305,306]. Furthermore, the metallic optical absorption was found in PANI-HBF$_4$ [280]. Then the temperature-independent susceptibility could be assigned to the Pauli susceptibility in these systems.

However, PANI-H$_2$SO$_4$ indicates a semiconducting behaviour not only in the dc conductivity, but also in the microscopic conductivity up to 300 K obtained by

the spin dynamics [303]. Such a result suggests the temperature-independent susceptibility observed in PANI-H$_2$SO$_4$ to be of Fermi glass that had arisen from the localized states near the Fermi level due to heavy disorder. A similar result is observed in unstretched PPV-HSO$_4^-$ [307]. It is known that the electronic states in PPV can be remarkably improved by mechanical stretching when converting a precursor film to PPV [308,309]. Such a stretching causes an extended chain conformation that provokes metallic extended electronic states, but a more coiled conformation in the unstretched one that localizes the electrons. Such a conformation of the chain is one of the important parameters to dominate the electronic states in the polymers [208,310,311]. Thus, the unstretched PPV-HSO$_4^-$ is also considered to be a Fermi glass system.

It is known that water molecules in PANI enhance the electrical conductivity several-fold [312]. Kahol et al. demonstrated that magnetic properties of PANI and its derivatives protonated by HCl are affected by heat treatment to remove water molecules from the sample [2,313–315]. They found a conversion of the Pauli-like spins to the Curie spins upon heating below 100°C, causing removal of the water molecule from the polymer, and de-doping of HCl well above 100°C, resulting in a steep decrease in both the Pauli and Curie spins [313,314].

5.4 Anomaly in susceptibility

In poly(p-phenylene) (PPP) doped with alkali metals, Li, Na, K, Rb and Cs [316–318], and AsF$_6^-$ [259,319–321], the susceptibility was investigated by ESR. A non-Curie susceptibility with a maximum around 10 K measured by ESR at the X-band was reported in PPP-yAsF$_6^-$ [320] and PPP-alkali metal systems by Kispert et al. [316–318], and was analyzed by them and Kahol and Mehring as thermal activation of the polaron pairs from the bipolaron ground state at low temperatures with around 10 K of antiferromagnetic exchange energy [316–318,320,322]. On the other hand, in PPP-yAsF$_6^-$ with y = 17.5, 9.8 and 4.7%, sum of the temperature-independent and Curie susceptibilities was observed by ESR at 18 G (51 MHz) as shown in Figure 6.44 [321]. The Pauli appeared above y ≈ 5% and the Curie reached one spin per 300 rings at y ≈ 10% [259]. It is noteworthy that there is no indication of non-Curie behaviour down to 2.4 K. The origin of the discrepancy between the two experiments is not clear yet. Although a similar non-Curie behaviour with a maximum around 20 K has been reported in PPy-
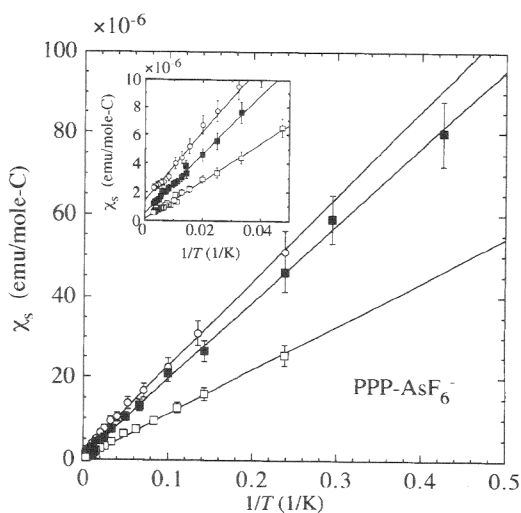

Figure 6.44. The spin susceptibility measured at 51.5 MHz in PPP doped with AsF$_6^-$ as a function of 1/T. The dopant concentrations are: 17.5% (○); 9.8% (■); and 4.7% (□) [321]. The inset is an expanded view for the Pauli susceptibility.

ClO$_4^-$ [286] which can be fitted with the same idea as the PPP case [322], it was corrected by the authors of [278] that it was not reproducible but that in this case the origin of the non-Curie behaviour is due to missing thermal contact between the sample and sample tube without Helium gas that is effective even at liquid Helium temperature. On the temperature-independent susceptibility, there is not enough data to conclude if it is an evidence for the degenerate Fermi electrons with the definite Fermi level or a Fermi glass system, and the extent of disorder would be a crucial parameter for these materials.

In PANI-HClO$_4$, Iida et al. observed Curie–Weiss plus thermally activated behaviour with ESR. The former, 1/(T + Θ) behaviour with several Kelvin of Θ at low temperatures shows a clear upturn above 150 K for as-prepared PANI-HClO$_4$, and a sign of similar behaviour was found for a redoped PANI-HClO$_4$ sample [323]. They interpreted such an upturn by a singlet (bipolaron)–triplet (polaron pair) equilibrium [323]. The present authors, however, would like to suggest another interpretation, similar to the case of P3MeT, to be mentioned later [295], that above 150 K, Pauli-like susceptibility appears, and below 150 K, such a Pauli-like susceptibility disappears because of some phase transition that opens an energy gap at the Fermi level, as suggested by several findings: anomaly around 150 K in the S–S susceptibility [266]; the spin dynamics analysis in PANI-HCl [305,306]; and a U-

shaped thermoelectric power with a minimum around 150 K in PANI-HCl [324,325] (refer to section 6.1.1). Small Weiss temperatures (Θ's) for the susceptibility are frequently observed in the polymer systems, attributable to a weak antiferromagnetic coupling between the Curie spins [282,314,323,326].

A similar anomaly and a similar interpretation were reported in the heavily-doped poly(2-n-butoxy-methoxy-1,4-phenylene vinylene)-I_2 (PBMPV, PPV derivative) by Lee et al. [327]. Both the ESR susceptibility and the linewidth have shown an anomaly around 180 K, which is similar to that in PANI-HClO$_4$ [323]. Another similar enhancement of the ESR susceptibility above 200 K and a peak in the linewidth around 200 K were also observed in poly(3-methylthiophene) (P3MeT) doped with $SO_3CF_3^-$, but not in poly(3-dimethylthiophene) (P3DMeT), by Tourillon et al. [295]. They pointed out a similarity with the metal-to-insulator transition, for example, in TTF-TCNQ, which is similar to the above mentioned possibility. An anomalous temperature dependence of the SQUID susceptibility in PPy-BF$_4^-$ [328] was also reported by Nalwa; a minimum around 80 K in PPy, which is suggested by him to be an indication of some phase transition.

Sariiftci et al. [329,330] have reported that the total susceptibility measured by a SQUID susceptometer in PPy-PF$_6^-$ shows the anomalous non-linear magnetization, saturating around ± 2 KG. Such behaviour was reproduced by the other group for PPy-PF$_6^-$ as shown in Figure 6.45 [282]. Figure 6.46 demonstrates that the initial slope (susceptibility) shows only a weak temperature dependence up to 300 K, which implies
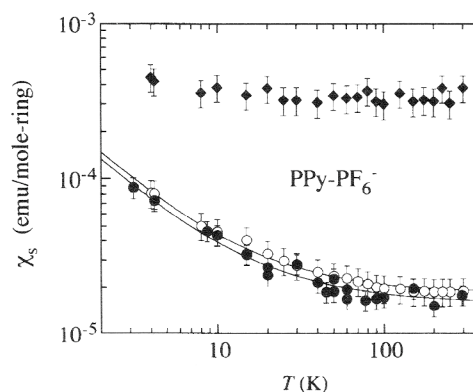

Figure 6.46. A comparison of the spin susceptibilities in PPy-PF$_6^-$ obtained by SQUID (up to 50 KG) ($\bigcirc$) and the Schumacher–Slichter (≈ 18 G) ($\bullet$) experiments [210]. They agree with each other to within 10% accuracy [282]. The solid curves show the least-square fitting with Curie + Pauli behaviour. In the SQUID experiment, a ferromagnetic-like contribution ($\blacklozenge$ indicate its initial slope) saturating around 2 KG is also observed as shown in Figure 6.45. The agreement between the SQUID result (except for the ferromagnetic one) and the S-S result, suggests that the magnetic field dependence is absent and the ferromagnetic one has not been observed in ESR.

that this anomalous magnetization is not superparamagnetic in origin. Figure 6.45 also indicates that the spin susceptibility obtained by the Schumacher–Slichter technique (SS) [210], at about 18 G agrees well with the spin susceptibility deduced from the SQUID data taken up to 5 T, by subtracting such an anomalous contribution from magnetization saturation at 300 K.
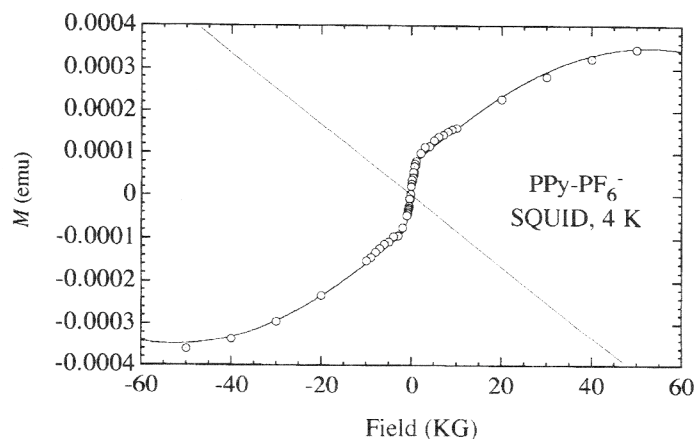

Figure 6.45. The magnetization curve at 4 K in PPy-PF$_6^-$ measured by SQUID [282]. The straight line shows a sum of the core-diamagnetism and the Pauli-paramagnetism. There are ferromagnetic-like steps around 2 KG and at the saturation of the Curie contribution, probably due to the polarons.

This result demonstrates that ESR with a narrow linewidth does not include such an anomalous magnetization [282].

5.5 Knight shift

Typical evidence for the metallic state by NMR is an observation of the Knight shift K [8,11,331] that is a field shift, or equivalently, a frequency shift of the NMR signal originating from the local magnetic field due to the Pauli paramagnetic spins through hyperfine couplings, defined by [8,11,331]:

$$K = \frac{\Delta f}{f_0} = \frac{\Delta H}{H_0} = \sum_i H_{hf}^i \frac{\chi_P}{\mu_B}, \qquad (6.23)$$

where Δf and ΔH are the frequency and the field shifts, respectively, f_0 and H_0 the resonance frequency and field, respectively, H_{hf}^i the hyperfine coupling constant in Gauss per μ_B and χ_P the Pauli susceptibility. In usual s-electron metals, there is a trend for the Knight shift to increase with increasing atomic number, going from 2.5×10^{-4} (250 ppm) for ^{7}Li to 2.5×10^{-2} (25 000 ppm) for ^{109}Hg. If the Knight shift in the conducting polymers is so large, experiments to check the metallic state in the conducting polymers are an easy task. Unfortunately, however, the expected Knight shift in the conducting polymers is extremely small, of the order of several ppm for doped polyacetylene, as demonstrated experimentally and theoretically [332,333], because of a small hyperfine coupling constant of several gauss [333,334] through an indirect polarization of the s-core by the π-conduction electron spins, which is compared with a direct contact coupling with the s-conduction electron, sufficiently larger than KG in the s-electron metals.

Then, actual NMR shift is expected to be governed by chemical shift due to the injected charges upon doping rather than by the Knight shift. The chemical shift of ^{13}C NMR is known to be about 160 ppm of the de-shielding or shielding shift corresponding to the π-electron density decrease or increase by one electron per carbon, respectively [335].

Peo *et al.* found a ^{13}C NMR de-shielding shift of 30 ppm accompanied by line broadening in AsF$_6^-$ doped polyacetylene at higher concentration than 7% and assumed it to be the Knight shift [336]. However, Clarke and Scott [332] pointed out that such a large shift originated from the chemical shift rather than the Knight shift. More recently Terao *et al.* [333] concluded that the Knight shift of ^{13}C NMR was less than 3 ppm which is estimated from the observed de-

shielding shift of 12 ppm in 7.6%-AsF$_6^-$ doped PA and a shielding shift of 14 ppm in 9%-K$^+$ doped PA by subtracting the chemical shift evaluated from the relation of 160 ppm/electron. Such an observation is in agreement with the expectation of (6.23) with $H_{hp}^\pi = 7.8$ G [334] and $\chi_p = 1 \times 10^{-6}$ emu/mole-carbon. In PPP doped with 17% of AsF$_6^-$, a similar experiment was reported with the conclusion that a sizable Knight shift was not observed [259]. Here, it should be noted that the concentration of 17% per ring, that is, about 3% per carbon is too low compared with about 10% in the case of PA. Very recently Bonagamba *et al.* reported that ^{13}C NMR spectra changed as a function of doping concentration in PPP-FeCl$_3$ nominally up to one monomer to 1.5 dopants [337]. In ^{13}C spectra, only one of two peaks, named the C2 site, corresponding to a carbon site bonded with a proton, markedly broadened by three times as much as the undoped, which was ascribed to the chemical shift distribution.

Another effort to shed light on the above problem was made by Sariciftci *et al.* [338,339] using an experiment of the Overhauser shift, accompanied by the Overhauser effect [8,340]. The Overhauser effect is a method of enhancing the nuclear polarization by saturating the electron spin resonance where the electron spins couple with the nuclei, through hyperfine couplings modulated strongly by the dynamics of the electron spins (see also section 4.1). In the coupled spin systems, a poarization of the electron spins gives rise to a shift in the resonance field and/or line broadening in NMR as in the case of the Knight shift, and simultaneously the nuclear spin polarization causes a resonance shift in ESR as in the case of the Overhauser shift, irrespective of the presence of such an enhancement. They observed a resonance shift ΔB_0 of the ESR spectra, by saturating NMR spectra, up to 11 mG which had arisen from the enhanced nuclear polarization at 1.9 K in a heavily doped Polythiophene. Then they deduced the nuclear enhancement facter of 55 and the average hyperfine coupling constant of about -2.0 G [338,339]. From these observations they concluded that the electronic state of heavily doped PT at 1.9 K was metallic [338,339]. However, one ambiguous point still remains before concluding that it is metallic.

Note that the observation of the Overhauser enhancement does not necessarily lead us to the presence of the conduction electrons. As mentioned in section 4.1, the Overhauser effect is known to be observed widely in coupled spin systems, even in the semiconducting pristine *trans*-polyacetylene, with only the

requirement of a rapid electron spin dynamics and shorter correlation time τ_c than the inverse electron Larmor frequency $1/\omega_e$, in which the Overhauser shift could be expected [8]. An extremely sharp ESR linewidth observed in the heavily doped PT [338,339] would fulfill such a requirement of spin dynamics. The minimum requirements for observation of such a shift are the presence of (1) the hyperfine coupling and (2) the polarization of the proton spins.

The above discussion, of course, does not directly negate the possibility of PT being metallic at 1.9 K. Observations of metallic behaviour including the Pauli-like susceptibility, [225,258,279,296] have been reported in similar systems at least at sufficiently higher temperatures than 1.9 K, as mentioned in section 5.3. However, some indications of phase change from metal to insulating state below 10 K are also reported [289,295,301,341].

6   SPIN DYNAMICS IN CONDUCTING STATE

One of the useful applications of magnetic resonance is a spin dynamics study utilizing the magnetic relaxation phenomena, spin-lattice and spin-spin relaxation rates as already demonstrated in section 4 for the neutral soliton dynamics of *trans*-polyacetylene. In this section some applications of such a technique using both the ESR linewidth, i.e., T_2^{-1}, and NMR T_1^{-1} as a function of frequency will be demonstrated for the conducting state of conjugated polymers. Using the same principles as described in sections 4.2 and 4.3, the functional forms of T_1^{-1} in (6.14) and T_2^{-1} in (6.20) and (6.21) provide parameters $D_\parallel$ and $D_\perp$ which characterize the microscopic hopping rates along the chain and between the chains, respectively [6,8,81,82]. Such parameters are useful for interpreting the electronic states in the conducting polymers, since there are still some barriers to obtaining the intrinsic charge transport properties using the conventional electrical conductivity experiments, caused by interfacial semiconducting transport between well crystallized, metallic areas.

6.1   ESR

There are complementary techniques to study spin dynamics, ESR and NMR. Both techniques have their advantages and shortcomings [6]. It is important to apply a suitable method for each case. In this section,

two examples are reviewed as being successful methods with the ESR technique.

6.1.1   Polyaniline

Polyaniline is an interesting system: stable in air [342]; controllable in its morphology [261,304,310]; giving high electrical conductivity σ [304,324,325,343,344] and with its metallic temperature dependence [304]. PANI is chemically synthesized in powder ES-I form [342] as a conducting salt form, with electrical conductivity around 10 S/cm. Such a powder form can be transformed to a free-standing EB-II film by casting from an NMP solution of de-protonated EB-I and to a highly oriented and conducting ES-II form by stretch-orientation. Following protonation results in a dc conductivity of more than 100 S/cm, but the same temperature dependence of σ as ES-I [323,325]. Further
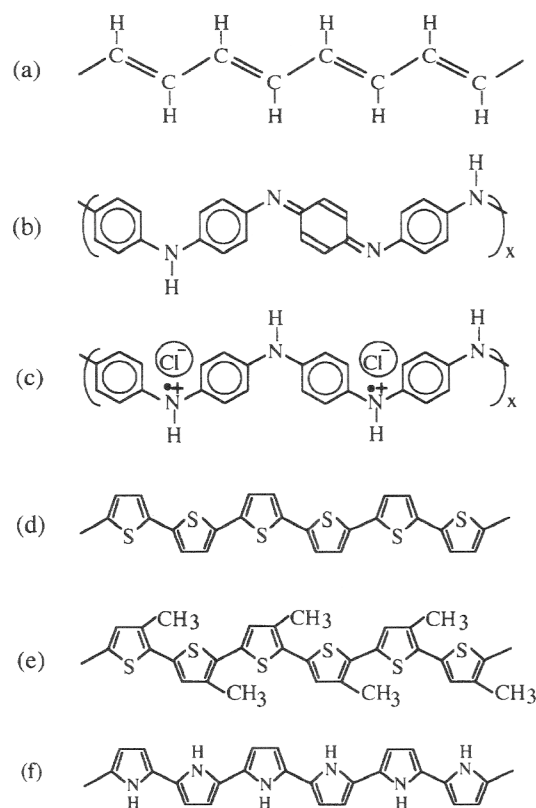

Figure 6.47. The chemical structures for: (a) polyacetylene; and polyaniline in: (b) the insulating emeraldine base (EB) form; (c) the conducting emeraldine salt (ES) form; (d) polythiophene; (e) poly(3-methylthiophene) and (f) polypyrrole.

progress has been reached using CSA as a dopant and *m*-cresol as a solvent, which realized a metallic temperature dependence above 200 K and high conductivity down to 4 K [304]. These findings suggest that the conductivity of the stretch-oriented NMP-cast film is still dominated by the probable amorphous region that gives hopping conduction characterized by $\exp\{-1/T^{1/2}\}$ dependence even at 300 K, but that in PANI-CSA the hopping conduction is successfully suppressed at least down to 200 K by virtue of the well extended morphology of cast film from *m*-cresol [310,311].

In this section a micrscopic charge transport study using the spin dynamics technique is reviewed for a PANI-HCl powder sample (ES-I) [263,305,306, 345,346]. As the first step, the frequency dependence of the proton NMR has been measured [263,264,345, 347]. In proton NMR T_{1H}^{-1}, two different spectral densities $\phi(\omega_n)$ and $\phi(\omega_e)$ appear in the relaxation formula of (6.14) [6,345], and one mainly observes one of them in usual experimental conditions. However, in the NMR case, it is hard to distinguish which of them is being observed. Fortunately, in the case of the ESR formula, (6.20) includes only $\phi(\omega_e)$. Mizoguchi *et al.* reported the ESR linewidth as a function of the inverse-square frequency for the different protonation levels in Figure 6.48 [6]. Analyzing these data with (6.20) and (6.21) they obtained the diffusion rate along the chain $D_\parallel$ and the cut-off frequency τ_c^{-1} as shown in Figure 6.49, together with the dc conductivity measured for the same batch of samples [6,263,345, 347]. Above $y \approx 0.2$, $1/\tau_c$ can be understood to be dominated by the interchain diffusion rate $D_\perp$, but below $y \approx 0.2$ another mechanism something like the exchange interaction [202] dominates $1/\tau_c$. Here, the structure of ES-I by Pouget *et al.* [348] was used. $D_\parallel$ obtained by both ESR and NMR shows some discrepancy in magnitude. A possible origin of such a discrepancy is due to an underestimation of the hyperfine coupling constant for NMR. They found some characteristic features:

(1) $D_\parallel$ shows no definite dependence on y, that is, all the spins produced by protonation have an approximately constant diffusion rate $D_\parallel$ independent of the protonation level y,
(2) $D_\perp$ shows a steep change around $y = 0.2$–0.3 and
(3) the microscopic conductivity σ_{τ_c} shows a behaviour quite similar to the dc conductivity.

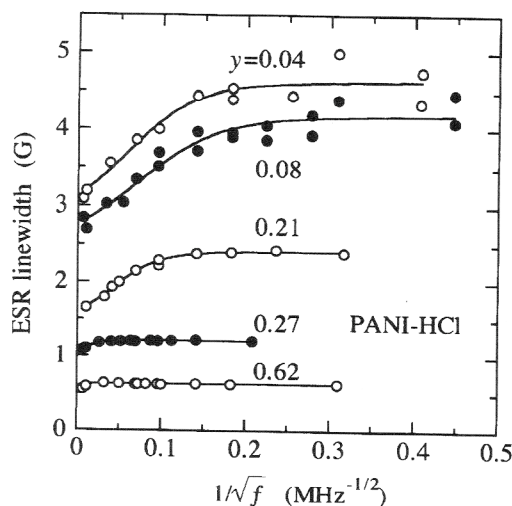They concluded from (1) that the chains carrying the observed spins are fully protonated irrespective of y,

Figure 6.48. The frequency dependence of the ESR linewidth with implicit parameter of the protonation level y [6,346]. Solid curves indicate the sum of the behaviour expected from equation (6.20) for Q-1-D diffusion and a constant as a fitting parameter. The slope of linear increase is proportional to $1/\sqrt{D_\parallel}$, the frequency where the linewidth levels off, corresponds to $D_\perp$. Reproduced from [6] by kind permission of Japanese Journal of Applied Physics.
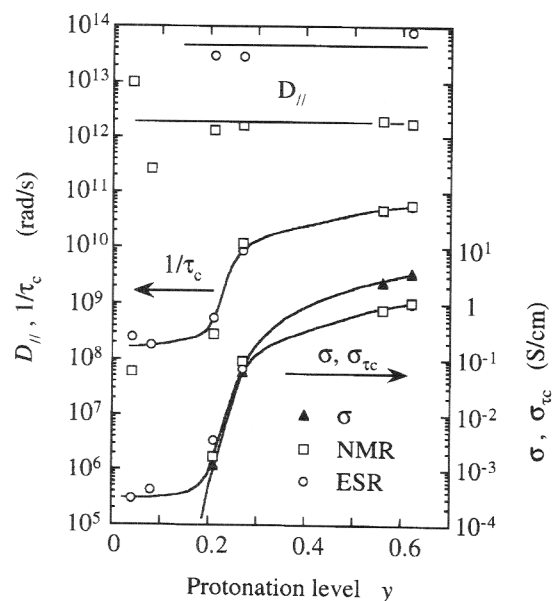

Figure 6.49. The protonation level dependence of the diffusion rates $D_{//}$ along and $D_\perp$ across the chains, together with the dc electrical conductivity σ and the microscopic conductivity $\sigma_{\tau c}$ for PANI-HCl [263,345]. Note the small dependence of $D_{//}$ on y and the similarity of $\sigma_{\tau c}$ to σ. (after [263])

suggesting segregative protonation and from (2), that the spins in the fully protonated chains more easily hop to the neighbouring chains at the higher protonation levels than at $y = 0.2$–0.3, where such protonated chains are connected to each other, that is, the percolation transition was observed microscopically [263,305,345].

Another interpretation was proposed: that the steep change of $D_\perp$ around $y = 0.2$–0.3 resulted from a change in the lattice constant observed by X-ray analysis [348,349]. However, most of the change in the lattice constant is accomplished below $y \approx 0.2$, thus there actually is no change between $y = 0.2$ and 0.3 [348].

They also concluded from (3) that the dc conductivity is limited by the interchain hopping rate $D_\perp$. Such an interpretation is in agreement with the temperature dependence as demonstrated in Figure 6.50 [6,305,306,346]. The dc conduction limited by $D_\perp$ suggests a presence of heavy local disorder, like tangled wires. In such a case, stretch alignment may strongly enhance the dc conductivity, but unfortunately, as was found experimentally [324,325], the temperature dependence remains unchanged and still limited by $D_\perp$ conduction.
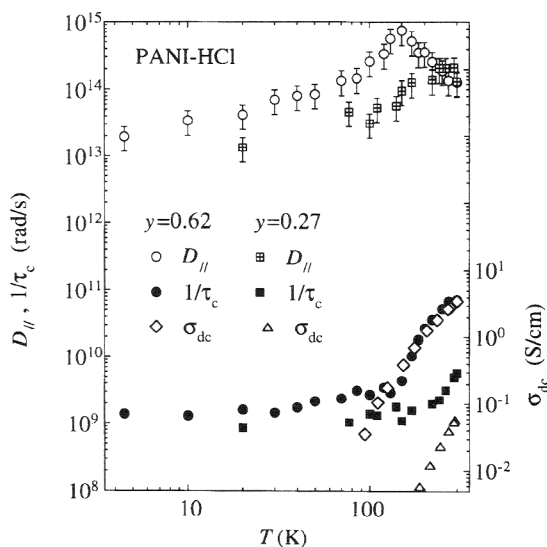

Figure 6.50. The temperature dependence of the diffusion rates $D_\parallel$ along and $D_\perp$ across the chains for PANI-HCl with protonation levels $y = 0.62$ and 0.27. Note that $D_\parallel$ shows metallic temperature dependence above 150 K for $y = 0.62$, and that $D_\perp$ is semiconducting with a temperature dependence similar to that of σ [6,305,306,346] Reproduced from Synth. Met. **69** (1995) 241–2.

Mizoguchi *et al.* reported the temperature dependence of $D_\parallel$, $D_\perp$ ($= 1/\tau_c$ for a larger case than 10^9 rad/s) and σ_{dc} for $y = 0.62$ and 0.27 as shown in Figure 6.50 [6,305,306,346]. The characteristic features are as follows.

(1) The metallic temperature dependence of $D_\parallel$, proportional to T^{-d} with $d = 2$–3 above 150 K for $y = 0.62$, but semiconducting for $D_\perp$ for both $y = 0.62$ and 0.27.

(2) The anisotropy ratio $D_\parallel/D_\perp$ is larger than 10^5, around 150–200 K for both samples.

(3) There is an abrupt change in $D_\parallel$ around 150 K for $y = 0.62$ and may be around 300 K for $y = 0.27$.

(4) The proportionality of $D_\perp$ to dc conductivity σ_{dc} keeps down to 120 K and 200 K for $y = 0.62$ and 0.27, respectively.

They discussed from (1), (2) and (3) that PANI-HCl powder is a Q-1-D metal above 150 K for $y = 0.62$. Such a conclusion of the Q-1-D metal can be compared with the conclusion that the stretch-aligned PANI-ES-II film is a 3D metal, deduced from the thermoelectric power S and the dielectric constant ε [324,325]. From (3) they suggested a phase change from semiconductor to metal at 150 K that is close to the minimum temperature of the thermoelectric power S for the ES-I powder [324,325]. From the fact that this minimum shifts to lower temperature with increasing crystallinity [324,325], they argued that this phase change could be related to the crystallinity of the sample. From the observation in Figure 6.50 that such a transition temperature seems to go up as y decreases from 0.62 to 0.27, they implied that increasing y resulting in the increase of the 3-D interaction, stabilizes the metallic phase.

They estimated several physical parameters as follows.

(1) The microscopic conductivity along the chain $\sigma_{D_\parallel}$ can be estimated as 1.5×10^3 S/cm at 300 K from the relation $\sigma_{D_\parallel} = e^2 N(E_F) D_\parallel c_\parallel^2$, which is comparable with the recent estimation of σ for PANI-CSA film [304].

(2) The mean free path l^* can also be estimated as $0.5 c_\parallel$ at 300 K and $5 c_\parallel$ at 150 K [305,306]. These values suggest that PANI-HCl is in the boundary between metals and electron localization.

(3) The anisotropy ratio could yield the lower bound of the conjugation length of the polymer chain [6] as $l_{min} = \sqrt{D_\parallel/D_\perp} c_\parallel = \sqrt{3 \times 10^4} c_\parallel \approx 180 c_\parallel$ which appears reasonable considering the average molecular weight of about 50 000 for PANI [350].

Finally they discussed a relationship of the large anisotropy and the observed Lorentzian ESR lineshape from the microscopic standpoint that the high degree of anisotropy $D_{\parallel}/D_{\perp} = 10^5$ in PANI-HCl does not contradict the observed Lorentzian lineshape in ESR [263,325] and that the determining factor of the lineshape is not the degree of anisotropy, but the condition $D_{\perp}(D_{\parallel}/D_{\perp})^{1/4} \gg \sqrt{<\omega^2>} = 9.4 \times 10^8$ rad/s, where $<\omega^2>$ is the second moment of the dipolar interaction between the electron spins [76,172]. In the present case, $D_{\perp}(D_{\parallel}/D_{\perp})^{1/4} \geq 10^{10}$ rad/s is large enough to satisfy the above condition at all temperatures. Therefore, the Lorentzian lineshape is a reasonable observation in PANI-HCl, and is consistent with the high anisotropy ratio.

6.1.2 Polythiophene

The spin dynamics of ESR was studied in polythiophene doped with ClO_4^- prepared by electrochemical polymerization at 300 K [296]. Heavily doped PT is known to show a metallic temperature dependence on ESR linewidth caused by the Elliott mechanism, characteristic of metals, as will be mentioned in section 7 [254,258,287,295,296]. In addition to this, a line broadening due to the spin dynamics is expected. Mizoguchi et al. reported the frequency dependence of the ESR linewidth in PT-ClO_4^- as shown in Figure 6.51 [296]. The filled circles do not behave simply following the prediction of (6.20) and (6.21) of Q-1-D spin motion, but there is a broadening mechanism other than
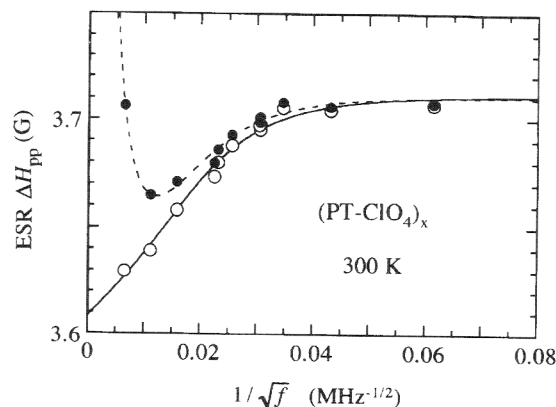

Figure 6.51. The frequency dependence of ESR linewidth for PT-ClO_4^- at 300 K [6,296]. ● indicate the raw data and ○ are linewidths corrected by the g-anisotropy broadening which is proportional to the external magnetic field strength. Reproduced from ref. 296 by kind permission of Japan Physics Society

Q-1-D. They concluded that such a mechanism, that broadens the linewidth proportionally to the magnetic field, can be assigned to powder pattern broadening of g-shift anisotropy [296]. Analyzing the data following such an idea, the data subtracting the broadening due to the g-shift, shown by the open circles in Figure 6.51, appears to be typical behaviour of Q-1-D spin motion, demonstrated by the solid curve, which shows the Elliott (frequency independent) + Q-1-D broadenings. They concluded PT-ClO_4^- to be a good Q-1-D metal [296].

From such an analysis they estimated $D_{\parallel} = 1.9 \times 10^{15}$ rad/s and $D_{\perp} = 5.5 \times 10^9$ rad/s with $a = 3.65$ Å, $b = 12.5$ Å and $c = 3.9$ Å, and with $N(E_F) = 0.12$ states/(eV C) for both spin directions from the Pauli susceptibility χ_p [210] which gives an estimate of the microscopic conductivity as $\sigma_{D_{\parallel}} = 1.2 \times 10^3$ S/cm and $\sigma_{D_{\perp}} = 3.7 \times 10^{-2}$ S/cm at 300 K. They considered these values to be compatible with the observed $\sigma_{dc} = 150$ S/cm, since $\sigma_{D_{\perp}} = 3.7 \times 10^{-2}$ S/cm forms a three-dimensional network with $\sigma_{D_{\parallel}} = 1.2 \times 10^3$ S/cm. Here, note that the absolute value of $\sigma_{D//}$ should be regarded with caution, since $\sigma_{D_{\parallel}}$ depends largely on $N(E_F)^3$ and Σ_i^2.

6.2 NMR

The frequency dependence of NMR spin-lattice relaxation is also a powerful tool in the study of spin dynamics in the conducting polymers, to reveal the microscopic dynamics of the charge carrier, polaron and/or conduction electron spins. However, one has to pay attention to one important point; the localized paramagnetic spins and molecular motion which substantially contribute to the NMR T_{1H}^{-1}. Since the relaxation caused by the spins diffusing is suppressed by a factor of $D_{\parallel}^{-1/2}$, the contribution due to the localized spins and the molecular motions could become dominant [6]. Therefore, interpretation of the NMR relaxation rate is generally useful but difficult.

6.2.1 Polyacetylene

The first study of spin dynamics in a conducting polymer, polyacetylene doped with AsF_6^-, was reported by Nechtschein et al. in 1980, as shown in Figure 6.52 [143]. With (6.14) assuming $\phi(\omega_n) \approx$ const. ($\omega_n \ll 1/\tau_c$) at the measured frequencies, they deduced the diffusion rate along the chain $D_{\parallel} \approx 1.7 \times 10^{17}$ rad/s that corresponds to the microscopic conductivity $\sigma_{\parallel} \approx 5 \times 10^4$ S/cm with anisotropy
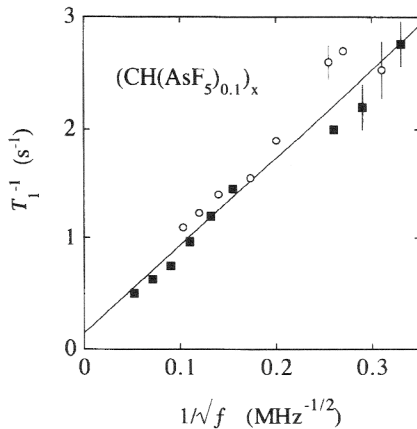
Figure 6.52. NMR T_1^{-1} as a function of inverse square-root frequency for AsF_6^--doped PA [143]. ■ and ○ refer to two different doped $(CH)_x$ samples. The solid line corresponds to (6.14). (after [143])

Figure 6.53. NMR T_1^{-1} as a function of the number of Curie spins measured by both SQUID susceptometer and Schumacher–Slichter methods in the polyacetylene heavily doped with several different species at 20 K and 50.5 MHz [221,353]. The solid line shows the linear dependence. Reproduced from Synth. Met. **69** (1995) 43–4.

ratio $\sigma_\parallel/\sigma_\perp \geqslant 4 \times 10^5$ [143]. This value is interesting if one compares it with the recently achieved dc conductivity $\sigma \geqslant 10^5$ S/cm in T-PA doped with I_3^- [211]. It is noteworthy that 5% of the spins that were present in the undoped $(CH)_x$ could explain the observed relaxation rate, as pointed out by them [143].

In 1983, Kume *et al.* found the Korringa-like relation $T_{1H}T = $ const. in Br_3-doped PA, characteristic of metallic systems [351]. They also found the same relation for AsF_6^--doped PA with an extra peak below 100 K, probably due to molecular motion of dopant ions. In both systems the Pauli-like susceptibility was observed. From analysis of the relaxation data they derived σ_{NMR} as 4×10^3 S/cm for Br_3^--PA and 1×10^4 S/cm for AsF_6^--PA, which are compared with $\sigma_{dc} = 10$ and 600 S/cm, respectively [351]. These estimations should be viewed with caution, since the same ambiguity as the first example of [143] is included.

Recently, several spin dynamics studies on doped PA were reported for the dopants of FSO_3^- [6,221,352, 353], K^+ [6,221,353–355], I_3^- [6,221,353], ClO_4^- [6,221,353] and Br_3^- [6,221,353,354]. Shimizu *et al.* [6,221,353] demonstrated that NMR T_{1H}^{-1} and the number of Curie spins N_c show a strong correlation at 20 K, but not above 200 K as shown in Figures 6.53 and 6.54. They explained this behaviour and the temperature dependence of T_{1H}^{-1} by the fact that the spin-lattice relaxation rate due to the Curie spins shows a steep increase below 70 K and gradually decreases above the broad peak, which is a characteristic behaviour also in other polymer systems, PT [356],
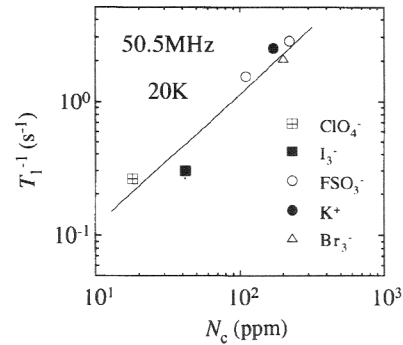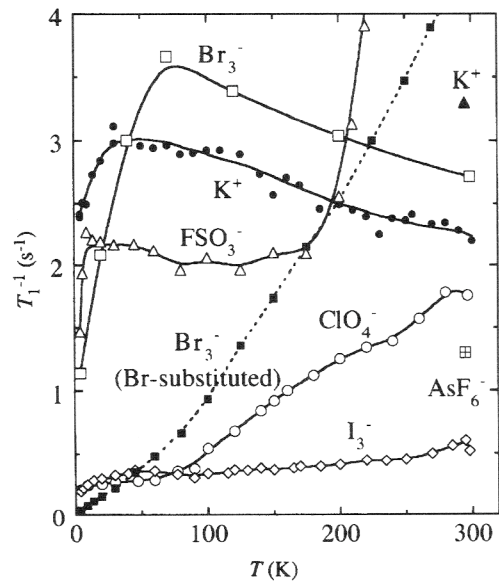

Figure 6.54. The typical temperature dependence of NMR T_1^{-1} measured at 50.5 MHz in: K^+ (S-PA 13%, ● [221,353,354]; and NT-PA 14% ▲ [355]); Br_3^- (S-PA 14.7%, □ and aged six months, ■ [221,353]); AsF_6^- (S-PA 10%, ◨ [143]), I_3^- (NT-PA 7.6%, ◇ [221,353]); ClO_4^- (○ [221,353]); and FSO_3^- (NT-PA 15%, △ [352]) - doped $(CH)_x$. The steep increase around 200 K in FSO_3^- is due to molecular motion The curves are a guide for the eye. Reproduced from Synth. Met. **69** (1995) 43–4.

PPy [286] and PANI [345,357,358] and that the increase above 100 K could be caused by the relaxation due to the charged carriers, which is what they want to extract, and/or the molecular motion which is specific

Figure 6.55. The temperature dependence of NMR T_1^{-1} in six-months-aged $[CH(Br_3^-)_y]$, with $y = 0.147$ [6,221]. It is noted that the temperature dependence is steeper than $T_1T =$ const. Reproduced by kind permission of the Japanese Journal of Applied Physics.

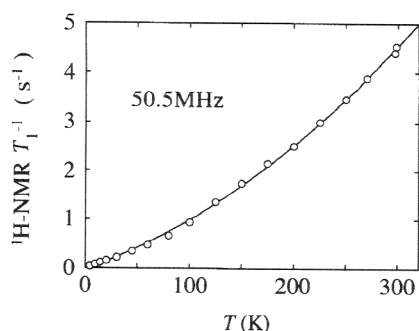**Figure 6.56.** The temperature dependence of the microscopic resistivity of ρ in six-months-aged $(CH(Br_3^-)_y)$, with $y = 0.147$ [221,353]. The solid curve is the prediction for the 1D metal described by (6.24) with $\hbar\omega_0/K_B = 160$ K. Reproduced by kind permission of the Japanese Journal of Applied Physics.

for FSO_3^- doped PA among the polymers in Figure 6.54. Then they estimated the minimum microscopic conductivity as $\sigma_\parallel \geqslant 2 \times 10^5$ S/cm for the I_3^- case and $\sigma_\parallel \geqslant 2 \times 10^4$ S/cm for the ClO_4^- case, in agreement with $\sigma_{dc} \geqslant 2 \times 10^5$ S/cm for the I_3^- doped T-PA [66,67].

They found that the six-months-aged Br_3^- doped S-PA shows a typical temperature dependence of the metallic carriers with the Pauli susceptibility as appears in Figure 6.42, that is, the relation $T_1T\sqrt{D_\parallel} = T_1T^{3/2}$ = constant, derived from (6.14) for the case of $\sigma \propto D_\parallel \propto 1/T$, as shown in Figure 6.55 [6,221,353]. Then they deduced the metallic temperature dependence of the microscopic resistivity $\rho_\parallel$, proportional to T at higher temperatures than 50 K, as demonstrated in Figure 6.56. They confirmed that the bromine atom is partially substituted for the protons, which is the effect of aging for six months. It is known that such substituted polyacetylenes (by Br for H) could also be doped with bromine to the metallic state [359]. Several possible reasons why the metallic relaxation was observed successfully in this system were suggested: (1) that the random potential produced by the Br substitution enhances the relaxation rate due to potential scattering; (2) that the phonon scattering of the electrons was also enhanced by an increase in the number of phonons of which the energy was lowered by the seventy-times-heavier mass of the Br atom than the proton; and (3) the relaxation centres of the slowly diffusing Curie spins (probably residual neutral solitons) were deactivated because of a confinement due to the random potential. (1) and (2) would actually raise the deduced resistivity up to 4×10^{-4} Ωcm at

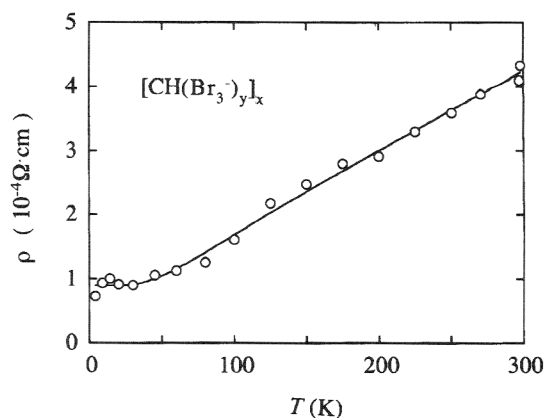300 K. The solid curve in Figure 6.56 shows a prediction for the 1-D metal [6,221,353,360]

$$\rho_{ph} = \frac{\pi^2\hbar\Sigma}{e^2}\frac{\alpha^2 D(E_F)}{M\omega_0 v_F}$$
$$\times \frac{1}{\cosh(\hbar\omega_0/2k_BT)\sinh(\hbar\omega_0/2k_BT)} + \rho_0, \quad (6.24)$$

where Σ is the cross-sectional area for a single chain, α the electron–phonon coupling constant, ω_0 the phonon frequency with $q = 2k_F$ causing carrier scattering in the 1-D electronic systems, ρ_0 the residual resistivity and the other symbols have their usual meanings. However, note the assumption that the Pauli susceptibility is independent of temperature, is not necessarily valid in the systems with strong electron–electron correlation as found in many charge–transfer salts [207].

6.2.2 Other polymers

In PPY-ClO_4^-, Devreux and Lecavelier studied ^{1}H NMR T_{1H}^{-1} as a function of frequency from 50 K to 300 K and analyzed it with the spectral density for a random walk on the fractal network, concluding that the dimensionality of the random walk was 1-D below 150 K and increased to 1.2 at 200 K, 1.5 at 250 K and reached 2-D at 300 K [361].

A similar result was reported on the electronic spin (polaron) created by the muon in the undoped-PPy and

undoped-PANI by Pratt *et al.*, [362]. The injected muon is understood to form a diamagnetic state in the polymers, creating a paramagnetic state, a polaron on the polymer backbone as found in PA [363]. They found that at 300 K the dimensionality was two in both PPy and PANI which is in agreement with [361] and one in PANI at 15 K, but in PPy the polaron seems to localize at 15 K.

Such an analysis was also attempted in PANI-HCl by ^{1}H NMR T_{1H}^{-1} and it was demonstrated that both Q-1-D and the fractal network analyses could reproduce T_{1H}^{-1} [263,345]. Finally, it was concluded that Q-1-D holds in this system, from the analysis of both NMR and ESR.

The hydration effect on PANI-HCl was investigated by NMR [364–367]. Using ^{1}H NMR, Nechtschein *et al.* [364], Travers *et al.* [367] and Alix *et al.* [366] found that protons fixed to the polymer backbone frequently (in order of 10^3 s^{-1}) exchanged for the mobile protons in the absorbed water. Further, the fixed water molecules are present even in the well-dried samples and become mobile upon hydration. Recently, Travers reported that the hydration enhances the on-chain diffusion rate of the polaron, using T_{1H}^{-1} and $T_{1\rho H}^{-1}$ [367].

Travers *et al.* studied the spin dynamics by ^{1}H NMR T_{1H}^{-1} as a function of frequency in an unstretched and four-fold-stretched PANI films protonated by HCl [359,369]. The result showed a good 1-D behaviour and a clear increase of the cut-off frequency of the stretched film, compared with the unstretched one, which implies that the increased interchain interaction was due to the increased crystallinity by stretching [370]. Then they concluded that an anisotropy ratio, $\sigma_\parallel / \sigma_\perp$ in the macroscopic (dc) conductivity is smaller than that in the microscopic one by the spin dynamics, because the geometrical factors of the conducting islands dominate that of the dc conductivity.

Kazama *et al.* reported that ^{1}H NMR T_{1H}^{-1} as a function of frequency in poly(paraphenylene sulphide) (PPS) doped heavily with SO_3^-, showed the inverse square law of frequency [371]. The diffusion coefficient estimated using (6.14) from such a frequency dependence was much smaller than that of the neutral soliton in *trans*-PA.

Very recently Kolbert *et al.* [372] observed a Korringa-like temperature dependence of ^{13}C NMR T_{1C}^{-1} in the same batch of the PANI-CSA sample for the magnetic measurement [209], which is a strong indication of the presence of conduction electrons, in agreement with many other conclusions obtained by various experiments: dc conductivity [304]; Puali-like susceptibility [209]; optical absorption [283]; negative dielectric constant [373,374]; and microscopic conductivity [305,306], characteristic of the metals.

In poly(3-alkylthiophene Mabboux *et al.* reported a comparative study of the spin dynamics by ^{1}H NMR T_{1H}^{-1} and found a remarkable difference of the on-chain diffusion rate up to two orders of magnitude higher in both polyhexylthiophene and a diblock polystyrene–polythiophene co-polymer doped with BF_4^- than in both polybithiophene and polydimethyltetrathiophene doped with BF_4^- [375]. They ascribed such observations to degrees of structural order.

7 ESR LINEWIDTH/ELLIOTT MECHANISM IN CONDUCTING STATE

In this section the Dysonian lineshape, arising from a skin depth shorther than the sample size, will not be mentioned. See [2] for this subject related to conducting polymers.

Since the charge carriers with spin, polarons and/or conduction electrons, move rapidly in the conducting polymers, the ESR linewidth is generally narrower than in the case of localized spins in which the linewidth is predominated by the unresolved hyperfine splitting due to nearby nuclei carrying a spin, proton, fluorine, carbon 13, etc. For example, in polyacetylene (PA) the linewidth is order of 10 G in *cis*-PA [53,109] where the neutral soliton is confined within short *trans*-segment, but is less than 1 G in *trans*-PA [147] where it can diffuse freely. In the case of the rapid motion of spins, the linewidth is governed by the relaxation rate and the life-time broadening, caused by motional modulation of local fields [8,11]. In such systems another characteristic relaxation, called the Elliott mechanism [288,376], is known to be effective, especially in systems containing heavy atoms with large atomic number, z, expressed by the relationship:

$$T_{1E}^{-1} = \alpha \Delta g^2 / \tau_r = \alpha (\lambda / \Delta E)^2 / \tau_r \propto \rho_{dc}, \qquad (6.25)$$

where T_{1E}^{-1} is the ESR spin-lattice relaxation rate proportional to the ESR broadening, Δg the ESR g-shift, λ the spin-orbit coupling constant, ΔE the energy splitting between the valence band and the spin-orbit state, $1/\tau_r \propto \rho_{dc}$ the relaxation rate of the electron momentum and α the constant determined experimentally, which is of the order of ≈ 0.1 for the alkali metals [377]. One meaning of (6.25) is that the spin-flipping transition (T_2^{-1}) is induced through the spin–orbit

coupling when the conduction electron is scattered by a phonon and/or impurities. Then, it is expected for the ESR linewidth to behave correspondingly to the electrical resistivity. Experimentally, the presence of not only such a correspondence [378–380] but also a simple normalization factor ($\alpha \approx 0.1$ in (6.25)) [377,381] was confirmed in simple metals such as alkali metals, noble metals and s–p metals. However, in purely one-dimensional systems, the Elliott mechanism is known to be prohibited because of symmetry restrictions [288,376]. In some cases such a restriction is not applicable, for example, due to electronic conduction in dimensions higher than unity as in alkali-doped polyacetylene and due to lower molecular symmetry, as in heterocyclic polymers.

Several studies on the ESR linewidth as a function of temperature in conducting polymers have been reported and temperature dependences of the ESR linewidth are roughly classified to three regimes as schematically shown in Figure 6.57: (1) motional narrowing regime; (2) intermediate regime; and (3) metallic regime. The electronic state in regime (1) is fundamentally localized at low temperatures and the motion of the electrons is thermally activated. In regime (3), the electronic state is a metal and the main relaxation mechanism is the Elliott one. The second regime is described as a cross-over of the two behaviours. These regimes are observed in the course of doping [258]: (1) corresponds to light doping; (2) intermediate doping; and (3) heavy doping.

The case of regime (3) was found in most of the heavily doped conjugated polymers; PA [382–384]; PPP [316,317,320,321],PT [6,287,296,338,339], P3MeT [258,287,295,296,301] and PPy [282,286,

287]. Some of the other heavily doped systems are still in regime (2) [238,255]

7.1   Alkali doped polyacetylenes

As shown in Figure 6.58, Rachdi *et al.* and Bernier *et al.* reported that the ESR linewidth in the alkali-doped PA prepared by chemical doping with alkali-metal-naphthalene complexes in tetrahydrofuran (THF) gave results in the metallic regime (3) [382,384]. Billaud *et al.* obtained a very similar result between 100 and 300 K for the alkali-doped PA prepared by the vapour phase intercalation technique [383]. Interesting features of this figure are small but clear upturns below 20 K for K^+ and Rb^+, and below 100 K for Li^+ [382,384] and a rapid increase in the linewidth as the atomic number increases [382–384]. Such an increase can be found in other alkali-metal intercalated PPP [316], graphite (GIC) [385] and fullerene [386,387], characterizing the ESR linewidth by the Elliott mechanism [288,376]. This observation suggests the spin–orbit mixing of the carrier band with the dopant alkali–metal band. Since the Elliott broadening found in the alkali-PPP [316] is much smaller than these alkali-PA, a stronger mixing in PA is suggested. In the present case, the restriction applicable to purely one-dimensional systems does not interfere with the case of alkali-PA, since the contribution of the dopant band makes the electronic state more three-dimensional.
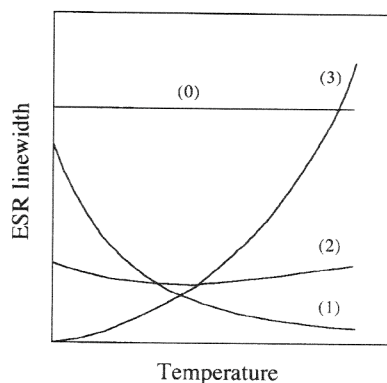

Figure 6.57. A schematic temperature dependence of the ESR linewidth in the three different regimes: (0) localized spins; (1) motionally narrowing regime; (2) intermediate regime; and (3) metallic regime.
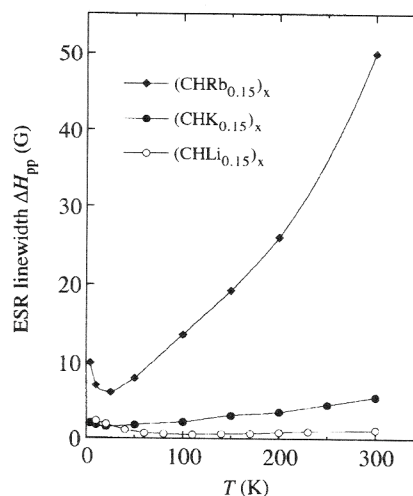

Figure 6.58. The ESR linewidth as a function of temperature for $(CHLi_{0.16})$, $(CHK_{0.16})$ and $(CHRb_{0.16})$ [382]. The solid curves are a guide for the eye. (after [382])

The ESR linewidth is analyzed as a function of atomic number with a power law, $\Delta H_{pp} \propto z^n$, where $n = 2.3 \pm 0.7$ [382,384] and 2.9 ± 0.5 [383]. More directly, one can compare the ESR linewidth with the spin–orbit splitting, λ, as shown in Figure 6.59 [376]. This figure indicates that the linewidth is proportional to λ–$\lambda^{1.5}$ that is weaker than λ^2 in the prediction of (6.25), when assuming that ΔE, α and the phonon scattering (τ_r) are independent of the species of alkali dopants. This finding suggests that ΔE, α and/or the phonon scattering (τ_r) weakly depend on the atomic number of alkali-dopants. Such a dependence was not observed in the ESR linewidth of the pure-alkali metals and noble metals [377,381]. If the intrinsic resistivity were available, the contribution of τ_r could be specified and if anisotropy of the g-shift were measured, the contribution of ($\lambda/\Delta E$) could be obtained.

The small upturn at low temperatures implies the localization of the spins observed by ESR. On this point, two possibilities could be mentioned; one is a change of the electronic state that is metallic at high temperatures, into a semiconducting phase, and the other is an interchange of the Pauli spins at high temperatures with the Curie spins which are a different spin species that predominate the ESR signal at low temperatures, even in minority spins. In the latter case, two spin species could be observed.
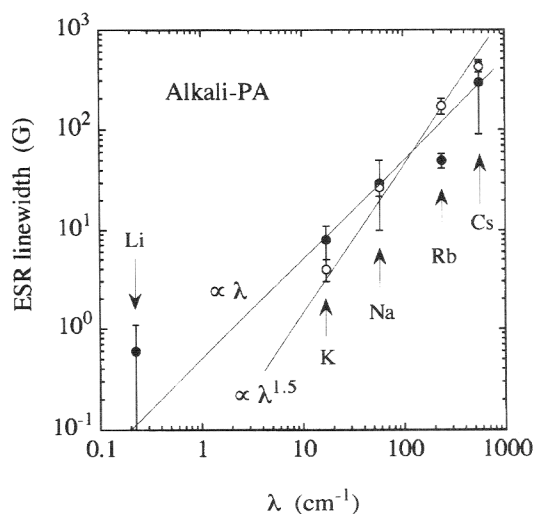
7.2 Heterocyclic polymers

As in the other example, the ESR linewidths reported by Mizoguchi et al. are shown as a function of temperature in commonly ClO_4^--doped PT and PMeT in Figure 6.60, and PPy in Figure 6.61 [287,301]. In PT and PMeT, both the residual widths at $T = 0$ and the upturn are relatively small compared with those in the alkali-PA's. On the other hand, in PPy, although the linewidth is extremely narrow, $\Delta H pp = 0.1$–0.4 G, as reported in [238,286,328,388], the residual width is remarkably large with the small upturn. It is noteworthy that the linewidth at 300 K rapidly increases
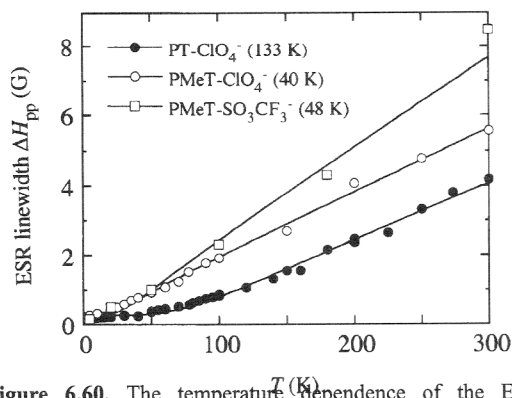
Figure 6.60. The temperature dependence of the ESR linewidth for PT-ClO_4^- and PMeT-ClO_4^- measured at 50 MHz [6,287], and for PMeT-$SO_3CF_3^-$ at the X-band [295]. Note the qualitative difference in the temperature dependencies for these materials. The solid curves show the qualitative predictions of (6.24) with $\hbar\omega_0/k_B$ shown in parentheses [6,296]

Figure 6.59. The ESR linewidth as a function of the spin-orbit splitting, λ (cm^{-1}) (After Yafet; 1965 [376]) of the dopant ion ●, [382,384] and ○ [383]
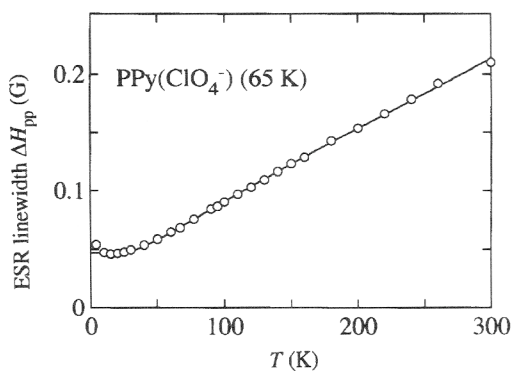

Figure 6.61. The temperature dependence of the ESR linewidth for PPy-ClO_4^- measured at 50 MHz [287]. The solid curve shows the qualitative prediction of (6.24) with $\hbar\omega_0/k_B$ shown in parentheses [6,296] Reprinted from Solid St. Commun. **96** (1995) 333–7.

with increasing atomic number of the heaviest atoms in the polymer backbone, nitrogen and sulphur.

In Figure 6.62, the ESR linewidth is plotted as a function of the spin–orbit coupling, ζ ($\zeta l \cdot s$) that is equal to $\pm \lambda$ ($\lambda L \cdot S$) in the case of $S = 1/2$ [9], for the heaviest atom on the polymer backbone of the available conducting polymers: PPV-HSO$_4^-$ [307]; PPy-BF$_4^-$ [286,328]; PPy-ClO$_4^-$ [238,287]; PPy-PF$_6^-$; PPy-TsO$^-$, PPy-AsF$_6^-$ [282]; PT-ClO$_4^-$, PT-AsF$_6^-$ PT-PF$_6^-$, PMeT-ClO$_4^-$ [287]; PMeT-PF$_6^-$ [389] and PMeT-SO$_3$SF$_3^-$ [295]. Figure 6.62 clearly demonstrates the expected behaviour of (6.25), $\Delta H \propto \zeta^2 = \lambda^2$, provided that ΔE, α and τ_r are independent of polymer systems. This point is a distinct difference from the case of the alkali-PA. The other marked difference from it is an independence of the dopant species that contain a variety of atoms: C ($\lambda = 29$ cm^{-1}); N (76 cm^{-1}); O (151 cm^{-1}); F (272 cm^{-1}); P (299 cm^{-1}); S (382 cm^{-1}); Cl (587 cm^{-1}); As (1500 cm^{-1}). This fact strongly suggests that the charge carriers present very little at the dopant site, in contrast with the alkali dopants in PA [287]. A possible origin of such a contrast would be a difference between acceptor and donor; vacant donor levels may be placed nearer to the conduction band than filled acceptor levels. The symmetry restriction on the Elliott mechanism seems not to appear in the heterocyclic polymers,
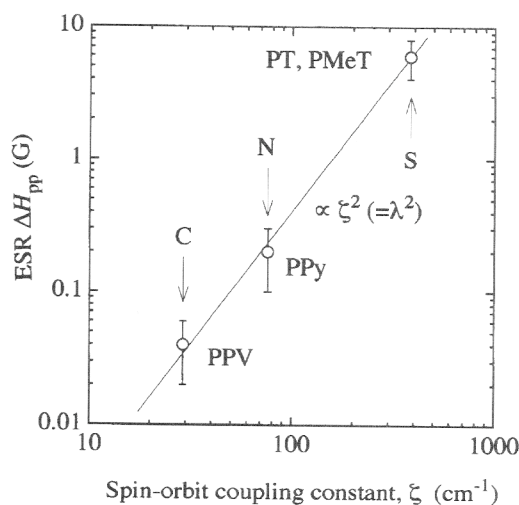
probably due to a low molecular symmetry [390]. A model on the interchain conduction mechanism via dopant proposed by Zuppiroli *et al.* [294] is not applicable to the present case, since such a model expects stronger coupling between the charge carriers and the dopants.

Then, it is interesting, if available, to compare the ESR linewidth with the resistivity in the crystalline region that could be metallic. In some systems the resistivitiy r_{VSC} obtained by the voltage-shorted-compaction (VSC) method (It is better represented by "Mininum Separation of Potential terminals" (MSP), because actually a conducting paste covers the whole area between the potential terminals except in the narrow slit of paste removed by a thin metal plate.), giving the metallic temperature dependence [277,284,289,301, 341], is available with a high reproducibility more than 50% [289] in samples prepared under well controlled conditions, film quality and type of conductive paste and solvent. Such a resistivity is compared with the ESR linewidth for the same batch of samples as the VSC measurements in Figure 6.63 and Figure 6.64 for PT-AsF$_6^-$ and PT-ClO$_4^-$ [287,301], respectively, and Figure 6.65 for PMeT-PF$_6^-$ [341,389]. The ESR linewidth demonstrates a good qualitative agreement with r_{VSC}, indicating validity of both the above interpretations of the ESR linewidth in terms of the Elliott mechanism and the VSC resistivity. The solid curves appearing in Figures 6.60–61 and 6.63–64 describe the fitting curves with the one-dimensional model for the resistivity (6.24), with three fitting parameters, ρ_0, $\hbar\omega_0/k_B$ and β ($= \pi^2 \hbar \Sigma \alpha^2 D(E_F)/e^2 M \omega_0 v_F$) as explained in section

Figure 6.62. The ESR linewidth as a function of the spin–orbit coupling constant, ζ (cm^{-1}) (After Gordy, 1980 [9]) of the heaviest atom in the polymer backbone: PPV-HSO$_4^-$ [307]; PPy-BF$_4^-$ [286,328]; PPy-ClO$_4^-$ [238,287]; PPy-PF$_6^-$, PPy-TsO$^-$, PPy-AsF$_6^-$ [282]; PT-ClO$_4^-$, PT-AsF$_6^-$ [287]; PT-PF$_6^-$, PMeT-ClO$_4^-$, PMeT-PF$_6^-$ [389]; and PMeT-SO$_3$SF$_3^-$ [295]

Figure 6.63. The ESR peak-to-peak linewidth as a function of temperature in PT-ClO$_4^-$, together with the resistivity r_{VSC} normalized at 280 K measured by the voltage-shorted-compaction (VSC) method. Both data can be qualitatively well reproduced by the solid curve, (6.24) Reprinted from Solid St. Commun. **96** (1995) 333–7.
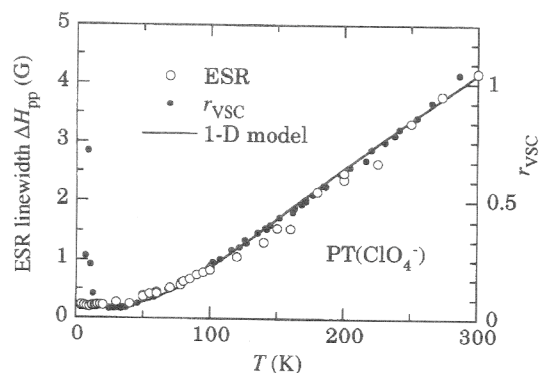
Figure 6.64. The ESR peak-to-peak linewidth as a function of temperature in PT-AsF$_6^-$, together with the resistivity r_{VSC} normalized at 280 K measured by the voltage-shorted-compaction (VSC) method. Both data can be qualitatively well reproduced by the solid curve, (24) Reprinted from Solid St Commun. **96** (1995) 333–77.
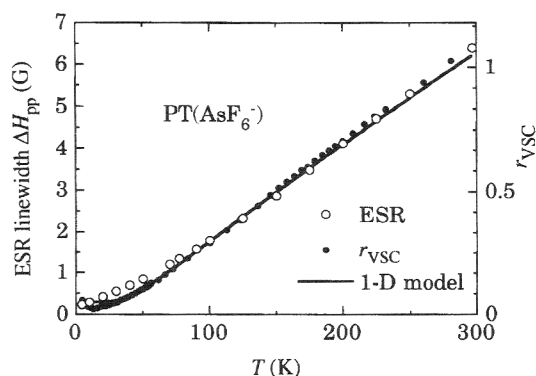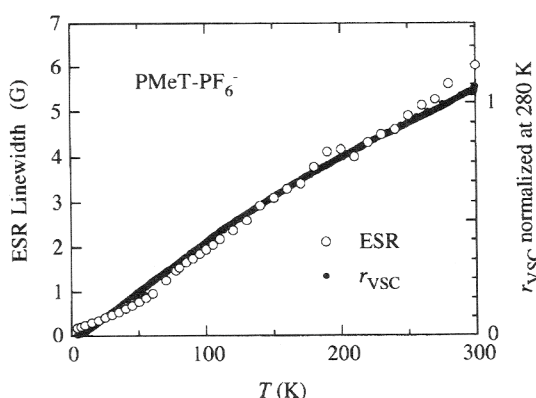

Figure 6.65. The ESR peak-to-peak linewidth as a function of temperature in PMeT-PF$_6^-$, tokether with the resistivity of r_{VSC} normalized at 280 K measured by the voltage-shorted-compaction (VSC) method

6.2.1. The values obtained for $\hbar\omega_0/k_B$ are summarized in Table 6.7 [287]. The functional form of (6.24) can reproduce a variety of the characteristic behaviour as a function of temperature as shown in Figures 6.60–61 and 6.63–6.64.

8 CONCLUDING REMARKS

It has been shown how the magnetic properties are useful for understanding a variety of aspects: lattice structure; structure and dynamics of the elementary excitations; susceptibility and Knight shift; and dynamics of charged carriers with spin in semiconducting and conducting states of conjugated polymers. Especially, at various stages, the usefulness of many kinds of magnetic resonance techniques were demonstrated; both of cw and pulse, broad line and high resolution, of 1-D and 2-D NMR and a combination of ESR and NMR as in ENDOR, TRIPLE resonance and Schumacher–Slichter techniques, as a function of temperature and frequency.

A second-moment study of ^{1}H NMR spectra is a complementary method of X-ray diffraction analysis. A shortcoming of the X-ray diffraction technique is the difficulty in determining the precise position of hydrogens, since the hydrogen contains only one electron to which the X-ray diffraction intensity is proportional. On the contrary, ^{1}H NMR provides the most intense signal and then is suitable for determining the spatial relation between the hydrogens. The second moment analysis of ^{1}H NMR has succeeded in fixing the setting angles uniquely. The oriented sample could give further useful information when analyses of other parameters are combined; i.e. linewidth, spin-lattice and spin–spin relaxation rates of NMR and ESR. The Pake doublet provides an excellent means to determine the atomic distance of a pair. The chemical shift also offers a conventional way of specifying types of bonding, as is well known.

ENDOR is useful in observing spin distributions of paramagnetic excitations of conjugated polymers. Use of stretch-oriented samples is particularly important in confirming the π-electron nature of excitations through anisotropic behaviour as well as in enhancing the spectral resolution. Detailed spin distribution parameters can be obtained with the aid of ENDOR-induced ESR and TRIPLE resonance. ENDOR studies of paramagnetic spins generated by doping or photo-excitation would become interesting subjects. Some-

Table 6.7. $T_\omega = \hbar\omega_0$ for the several conducting polymers with the five-membered ring, doped by ClO_4^- or AsF_6^- [287]. T_ω is a measure of the frequency for the phonon with $q = 2k_F$ in units of temperature. Reprinted from Solid St. Commun. **96** (1995) 333–7.

	PT(ClO_4^-)	PMeT (ClO_4^-)	PPy (ClO_4^-)	PT(AsF_6^-)
T_ω (K)	240	80	130	150

times analysis of the ESR spectra using the spectrum simulation method, yields the spin density distribution.

The topic of neutral soliton dynamics has been controversial for many years. The reasons have been due to a lack of definite data and a lot of different interpretations from a variety of bases for many experimental data. In this review, we tried to explain most of the important experimental results in terms of a diffuse/trap model based on observations of the ESR linewidth as functions of temperature and frequency. Anomalous broadening observed only in $(CH)_x$, but not in $(CD)_x$ at frequencies lower than 6 MHz was explained in a clear-cut way by this model, giving a consistent value of the maximum spin density of the neutral soliton, $\rho \approx 0.15$–0.17 in comparison with 0.17 determined by the ENDOR technique. These successes represented in the finally obtained diffusion rates which are found to be consistent between NMR and ESR seem to settle the controversy.

Susceptibility is one of the basic quantities used to characterize materials. Recently, one could measure it easily using SQUID susceptometers and ESR integrated intensity. However, we need to pay attention to extract the intrinsic properties from experimental data. For example, sometimes a temperature measuring system may give different results because of artificial origins. Even if the result obtained is intrinsic, the appropriate interpretation is also necessary, since, for example, the Pauli-like susceptibility could represent different situations; delocalized conduction electrons in metals and Anderson localized electrons in Fermi glasses. Therefore, it is convincing that the Pauli susceptibility exists, at least in the recent well-characterized heavily-doped films with higher structural order. In several systems, anomalies in susceptibility were reported; the Curie-like behaviour below 200 K and a stepwise increase continuing to the Pauli-like one above 200 K, suggest a phase transition. Paying attention to the quality of samples, such anomalies should be specified.

The metallic state of the conducting polymers has been confirmed by optical measurements and thermoelectric power, but only above 200°C by dc conductivity because of semiconducting transport between the metallic regions. The intrinsic anisotropy of such a metallic conduction that could specify dimensionality of the electronic states, is rather difficult to measure by dc conductivity for the same reason. The spin dynamic techniques might be a powerful tool to characterize microscopic conduction of charge carriers with spin. Such studies were recently reported for several systems with ESR and NMR as a function of frequency. This direction of investigation could yield fruitful results with further refinement of analysis.

Similar information can be also obtained by the ESR linewidth as a function of temperature, dominated by the Elliott mechanism through the spin-orbit coupling. It could possibly yield temperature dependence of the electrical resistivity if it were analyzed together with the g-shift and/or g-shift anisotropy and the spin dynamics data. It is noteworthy that a variety of temperature dependences are uniformly understandable with a single formulation characteristic of one-dimensional electronic systems. This mechanism is observable only in polymers with heavy nuclei, such as alkali and sulphur. It is also worth noting that the dopant nuclei could contribute to the Elliott mechanism in the donor dopant systems. Contrary to this, nuclei in the acceptor dopants could contribute little. Such a difference reflects each electronic state. Further investigation makes clear these points.

The authors hope that this critical review will encourage further development in the investigation of the magnetic properties of conjugated polymers. They hope they have not omitted any important work or caused any misunderstanding but that further discussion will be encouraged as well as the communication of further results. Finally, they hope this review will make a contribution to the understanding of the science and technology of conducting polymers.

9 ACKNOWLEDGEMENTS

10 REFERENCES

1. A.J. Heeger, S. Kivelson, J.R. Schrieffer and W-P Su, *Rev. Mod. Phys.* **60**, 781–850 (1988).
2. P.K. Kahol, G.C. Clark and M. Hehring, in *Conjugated Conducting Polymers*, Ed. H. Kiess, Vol **102**, pp 217–304, Springer-Varlag, Berlin, Heidelberg, New York (1992).
3. M. Mehring, in *Low-Dimensional Conductors and Superconductors, Proceedings of a NATO Advanced Study Institute*, Ed. By D. Jerome and L.G. Caron, Vol **155**, pp 185–93, Plenum, New York (1987).
4. S. Roth and H. Bleier, *Adv. Phys.* **36**, 385 (1987).

5. J.R. Morton, *Chem. Rev.* **64**, 453 (1964).

6. K. Mizoguchi, *Jpn. J. Appl. Phys.* **34**, 1–19 (1995).

7. S. Kuroda, *Int. J. Mod. Phys. B.* **9**, 221–60 (1995).

8. A. Abragam, *The Principles of Nuclear Magnetism*, Oxford University Press, Oxford (1961).

9. W. Gordy, *Theory and Application of Electron Spin Resonance*, John Wiley & Sons, New York (1980).

10. M. Mehring, *Principles of High Resolution NMR in Solids*, Springer, Berlin, Heidleberg (1983).

11. C.P. Slichter, *Principle of Magnetic Resonance*, 3rd edn. Springer, Berlin, Heidelberg (1989).

12. J.A. Pople and S.H. Walmsley, *Mol. Phys.* **5**, 15 (1962).

13. S.E. Brazovskii and N.N. Kirova, *Sov. Sci. Rev. A. Phys.* **5**, 99–264 (1984).

14. J.C.W. Chien, *Polyacetylene*, Academic, New York (1984).

15. J.L. Brédas and G.B. Street, *Acc. Chem. Res.* **18**, 309 (1985).

16. R.R. Chance, D.S. Boudreaux, J.L. Brédas and R. Silbey, in *Handbook of Conducting Polymers*, Ed. T. Skotheim, pp 825–57, Marcel Dekker, New York (1986).

17. J.L. Brédas, in *Handbook of Conducting Polymers*, Ed. By T. Skotheim, pp 859–914, New York, Marcel Dekker, (1986).

18. D. Baeriswyl, D.K. Campbell and S. Mazumdar, in *Conjugated Conducting Polymers*, Ed. H.G. Kiess, Vol **102**, pp 107, Sringer-Verlag, Berlin, Heidelberg (1992).

19. L. Yu, *Solitons and Polarons in Conducting Polymers*, World Scientific, Singapore (1988).

20. L. Mihaly, S. Pekker and A. Janossy, *Synth, Met.* **1**, 349–55 (1979/1980).

21. S. Ikehata, M. Druy, T. Woerner, A.J. Heeger and A.G. MacDiarmid, *Solid St. Commun.* **39**, 1239 (1981).

22. K. Mizoguchi, S. Masubuchi and K. Kume, to be published.

23. K. Mizoguchi, K. Kume, J. Tanaka and M. Tanaka, to be published.

24. T. Tsukamoto, Master Degree, Tokyo Metropolitan University, (1988).

25. J. R. Hendrickson and M.P. Tabbey, *J. Mag. Res.* **43**, 282–7 (1981).

26. W.K. Rhim, A. Pines and J.S. Waugh, *Phys. Rev.* **B3**, 684 (1971).

27. M. Mehring, H. Seidel, H. Weber and G. Wegner, *J. Phys. Colloq.* **44**, C3 217–22 (1983).

28. H. Weber, *Ph. D. Dissertation*, University of Dortmund (1983).

29. M. Helmle, *Thesis*, University of Stuttgart (1984).

30. B. Meurer, P. Spegt, G. Weill, C. Mathis and B. Francois, *Solid St. Commun.* **44**, 201–4 (1982).

31. B. Meurer, P. Spegt and G. Weill, *J. Phys. E* **16**, 403–7 (1983).

32. M. Ziliox, B. Francois, C. Mathis, B. Meurer, P. Spegt and G. Weill, *J. Phys. Colloq.* **44**, C3 361–4 (1983).

33. H. Naarman and N. Theophilou, *Synth. Met.* **22**, 1 (1987).

34. K. Mizoguchi, T. Tsukamoto, K. Kume, K. Akagi and H. Shirakawa, Proc. of ICSM, **96**, Synth. Met. in press.

35. R.H. Baughman, S.L. Hsu, G.P. Pez and A.J. Signorelli, *J. Chem. Phys.* **68**, 5405–9 (1978).

36. R.H. Baughman and S.L. Hsu, *J. Polym. Sci.: Polym. Lett. Ed.* **17**, 185–93 (1979).

37. G. Lieser, G. Wegner, W. Müller and V. Enkelmann, *Makromol. Chem., Rapid Commun.* **1**, 621–6 (1980).

38. J.C.W. Chien, F.E. Karasz and K. Shimamura, *J. Polym. Sci.: Polym. Lett. Ed.* **20**, 97–102 (1982).

39. R.H. Baughman, S.L. Hsu, L.R. Anderson, G.P. Pez and A.J. Signorelli, in *Molecular Metals*, Edited by W.E. Hatfield, Vol **6**, pp 187–202, Plenum Press, New York (1979).

40. R.H. Baugham, B.E. Kohler, I.J. Levy and C. Spangler, *Synth. Met.* **11**, 37–52 (1985).

41. T. Akaishi, K. Miyasaka, I. Ishikawa, H. Shirakawa and S. Ikeda, *Rep. Prog. Polym. Phys. Jpn.* **22**, 125-6 (1979).

42. K. Shimamura, F.E. Karasz, J.A. Hirsh and J.C.W. Chien, *Makromol. Chem. Rapid Commun.* **2**, 473 (1981).

43. C.R. Fincher Jr, C.E. Chen, A.J. Heeger, A.G. MacDiarmid and J.B. Hastings, *Phys. Rev. Lett.* **48**, 100 (1982).

44. V. Enkelmann, M. Monkenbusch and G. Wegner, *Polymer* **23**, 1581 (1982).

45. G. Lieser, G. Wegner, W. Müller, V. Enkelmann and W.H. Meyer, *Makromol. Chem. Rapid Commun.* **1**, 627–32 (1980).

46. G. Lieser, G. Wegner, R. Weizenhoffer and L. Brombacher, *Polymer Preprints* **25**, 221 (1984).

47. C.R. Fincher Jr, *Synth. Met.* **6**, 243–63 (1983).

48. H. Kahlert, A. Leitner and G. Leising, *Synth. Met.* **17**, 467 (1987).

49. P. Kovacic, M.B. Feldman, J.P. Kovacic and J.B. Lando, *J. Appl. Polym. Sci.* **12**, 1735–43 (1968).

50. L.W. Shacklette, R.R. Chance, D.M. Ivory, G.G. Miller and R.H. Baughman, *Synth. Met.* **1**, 307–20 (1979).

51. F. Teraoka and T. Takahashi, *J. Macromol. Sci.-Phys.* **B18**, 73–82 (1980).

52. C.R. Bruce, *Phys. Rev.* **107**, 43 (1957).

53. B.R. Weinberger, E. Ehrenfreund, A. Pron, A.J. Heeger and A.G. MacDiarmid, *J. Chem. Phys.* **72**, 4749–55 (1980).

54. S. Kuroda, M. Tokumoto, N. Kinoshita and H. Shirakawa, *J. Phys. Soc. Jpn.* **51**, 693–4 (1982).

55. D.A. Wigley, *Mechanical Properties of Materials at Low Temperatures*, Plenum Press, New York (1971).

56. N. Mermilliod, L. Zuppiroli and B. Francois, *J. Phys. (France)* **41**, 1453–8 (1980).

57. G. Leising and H. Kahlert, *J. Phys. Colloq.* **44**, C3 111–14 (1983).

58. R.J. Schweizer, K. Menke, W. Gohring and S. Roth, *Mol. Cryst. Liq. Cryst.* **117**, 181–4 (1985).

59. W. Winokur, Y.B. Moon, A.J. Heeger, J. Barker, D.C. Bott and H. Shirakawa, *Phys. Rev. Lett.* **58**, 2329 (1987).

60. Y.W. Park, A.J. Heeger, M.A. Druy and A.G. MacDiarmid, *J. Chem. Phys.* **73**, 946 (1980).

61. K. Mizoguchi, K. Kume, S. Masubuchi and H. Shirakawa, *Solid St. Commun.* **59**, 465–8 (1986).

62. K. Mizoguchi, K. Kume, S. Masubuchi and H. Shirakawa, *Synth. Met.* **17**, 405–11 (1987).

63. Y-C. Chen, K. Akagi and H. Shirakawa, *Synth. Met.* **14**, 173–8 (1986).

64. D.C. Bott, C.S. Brown, C.K. Chai, N.S. Walker, W.J. Feast, P.J.S. Foot, P.D. Calvert, N.C. Billingham and R.H. Friend, *Synth. Met.* **14**, 245 (1986).

65. K. Akagi and H. Shirakawa, *Synth. Met.* **60**, 85 (1993).

66. J. Tsukamoto, A. Takahashi and K. Kawasaki, *Jpn. J. Appl. Phys.* **29**, 125 (1990).

67. J. Tsukamoto, *Adv. Phys.* **41**, 509–546 (1992).

68. K Akagi, K. Sakamaki, H. Shirakawa and H. Kyotani, *Synth. Met.* **69**, 29–30 (1995).

69. T. Akaishi, K. Miyasaka, K. Ishikawa, H. Shirakawa and S. Ikeda, *J. Polym. Sci.: Polym. Phys. Ed.* **18**, 745–50 (1980).

70. A. Bartl, J. Fröhner and S. Roth, *Synth. Met.* **55-57**, 613–17 (1993).

71. H.W. Gibson, R.J. Weagley, R.A. Mosher, S. Kaplan, W.M. Prest Jr, and A.J. Epstein, *Mol. Cryst. Liq. Cryst.* **117**, 315–18 (1985).

72. K. Holczer, C. Mathis and M. Ziliox, *Mol. Cryst. Liq. Cryst.* **117**, 431–8 (1985).

73. D. Baeriswyl and K. Maki, *Phys. Rev.* **B38**, 3135–41 (1988).

74. P. Vogl and D.K. Campbell, *Phys. Rev.Lett.* **62**, 2012–15 (1989).

75. M.E. Horton, R.H. Friend, P.J.S. Foot, N.C. Billingham and P.D. Calvert, *Synth. Met.* **17**, 395–400 (1987).

76. Z.H. Wang, N. Theophilou, D.B. Swanson, A.G. MacDiarmid and A.J. Epstein, *Phys. Rev.* **B44**, 12070 (1991).

77. K. Mizoguchi, H. Sakurai, F. Shimizu, S. Masubuchi and K. Kume, *Synth. Met.* **68**, 239–42 (1995).

78. K. Mizoguchi, K. Kume and H. Shirakawa, *Solid St. Commun.* **50**, 213–18 (1984).

79. K. Mizoguchi, K. Kume and H. Shirakawa, *Synth. Met.* **17**, 439–45 (1987).

80. K. Mizoguchi, S. Komukai, T. Tsukamoto, K. Kume, M. Suezaki, K. Akagi and H. Shirakawa, *Synth. Met.* **28**, D393–8 (1989).

81. K. Mizoguchi, *Makromol. Chem., Macromol. Symp.* **37**, 53–66 (1990).

82. K. Mizoguchi, S. Masubuchi, K. Kume, K. Akagi and H. Shirakawa, *Phys. Rev.* **B51**, 8864–73 (1955).

83. W.E. Blumberg, *Phys. Rev.* **119**, 79 (1960).

84. H. Cailleau, A. Girad, F. Moussa and C.M.E. Zeyen, *Solid St. Commun.* **29**, 259 (1979).

85. J.L. Baudour and H. Cailleau, *Acta Cryst. B* **33**, 1773–80 (1977).

86. J.L. Baudour, Y. Delugeard and P. Rivet, *Acta Cryst. B* **34**, 625–8 (1978).

87. J.L. Baudour, L. Toupet, Y. Delugeard and S. Ghemid, *Acta Cryst. C* **42**, 1211–17 (1986).

88. C.S. Yannoni and T.C. Clarke, *Phys. Rev. Lett.* **51**, 1191 (1983).

89. M.J. Duijvestijn, A. Manenschihn, J. Smidt and R.A. Wind, *J. Mag. Res.* **64**, 461–9 (1985).

90. R. Willstatter and C.W. Moore, *Chem. Ber.* **40**, 2655 (1907).

91. A.G. Green and A.E. Woodhead, *J. Chem. Soc.* **97**, 2388 (1910).

92. S. Kaplan, E.M. Conwell, A.F. Richter and A.G. MacDiarmid, *Synth. Met.* **29**, 235–42 (1989).

93. A.F. Richter, A. Ray, K.V. Ramanathan, S.K. Manohar, G.T. Furst, S.J. Opela, A.G. MacDiarmid and A.J. Epstein, *Synth. Met.* **29**, 243–9 (1989).

94. A.M. Kenwright, W.J. Feast, P. Adams, A.J. Milton, A.P. Monkman and B.J. Say, *Synth. Met.* **55**, 666–71 (1993).

95. A. Abragam and B. Bleany, *Electron Paramagnetic Resonance of Transition Ions*, Clarendon Press, Oxford (1970).

96. L. Kevan and L.E. Kispert, *Electron Spin Double Resonance Spectroscopy*, John Wiley & Sons, New York (1976).

97. M. Dorio and J Freed, *Multiple Electron Resonance Spectroscopy*, Plenum, New York (1979).

98. S. Kuroda and H. Shirakawa, *Solid St. Commun.* **43**, 591–4 (1982).

99. A. Grupp and M. Mehring, in *Modern Pulsed and Continuous-Wave Electron Spin Resonance*, (Ed.) by L. Kevan and M.K. Bowman, Wiley, New York (1990).

100. W.P. Su, J.R. Schrieffer and A.J. Heeger, *Phys. Rev. Lett.* **42**, 1698 (1979).

101. K.R. Subbaswamy and M. Grabowski, *Phys. Rev.* **B24**, 2168 (1981).

102. S. Kuroda, H. Bando and H. Shirakawa, *Solid St. Commun.* **50**, 893 (1984).

103. S. Kuroda, H. Bando and H. Shirakawa, *J. Phys. Soc. Jpn.* **54**, 3956–65 (1985).

104. S. Kuroda and H. Shirakawa, *Phys. Rev.* **B35**, 9380–2 (1987).

105. S. Kuroda and H. Shirakawa, *J. Phys. Soc. Jpn.* **61**, 2930–42 (1992).

106. H. Käss, P. Höfer, A. Grupp, P.K. Kahol, R. Weizenhofer, G. Wegner and M. Mehring, *Europhys. Lett.* **4**, 947–51 (1987).

107. M. Mehring, A. Grupp, P. Höfer and H. Käss, *Synth. Met.* **28**, D399–406 (1989).

108. A.J. Heeger and J.R. Schrieffer, *Solid St. Commun.* **48**, 207–10 (1983).

109. S. Kuroda, M. Tokumoto, N. Kinoshita, T. Ishiguro and H. Shirakawa, *J. Phys. Colloq.* **44**, C3 303–6 (1983).

110. H. Thomann and L.R. Dalton, in *Handbook of Conducting Polymers* , (ed.) T.A. Skotheim, Vol **2**, pp. 1157, Marcel Dekker, New York (1986).

111. K. Yonemitsu, Y. Ono and Y. Wada, *J. Phys. Soc. Jpn.* **57**, 3875 (1988).

112. C.T. White, F.W. Kutzler and M. Cook, *Phys. Rev. Lett.* **56**, 252–5 (1986).

113. Z.G. Soos and S. Ramasesha, *Phys. Rev. Lett.* **51**, 2374 (1983).

114. J.E. Hirsh and M. Grabowski, *Phys. Rev. Let.* **52**, 1713 (1984).

115. M. Sasai and H. Fukutome, *Solid St. Commun.* **51**, 609–12 (1984).

116. H. Thomann, L.R. Dalton, Y. Tomkiewicz, N.S. Shiren and T.C. Clarke, *Phys. Rev. Lett.* **50**, 533–6 (1983).

117. H. Thomann, L.R. Dalton, M.Grabowski and T.C. Clarke, *Phys. Rev.* **B31**, 3141–3 (1985).

118. S. Kuroda and H. Shirakawa, *Solid St. Commun.* **59**, 261–5 (1986).

119. S. Kuroda and H. Shirakawa, *Synth. Met.* **17**, 423–8 (1987).

120. R.H. Friend, D.D.C. Bradley and P.D. Townsend, *J. Phys. D: Appl. Phys.* **20**, 1367 (1987).

121. L.S. Swanson, J. Shinar and K. Yoshino, *Phys. Rev. Lett.* **65**, 1140–3 (1990).

122. K.E. Ziemelis, A.T. Hussain, D.D.C. Bradley, R.H. Friend, J. Rühe and G. Wegner, *Phys. Rev. Lett.* **66**, 2231–4 (1991).

123. L.S. Swanson, P.A. Lane, J. Shinar and F. Wudl, *Phys. Rev.* **B44**, 10617–21 (1991).

124. L.S. Swanson, J. Shinar, A.R. Brown, D.D.C. Bradley, R.H. Friend, P.L. Burn, A.Kraft and A.B. Holmes, *Synth. Met.* **55–57**, 241–8 (1993).

125. X. Wei, B.C. Hess, Z.V. Vardeny and F. Wudl, *Phys. Rev. Lett.* **68**, 666–9 (1992).

126. J.H. Burroughes, D.D.C. Bradley, A.R. Brown, R.N. Marks K. Mackay, R.H. Friend, P.L. Burns and A.B. Holmes, *Nature* **347**, 539 (1990).

127. D. Braun and A.A.J. Heeger, *Phys. Rev. Lett.* **58**, 1982 (1991).

128. H.A. Mizes and E.M. Conwell, *Phys. Rev. Lett.* **70**, 1505–8 (1993).

129. H.A. Mizes and E.M. Conwell, *Synth. Met.* **68**, 145–51 (1995).

130. S. Kuroda, T. Noguchi and T. Ohnishi, *Phys. Rev. Lett.* **72**, 286–9 (1994).

131. S. Kuroda, K. Murata, T. Noguchi and T. Ohnishi, *J. Phys. Soc. Jpn.* **64**, 1363–70 (1995).

132. Y. Shimoi, S. Abe, S. Kuroda and K. Murata, *Solid St. Commun.* **95**, 137–41 (1995).

133. S. Kuroda, I. Murase, T. Ohnishi and T. Noguchi, *Synth. Met.* **17**, 663–6 (1987).

134. T. Ohnishi, T. Noguchi, T. Nakano, M. Hirooka and I. Murase, *Synth. Met.* **41–43**, 309 (1991).

135. I. Murase, T. Ohnishi, T. Noguchi and M. Hirooka, *Polym. Commun.* **25**, 317 (1984).

136. P. Brendel, A. Grupp, M. Mehring, R. Schenk, K. Müllen and W. Huber, *Synth. Met.* **45**, 49–57 (1991).

137. M. Baumgarten, L. Gherghel and S. Karabunarliev, *Synth. Met.* **69**, 633–6 (1995).

138. L.S. Swanson, J. Sinar, P.A. Lane, B.C. Hess and F.Wudl, *Synth. Met.* **49–50**, 481–9 (1992).

139. J.M. Leng, R.P. McCall, K.R. Cromack, Y. Sun, S.K. Manohar, A.G. MacDiarmid and A.J. Epstein, *Phys. Rev.* **B48**, 15719–31 (1993).

140. W.P. Su, and A.J. Epstein, *Phys. Rev. Lett.* **70**, 1497–500 (1993).

141. K.A. Koplin, S. Jasty, S.M. Long, S.K. Manohar, Y. Sun, A.G. MacDiarmid and A.J. Epstein, *Phys. Rev. Lett.* **72**, 3206–9 (1994).

142. S.M. Long, Y. Sun, A.G. MacDiarmid and A.J. Epstein, *Phys. Rev. Lett.* **72**, 3210–13 (1994).

143. M. Nechtschien, F. Devreux, R.L. Greene, T.C. Clarke and G.B. Street, *Phys. Rev. Lett.* **44**, 356–9 (1980).

144. F. Devreux, K. Holczer, M. Nechtschein, T.C. Clarke and R.L. Greene, in *Physics in One Dimension*, pp 194–200, Springer-Verlag, Berlin (1981).

145. K. Holczer, F. Devreux, M. Nechtschein and J.P. Travers, *Solid St. Commun.* **39**, 881–4 (1981).

146. K. Holczer, J.P. Boucher, F. Devreux and M. Nechtschein, *Phys. Rev.* **B23**, 1051–63 (1981).

147. M. Nechtschein, F. Devreux, F. Genoud, M. Guglielmi and K. Holczer, *Phys. Rev.* **B27**, 61–78 (1983).

148. K. Kume, K. Mizuno, K. Mizoguchi, K. Nomura, J. Tanaka, M. Tanaka, H. Fujimoto and H. Shirakawa, *J. Magn. Magn. Mater.* **31–34**, 1151–2 (1983).

149. J. Alizon, J.P. Blanc, J. Gallice, H. Robert and C. Thibaud, *Solid St. Commun.* **39**, 169–71 (1981).

150. F. Masin, G. Gusman and R. Deltour, *Solid St. Commun.* **39**, 505–7 (1981).

151. W.G. Clark, K. Glover, G. Mozurkewich, C.T. Murayama, J. Sanny, S. Etemad and M. Maxfield, *J. Phys. Colloq.* **44**, C3 239–45 (1983).

152. J.C. Scott and T.C. Clarke, *J. Phys. Colloq.* **44**, C3 365–8 (1983).

153. P.E. Sokol, J.R. Gaines, S.I. Cho, D.B. Tanner, H.W. Gibson and A.J. Epstein, *Synth. Met.* **10**, 43–9 (1984).

154. M. Ziliox, P. Spegt, C. Mathis, B. Francois and G. Weill, *Solid St. Commun.* **51**, 393–6 (1984).

155. K. Kume, K. Mizoguchi and H. Shirakawa, *Mol. Cryst. Liq. Cryst.* **118**, 469–72 (1985).

156. K. Mizoguchi, K. Kume and H. Shirakawa, *Mol. Cryst. Liq. Cryst.* **118**, 459–62 (1985).

157. K. Kume and K. Mizoguchi, *Progr. Theor. Phys. Suppl.* **113**, 91–6 (1993).

158. K. Mizoguchi, H. Sakurai, F. Shimizu, S. Masubuchi and K. Kume, *Synth. Met.* **69**, 51–2 (1995).

159. Y. Tomkiewicz, N.S. Shiren, T.D. Schultz, K. Mortensen, M.L.W. Thewalt, J.D. Kuptsis, R.G. Schad, B.H. Robinson, T.C. Clarke, G.B. Street, H. Thomann, L.R. Dalton and H.B. Brom, in *Physics in One Dimension. Proceedings of an International Conference*, pp 214–17, Springer-Verlag, Berlin (1981).

160. N.S. Shiren, Y. Tomkiewicz, T.G. Kazyaka, A.R. Taranko, H. Thomann, L. Dalton and T.C. Clarke, *Solid St. Commun.* **44**, 1157–60 (1982).

161. N.S. Shiren, Y. Tomkiewicz, H. Thomann, L. Dalton and T.C. Clarke, *J. Phys. Colloq.* **44**, C3–223 (1983).

162. L.R. Dalton, H. Thomann, A. Morrobel-Sosa, C. Shiu, M.E. Galvin, G.E. Wnek, Y. Tomkiewicz, N.S. Shiren, B.H. Robinson and A.L. Kwiram, *J. Appl. Phys.* **54**, 5583–91 (1983).

163. J. Tang, C.P. Lin, M.K. Bowman, J.R. Norris, J. Isoya and H. Shirakawa, *Phys. Rev.* **B28**, 2845 (1983).

164. B.H. Robinson, J.M. Schurr, A.L. Kwiram, H. Thomann, H. Kim, A. Morrobel-Sosa, P. Bryson and L.R. Dalton, *J. Phys. Chem.* **89**, 4994–5002 (1985).

165. H. Thomann, H. Jin and G.L. Baker, *Phys. Rev. Lett.* **59**, 509–12 (1987).

166. I.B. Goldberg, H.R. Crowe, P.R. Newman, A.J. Heeger and A.G. MacDiarmid, *J. Chem. Phys.* **70**, 1132–6 (1979).

167. B.R. Weinberger, J. Kaufer, A.J. Heeger, A. Pron and A.G. MacDiarmid, *Phys. Rev.* **B20**, 223–30 (1979).

168. S. Ikehata, J. Kaufer, T. Woerner, A. Pron, M.A. Druy, A. Sivak, A. J. Heeger and A.G. MacDiarmid, *Phys. Rev. Lett.* **45**, 1123–6 (1980).

169. W.P. Su, J.R. Schrieffer and A.J. Heeger, *Phys. Rev.* **B22**, 2099–111 (1980).

170. J.L. Brédas, J.C. Scott, K. Yakushi and G.B. Street, *Phys. Rev.* **B30**, 1023–5 (1984).

171. This notation in units of rad/s will be mainly used in this review; to convert to the diffusion coefficient $D_\parallel$ cm^2/s, multiply a square of unit hopping length b^2 cm^2.

172. M.J. Hennessy, C.D. McElwee and P.M. Richards, *Phys. Rev.* **B7**, 930 (1973).

173. W.G. Clark, K. Glover, G. Mozurkewich, S. Etemad and M. Maxfield, *Mol. Cryst. Liq. Cryst.* **117**, 447 (1985).

174. M. Nechtschein, F. Devreux, F. Genoud, M. Guglielmi and K. Holczer, *J. Phys. Colloq.* **44**, C3 209–16 (1983).

175. F. Genoud, M. Nechtschein, K. Holczer, F. Devreux and M. Guglielmi, *Mol. Cryst. Liq. Cryst.* **96**, 161–70 (1983).

176. K. Maki, *Phys. Rev.* **B26**, 4539–42 (1982).

177. K. Maki, *Phys. Rev.* **B26**, 2187–91 (1982).

178. K. Maki, *Phys. Rev.* **B26**, 2181–6 (1982).

179. H.W. Gibson, R.J. Weagley, R.A. Mosher, S. Kaplan, W.M. Prest Jr, and A.J. Epstein, *Phys. Rev.* **B31**, 2338–42 (1985).

180. M. Ziliox, B. Francois, C. Mathis, B. Meurer, G. Weill and K. Holczer, *Mol. Cryst. Liq. Cryst.* **117**, 483–6 (1985).

181. F. Masin and G. Gusman, *Phys. Rev.* **B36**, 2153–7 (1987).

182. C.A. Sholl, *J. Phys. C: Solid St. Phys.* **14**, 447 (1981).

183. M.A. Butler, L.R. Walker and Z.G. Soos, *J. Chem. Phys.* **64**, 3592 (1976).

184. P.E. Sokol, J.R. Gaines, S.I. Cho, D.B. Tanner, H.W. Gibson and A.J. Epstein, *J. Phys. Colloq.* **44**, C3 349–52 (1983).

185. F. Devreux, *Phys. Rev.* **B25**, 6609 (1982).

186. H. Thomann and G.L. Baker, *J. Am. Chem. Soc.* **109**, 1569–70 (1987).

187. K. Kume, K. Mizuno, K. Mizoguchi, K. Nomura, J. Tanaka, M. Tanaka and H. Fujimoto, *Mol. Cryst. Liq. Cryst.* **83**, 1081–8 (1982).

188. H. Thomann, L.R. Dalton, M.E. Galvin, G.E. Wnek and Y. Tomkiewicz, *J. Phys. Colloq.* **44**. C3 313–16 (1983).

189. P.K. Kahol, M. Mehring and X. Wu, *J. Phys.* **46**, 1683–91 (1985).

190. P.K. Kahol, M. Mehring and X. Wu, in *Electronic Properties of Polymers and Related Compounds*, Ed. H. Kuzmany, M. Mehring and S. Roth, Vol **63**, pp 271–4, Springer-Verlag, Berlin, Heildelberg (1985).

191. R.S. Denis, E.J. Hustedt, C. Mailer and B.H. Robinson, *J. Phys. Chem.* **94**, 4716–23 (1990).

192. This figure is twice that reported earlier, since the directional quantum number was not taken into account.

193. J. Isoya, private communication.

194. J. Isoya, H. Nagasawa, H. Shirakawa, M.K. Bowman, C.P. Lin, J. Tang and J.R. Norris, *Synth. Met.* **17**, 215–9 (1987).

195. P.K. Kahol and M. Mehring, *J. Phys. C: Solid St. Phys.* **19**, 1045–54 (1986).

196. M. Ogata and Y. Wada, *Prog. Theor. Phys. Suppl.* no. 94, 115–27 (1988).

197. Y Wada and J.R. Schrieffer, *Phys. Rev,* **B18**, 3987 (1978).

198. S. Jeyadev and E M. Conwell, *Phys. Rev.* **B36**, 3284–93 (1987).

199. Y. Wada, *Prog. Thor. Phys. Suppl.* **113**, 1–23 (1993).

200. H. Bleier, P. Bernier, D. Schafer-Siebert and S. Roth, *Synth. Met.* **28**, D407–12 (1989).

201. Y. Cao, J.R. Gaines, A.J. Epstein, G. Arbuckle and A.G. MacDiarmid, *Phys. Rev.* **40**, 3176–81 (1989).

202. C. Jeandey, J.P. Boucher, F. Ferrieu and M. Nechtschein, *Solid St. Commun.* **23**, 673 (1977).

203. S. Kivelson, *Phys. Rev.* **B25**, 3798–21 (1982).

204. K. Fesser, A.R. Bishop and D.K. Campbell, *Phys. Rev.* **B27**, 4804 (1983).

205. T.C. Chung, J.H. Kaufman, A.J. Heeger and F. Wudl, *Mol. Cryst. Liq. Cryst.* **118**, 205–15 (1985).

206. A.J. Epstein, H. Rommelmann, M.A. Druy, A.J. Heeger and A.G. MacDiarmid, *Solid St. Commun.* **38**, 683–7 (1981).

207. P. Wzietek, F. Creuzet, C. Bourbonnais, D. Jérome, K. Bechgaard and P. Batail, *J. Phys. I France* **3**, 171–201 (1993).

208. A.J. Epstein, J. Joo, R.S. Kohlman, G. Du, A.G. MacDiarmid, E.J. Oh, Y. Min, J. Tsukamoto, H. Kaneko and J.P. Pouget, *Synth. Met.* **65**, 149–57 (1994).

209. N.S. Sariciftci, A.J. Heeger and Y. Cao, *Phys. Rev.* **B49**, 5988–92 (1994).

210. R.T. Schumacher and C.P Slichter, *Phys. Rev.* **101**, 58 (1956).

211. M. Tokumoto, N. Kinoshita, S. Kuroda, T. Ishiguro, H. Shirakawa and H. Nemoto, *J. Phys. Colloq.* **44**, C3 299–302 (1983).

212. G. Feher and A.F. Kip, *Phys. Rev.* **98**, 337 (1955).

213. F.J. Dyson, *Phys. Rev.* **98**, 349 (1955).

214. J. Chen, T-C. Chung, F. Moraes and A.J. Heeger, *Solid St. Commun.* **53**, 757–63 (1985).

215. F. Moraes, J. Chen, T-C Chung and A.J. Heeger, *Synth. Met.* **11**, 271–92 (1985).

216. J.C.W. Chien, J.M. Warakomski, F.E. Karasz, W.L. Chia and C.P. Lillya, *Phys. Rev.* **B28**, 6937–52 (1983).

217. J.C.W. Chien, J.M. Warakomski and F.E. Karasz, *J. Chem. Phys.* **82**, 2118–21 (1985).

218. T-C. Chung, F. Moraes, J.D. Flood and A.J. Heeger, *Phys. Rev.* **B29**, 2341-3 (1984).

219. J. Chen and A.J. Heeger, *Synth. Met.* **24**, 311–27 (1988).

220. A.J. Epstein, R.W. Bigelow, H. Rommelmann, H.W. Gibson, R.J. Weagley, A. Feldblum, D.B. Tanner, J.P. Pouget, J.C. Pouxviel, R. Comes, P. Robin and S. Kivelson, *Mol. Cryst. Liq. Cryst.* **117** , 147–54 (1985).

221. F. Shimizu, *PhD thesis*, Tokyo Metropolitan University (1994).

222. N. Theophilou, D.B. Swanson, A.G. MacDiarmid, A. Chakraborty, H.H.S. Javadi, R.P. McCall, S.P. Treat, F. Zuo and A.J. Esptein, *Synth. Met.* **28**, D35–42 (1989).

223. Y. Nogami, H. Kaneko, T. Ishiguro, A. Takahashi, J. Tsukamoto and N. Hosoito, *Synth. Met.* **76**, 583–6 (1990).

224. Y. Tomkiewicz, T.D. Schultz, H.B. Brom, A.R. Taranko, T.C. Clarke and G.B. Street, *Phys. Rev.* **B24**, 4348–63 (1981).

225. E.M. Conwell and H.A. Mizes, *Synth. Met.* **65**, 203–9 (1994).

226. B. Horovitz, *Phys. Rev. Lett.* **55**, 1429 (1985).

227. H-Y. Choi and E.J. Mele, *Phys. Rev.* **B34**, 8750–7 (1986).

228. S. Kivelson and A.J. Heeger, *Synth. Met.* **17**, 183–8 (1987).

229. D.B. Tanner, G.L. Doll, A.M. Rao, P.C. Eklund, G.A. Arbuckle and A.G. MacDiarmid, *Synth. Met.* **28**, D141–6 (1989).

230. Y.H. Kim and A.J. Heeger, *Phys. Rev.* **40**, 8393–8 (1989).

231. J. Joo, G. Du, J. Tsukamoto and A.J. Epstein, to be published.

232. G.J. Baker, J.H. Holloway, J.B. Raynor and H. Selig, *Synth. Meth.* **20**, 323–31 (1987).

233. J.L. Brédas, *Mol. Cryst. Liq. Cryst.* **118**, 49–56 (1985).

234. J.L. Brédas, F. Wudl and A.J. Heeger, *Solid St. Commun.* **63**, 577–80 (1987).

235. D. Baeriswyl, in *Electronic Properties of Conjugated Polymers III*, Ed. by H. Kuzmany, M. Mehring and S. Roth, Vol **91**, pp 54–9, Springer-Verlag, Berlin (1989).

236. E.M. Conwell and H.A. Mizes, *Synth. Met.* **57**, 4284–9 (1993).

237. Y. Shimoi and S. Abe, *Phys. Rev.* **B50**, 14781–4 (1994).

238. J.C. Scott, P. Pfluger, M.T. Krounbi and G.B. Street, *Phys. Rev.* **B28**, 2140–5 (1983).

239. J.C. Scott, J.L. Brédas, K. Yakushi, P. Pfluger and G.B. Street, *Synth. Met.* **9**, 165–72 (1984).

240. J.C. Scott, J.L. Brédas, J.H. Kaufman, P. Pfluger, G.B. Street and K. Yakushi, *Mol. Cyrst. Liq. Cryst.* **118**, 163–70 (1985).

241. J.H. Kaufman, N. Colaneri, J.C. Scott and G.B. Street, *Phys. Rev. Lett.* **53**, 1005–8 (1984).

242. J.H. Kaufman, N. Colaneri, J.C. Scott, K.K. Kanazawa and G.B. Street, *Mol. Cryst. Liq. Cryst.* **118**, 171–7 (1985).

243. F. Genoud, M. Guglielmi, M. Nechtschein, E. Genies and M. Salmon, *Phys. Rev. Lett.* **55**, 118–21 (1985).

244. M. Nechtschein, F. Devreux, F. Genoud, E. Vieil, J.M. Pernaut and E. Genies, *Synth. Meth.* **15**, 59–78 (1986).

245. F. Devreuz, *Europhys. Lett.* **1**, 233–9 (1986).

246. P. Pfluger and G.B. Street, *J. Phys. Colloq.* **44**, C3 609–14 (1983).

247. P. Pfluger and G.B. Street, *J. Chem. Phys.* **80**, 544–53 (1984).

248. P. Pfluger, U.M. Gubler and G.B. Street, *Solid St. Commun.* **49**, 911–15 (1984).

249. M.A. Druy, *Synth. Met.* **15**, 243 (1986).

250. L.F. Warren and D.P. Anderson, *J. Electrochem.* **134**, 101 (1987).

251. P. Bätz, D. Schmeisser and W. Göpel, *Phys. Rev.* **B43**, 9178–89 (1991).

252. M. Yamaura, T. Hagiwara, M. Hirasaka, T. Demura and K. Iwata, *Synth. Met.* **28**, C157–64 (1989).

253. T. Hagiwara, M. Hirasaka, K. Sato and M. Yamaura, *Synth. Met.* **36**, 241–52 (1990).

254. K. Kaneto, S. Hayashi, S. Ura and K. Yoshino, *J. Phys. Soc. Jpn.* **54**, 1146–53 (1985).

255. F. Moraes, D. Davidov, M. Kobayashi, T.C. Chung, J. Chen, A.J. Heeger and F. Wudl, *Synth. Met.* **10**, 169–79 (1985).

256. S. Hayashi, K. Kaneto, K. Yoshino, R. Matsushita and T. Matsuyama, *J. Phys. Soc. Jpn.* **55**, 1971–80 (1986).

257. J. Chen, A.J. Heeger and F. Wudl, *Solid St. Commun.* **58**, 251–7 (1986).

258. M. Schärli, H. Kiess, G. Harbeke, W. Berlinger, K.W. Blazey and K.A. Mueller, *Synth. Met.* **22**, 317–36 (1988).

259. K. Kume, K. Mizuno, K. Mizoguchi, K. Nomura, Y. Maniwa, J. Tanaka, M. Tanaka and A. Watanabe, *Mol. Cryst. Liq. Cryst.* **83**, 1317–22 (1982).

260. K.D. Gourley, C.P. Lillya, J.R. Reynolds and J.C.W. Chien, *Macromol.* **17**, 1025–35 (1984).

261. M.E. Jozefowicz, R. Laversanne, H.H.S. Javadi, A.J. Epstein, J.P. Pouget, X. Tang and A.G. MacDiarmid, *Phys. Rev.* **B39**, 12958–61 (1989).

262. A.G. MacDiarmid, J.C. Chiang, A.F. Richter and A.J. Epstein, *Synth. Met.* **18**, 285–90 (1987).

263. K. Mizoguchi, M. Nechtschein, J-P Travers and C. Menardo, *Phys. Rev. Lett.* **63**, 66–9 (1989).

264. M. Nechtschein, F. Genoud, C. Menardo, K. Mizoguchi, J.P. Travers and B. Villeret, *Synth. Met.* **29**, E211–18 (1989).

265. F. Genoud, M Nechtschein and C. Santier, *Synth. Met.* **55**, 642–7 (1993).

266. K. Mizoguchi, T. Obana, S. Ueno and K. Kume, *Synth. Met.* **55**, 601–6 (1993).

267. A.J. Epstein, J.M. Ginder, F. Zuo, R.W. Bigelow, H-S Woo, D.B. Tanner, A.F. Richter, W-S Huang and A.G. MacDiarmid, *Synth. Met.* **18**, 303–9 (1987).

268. H. Kamimura, *Phil. Mag.* **42**, 763–79 (1980).

269. P. Le Guennec, M. Nechtschein and J.P. Travers, *Synth. Met.* **55–57**, 630–5 (1993).

270. M.N. Bussac and L. Zuppiroli, *Phys. Rev.* **B47**, 5492–6 (1993).

271. M. Peo, S. Roth, K. Dransfeld, B. Tieke, J. Hocker, H. Gross, A. Grupp and H. Sixl, *Solid St. Commun.* **35**, 119–22 (1980).

272. M. Peo, S. Roth and J. Hocker, *Chem. Scr. (Sweden)* **17**, 133–4 (1981).

273. L.R. Anderson, G.P. Pez and S.L. Hsu, *J. Chem. Sol. Chem. Commun.* 1066 (1978).

274. J.F. Kwak, T.C. Clarke, R.L. Greene and G.B Street, *Solid St. Commun.* **31**, 355 (1979).

275. Y.W. Park, J.C. Woo, K.H. Yoo, W.K. Hau, C.H. Choi, T. Kobayashi and H. Shirakawa, *Solid St. Commun.* **46**, 731 (1983).

276. R. Zuzok, A.B. Kaiser, W. Pukacki and S. Roth, *J. Chem. Phys.* **95**, 1270 (1991).

277. S. Masubuchi, S. Kazama, K. Mizoguchi, F. Shimizu, K. Kume, R. Matsushita, and T. Matsuyama, *Synth. Met.* **55–57**, 4866–71 (1993).

278. F. Devreux, F. Genoud, M. Nechtschein and B. Villeret, in *Electronic Properties of Conjugated Polymers*, Vol 76, pp 270–6, Springer-Verlag, Berlin (1987).

279. K. Mizoguchi, K. Misoo, K. Kume, K. Kaneto, T. Shiraishi and K. Yoshino, *Synth. Met.* **18**, 195–8 (1987).

280. J. Tananka, N. Mashita, K. Mizoguchi and K. Kume, *Synth. Met.* **29**, E175–84 (1989).

281. R.S. Kohlman, J. Joo, Y.Z. Wnag, J.P. Pouget, H. Kaneko, T. Ishiguro and A.J. Epstein, *Phys. Rev. Lett.* **74**, 773–6 (1995).

282. K. Mizoguchi, N. Kachi, H. Sakamoto, K. Kume, K. Yoshioka, S. Masubuchi and S. Kazama, Proc. of ICSM '96, Synth. Met. in press.

283. K. Lee, R. Menon, C.O. Yoon and A.J. Heeger, *Phys. Rev.* **B52**, 4779–87 (1995).

284. S. Masubuchi, S. Kazama, R. Matsushita and T. Matsuyama, *Synth. Met.* **69**, 345–6 (1995).

285. S. Masubuchi, S. Kazama, R. Matsushita and T. Matsuyama, to be published.

286. F. Devreux, F. Genoud, M. Nechtschein, J.P. Travers and G. Bidan, *J. Phys. Colloq.* **44**, C3 621–4 (1983).

287. K. Mizoguchi, M. Honda, N. Kachi, F. Shimizu, H. Sakamoto, K. Kume. S. Masubuchi and S. Kazama, *Solid St. Commun.* **96**, 333–7 (1995).

288. R.J. Elliott, *Phys. Rev.* **96**, 266–79 (1954).

289. S. Masubuchi and S. Kazama, *Synth. Met.* **74**, 151–8 (1995).

290. H. Kaneko, T. Ishiguro, K. Sato, T. Hagiwara, M. Yamaura, H. Nishiyama and H. Ishimoto, *Synth. Met.* **55**, 1102–7 (1993).

291. S. Kobayashi, T. Takahashi and W. Sasaki, *J. Phys. Soc. Jap.* **31**, 1442–5 (1971).

292. R. Kubo, A. Kawabata and S. Kobayashi, *Annual review of materials science* **14**, 49–66 (1984).

293. O. Chauvet, S. Paschen, L. Forro, L. Zuppiroli, P. Bujard, K. Kai and W. Wernet, *Synth. Met.* **63**, 115–19 (1994).

294. L. Zuppiroli, M.N. Bussac, S. Paschen, O. Chauvet and L. Forro, *Phys. Rev.* **B50**, 5196–203 (1994).

295. G. Tourillon, D. Gourier, F. Garnier and D. Vivien, *J. Phys. Chem.* **88**, 1049–51 (1984).

296. K. Mizoguchi, M. Honda, S. Masubuchi, S. Kazama and K. Kume, *Jpn. J. Appl. Phys.* **33**, 971–5 (1994).

297. W. Czerwinski, L. Kreja, M. Chrzaszcz and A. Kazubski, *J. Mater. Sci.* **29**, 1191–7 (1994).

298. K.Y. Jen., R. Oboodi and R.L. Elsenbaumer, *Synth. Met.* **15**, 169 (1986).

299. M. Sato, S. Tanaka and K. Kaeriyama, *Synth. Met.* **14**, 289 (1986).

300. S. Hotta, S.D.D.V. Rughooputh, A.J. Heeger and F. Wudl, *Macromolecules* **20**, 212 (1987).

301. S. Masubuchi, S. Kazama, K. Mizoguchi, H. Honda, K. Kume, R. Matsushita and T. Matsuyama, *Synth. Met.* **57**, 4962–7 (1993).

302. H. Kamimura, in *Electron–electron interactions in disordered systems*, pp 555–617, North-Holland, Amsterdam (1985).

303. H.K. Roth, K. Mizoguchi, M. Honda, H. Sakamoto and K. Kume, to be published.

304. M. Reghu, Y. Cao, D. Moses and A.J. Heeger, *Synth. Met.* **57**, 5020–5 (1993).

305. K. Mizoguchi and K. Kume, *Solid St. Commun.* **89**, 971–5 (1994).

306. K. Mizoguchi and K. Kume, *Synth. Met.* **69**, 241–2 (1995).

307. H. Sakamoto, N. Kachi, F. Shimizu, K. Mizoguchi, K. Kume, T. Noguchi and T. Ohnishi, Proc. of ICSM '96, Synth. Met. in press.

308. I. Murase, T. Ohnishi, T. Noguchi, M. Hirooka and S. Murakami, *Mol. Cryst. Liq. Cryst.* **118**, 333–6 (1985).

309. J. Briers, W. Eevers, P. Cos, H.J. Geise, R. Mertens, P. Nagels, X.B. Zhang, G. Van Tendeloo, W. Herrebout and B. Van der Veken, *Polymer* **35**, 4569–72 (1994).

310. A.G. MacDiarmid and A.J. Epstein, *Synth. Met.* **69**, 85–92 (1995).

311. Y. Min, Y. Xia, A.G. MacDiarmid and A.J. Epstein, *Synth. Met.* **69**, 159 (1995).

312. M. Angelopoulos, A. Ray, A.G. MacDiarmid and A.J. Epstein, *Synth. Met.* **21**, 21–30 (1987).

313. P.K. Kahol and B.J. McCormick, *J. Phys., Condens. Matter.* **3**, 7963–72 (1991).

314. P.K. Kahol and B.J. Mccormick, *Phys. Rev.* **B47**, 14588–90 (1993).

315. P.K. Kahol, N.J. Pinto and B.J. McCormick, *Solid St. Commun.* **91**, 21–4 (1994).

316. L.D. Kispert, J. Joseph, G.G. Miller and R.H. Baughman, *J. Chem. Phys.* **81**, 2119–25 (1984).

317. L.D. Kispert, J. Joseph, G.G. Miller and R.H. Baughman, *Mol. Cryst. Liq. Cryst.* **106**, 418 (1984).

318. L.D. Kispert, J. Joseph and R. Drobner, *Synth. Met.* **20**, 209–14 (1987).

319. F. Maurice, C. Fontaine, A. Morisson, J.Y. Goblot and G. Froyer, *Mol. Cryst. Liq. Cryst.* **118**, 319–22 (1985).

320. L.D. Kispert, J. Joseph, G.G. Miller and R.H. Baughman, *Mol. Cryst. Liq. Cryst.* **118**, 313–18 (1985).

321. K. Mizoguchi, K. Kume, J. Tanaka, M. Tanaka and A. Watanabe, unpublished.

322. P.K. Kahol and M. Mehring, *Synth. Met.* **16**, 257–64 (1986).

323. M. Iida, T. Asaji, M.B. Inoue and M. Inoue, *Synth. Met.* **55–57**, 607–10 (1993).

324. Z.H. Wang, C. Li, E.M. Scherr, A.G. MacDiarmid and A.J. Epstein, *Phys. Rev. Lett.* **66**, 1745–8 (1991).

325. Z.H. Wang, E.M. Scherr, A.G. MacDiarmid and A.J. Epstein, *Phys. Rev.* **B45**, 4190–202 (1992).

326. Z.H. Wang, A. Ray, A.G. MacDiarmid and A.J. Epstein, *Phys. Rev.* **B43**, 5373–84 (1991).

327. C.E. Lee, C.H. Lee, K.H. Yoon and J-I Jin, *Synth. Met.* **69**, 427–8 (1995).

328. H.S. Nalwa, *Phys. Rev.* **B39**, 5964–74 (1989).

329. N.S. Sariciftci, M. Reghu, C.O. Yoon and A.J. Heeger, *Bull. Am. Phys. Soc.* **40**, 344 (1995).

330. N.S. Sariciftci, M. Reghu, C.O. Yoon, A. Ersoz and A.J. Heeger, in preparation.

331. G.C. Carter, L.H. Bennett and D.J. Kahan, *Metallic Shifts in NMR*, Pergamon Press, Oxford (1976).

332. T.C. Clarke and J.C. Scott, *Solid St. Commun.* **41**, 389–91 (1982).

333. T. Terao, S. Maeda, T. Yamabe, K. Akagi and H. Shirakawa, *Solid St. Commun.* **49**, 829–32 (1984).

334. M. Karplus and G.K. Frënkel, *J. Chem. Phys.* **35**, 1312 (1961).

335. W.G. Blann, C.A. Fyfe, J.R. Lyerla and C.S. Yannoni, *J. Am. Chem. Soc.* **103**, 4030 (1981).

336. M. Peo, H. Forster, K. Menke, J. Hocker, J.A. Gardner, S. Roth and K. Dransfeld, *Solid St. Commun.* **38**, 467–8 (1981).

337. T.J. Bonagamba, B. Bello Jr, M.V. Giotto, H. Panepucci, C.J. Magon and M.S. Campos, *Synth. Met.* **68**, 103–8 (1995).

338. N.S. Sariciftci, A. Grupp and M. Mehring, *Chem. Phys. Lett.* **192**, 375–8 (1992).

339. N.S. Sariciftci, A. Grupp and M. Mehring, *Synth. Met.* **55–57**, 624–9 (1993).

340. A.W. Overhauser, *Phys. Rev.* **92**, 411–5 (1953).

341. S. Masubuchi and S. Kazama, *Synth. Met.* **69**, 315–6 (1995).

342. A.G. MacDiarmid, J.C. Chiang, M. Halpern, W.S. Huang, S.L. Mu, N.L.D.Somasiri, W.Q. Wu, and S.I. Yaniger, *Mol. Cryst. Liq. Cryst.* **121**, 173 (1985).

343. A.P. Monkman and P.N. Adams, *Synth. Met.* **41–43**, 627 (1991).

344. P.N. Adams, P.J. Laughlin, A.P. Monkman and N. Bernhoeft, *Solid St. Commun.* **91**, 875 (1994).

345. K. Mizoguchi, M. Nechtschein, J.P. Travers and C. Menardo, *Synth. Met.* **29**, E417–24 (1989).

346. K. Mizoguchi, M. Nechtschein and J.P. Travers, *Synth. Met.* **41**, 113–16 (1991).

347. M. Nechtschein, F. Devreux, K. Mizoguchi and J.P. Travers, in *Electronic Properties of Conjugated Polymers III*, (ed.) H. Kuzmany, M. Mehring and S. Roth, Vol **91**, pp 178–83, Springer-Verlag, Berlin (1989).

348. J.P. Pouget, M.E. Józefowicz, A.J. Epstein, X. Tang and A.G. MacDiarmid, *Macromolecules* **24**, 779 (1991).

349. A.J. Epstein, A.G. MacDiarmid and J.P. Pouget, *Phys. Rev. Lett.* **65**, 664 (1990).

350. E.J. Oh, Y. Min, J.M. Wiesinger, S. K. Manohar, E.M. Scherr, P.J. Prest, A.G. MacDiarmid and A.J. Epstein, *Synth. Met.* **55–57**, 977 (1993).

351. K. Kume, K. Mizuno, K. Mizoguchi, K. Nomura, H. Takayama, S. Ishihara, J. Tanaka, M. Tanaka, H. Fujimoto and H. Shirakawa, *J. de Phys.* **44**, C3 353–6 (1983).

352. K. Mizoguchi, F. Shimizu and S. Masubuchi, *Synth. Met.* **41**, 185–8 (1991).

353. F. Shimizu, K. Mizoguchi, S. Masubuchi and K. Kume, *Synth. Met.* **69**, 43–4 (1995).

354. F. Shimizu, K. Mizoguchi, S. Masubuchi and K. Kume, *Synth. Met.* **55**, 720–4 (1993).

355. M. Nechtschein and Y.W. Park, *Synth. Met.* **69**, 77–8 (1995).

356. S. Masubuchi, unpublished data.

357. J.P. Travers, M. Nechtschein and K. Mizoguchi, in *Electronic Properties of Polymers*, (Ed.) H. Kuzmany, M. Mehring and S. Roth, Vol **107**, pp 262–267, Springer-Verlag, Berlin (1992).

358. K. Mizoguchi, unpublished data.

359. M. Kletter, A.G. MacDiarmid, A.J. Heeger, E. Faulques, S. Lefrant, P. Bernier, F. Barbarin, J.P. Blanc, J. P. Germain and H. Robert, *Mol. Cryst. Liq. Cryst.* **83**, 165 (1982).

360. S. Kivelson and A.J. Heeger, *Synth. Met.* **22**, 371–84 (1988).

361. F. Devreux and H. Lecavelier, *Phys. Rev. Lett.* **59**, 2585–7 (1987).

362. F.L. Pratt, W. Hayes, G.R. Mitchell, B. Rossi, M.S. Kiani, B.D. Malhotra, S.S. Pandey, A. Milton and A. P. Monkman, *Synth. Met.* **55**, 677–84 (1993).

363. K. Nagamine and K. Ishida, *Hyperfine Interactions* **32**, 535–49 (1986).

364. M. Nechtschein, C. Santier, J.P. Travers, J. Chroboczek, A. Alix and M Ripert, *Synth. Met.* **18** 311–16 (1987).

365. J.P. Travers and M. Nechtschein, *Synth. Met.* **21**, 135–41 (1987).

366. A. Alix, V. Lemoine, M. Nechtschein, J.P. Travers and C. Menardo, *Synth. Met.* **29**, 457–62 (1989).

367. J.P. Travers, *Synth. Met.* **55**, 731–6 (1993).

368. J.P. Travers, P. Le Guyadec, P.N. Adams, P.J. Laughlin and A.P. Monkman, *Synth. Met.* **65**, 159–66 (1994).

369. J.P. Travers, P. Le Guyadec. P.N. Adams, P.J. Laughlin and A.P. Monkman, *Synth. Met.* **69**, 229–30 (1995).

370. J.E. Fischer, X. Tang, E.M. Scherr, V.B. Cajipe and A.G. MacDiarmid, *Synth. Met.* **41–43**, 661 (1991).

371. S. Kazama, *Synth. Met.* **16**. 77–85 (1986).

372. A.C. Kolbert, S. Caldarelli, K.F. Thier, N.S. Sariciftci, Y. Cao and A.H. Heeger, *Phys. Rev.* **B51**, 1541–5 (1995).

373. J. Joo, Z. Oblakowski, G. Du, J.P. Pouget, E.J. Oh, J.M. Wiesinger, Y. Min, A.G. MacDiarmid and A.J. Epstein, *Phys. Rev.* **B49**, 2977–80 (1994).

374. J. Joo, E.J. Oh, G. Min, A.G. MacDiarmid and A.J. Epstein, *Synth. Met.* **69**, 251–4 (1995).

375. P-Y. Mabboux, J.P. Travers, Y. Nicolau, E. Samuelsen, P.H. Carlsen and B. Francois, *Synth. Met.* **69**, 361–2 (1995).

376. Y. Yafet, in *Solid State Physics*, (Ed.) H. Ehrenreich, F. Seitz and D. Turnbull, Vol **14**, Academic, N.Y. (1965).

377. F. Beuneu and P. Monod, *Phys. Rev.* **B18**, 2422–5 (1978).

378. R.A.B. Devine and R. Dupree, *Phil. Mag.* **21**, 787–802 (1970).

379. R. Catterall and P.P. Edwards, *Adv. Mol. Relaxation Processes* **7**, 87–103 (1975).

380. P. Monod and F. Beuneu, *Phys. Rev.* **B19**, 911-16 (1979).

381. F. Beuneu and P. Monod, *Phys. Rev.* **B13**, 3424–30 (1976).

382. F. Rachdi and P. Bernier, *Phys. Rev.* **B33**, 7817–19 (1986).

383. D. Billaud, J. Ghanbaja, J.F. Marêché, E. McRae and C. Goulon, *Synth. Met.* **28**, D147–54 (1989).

384. P. Bernier, C. Fite, A. El-Khodary, F. Rachdi, K. Zniber, H. Bleier and N. Coustel, *Synth. Met.* **37**, 41 (1990).

385. P. Lauginie, H. Estrade, J. Conard,. D. Guerard, P. Lagrange and M El Makrini, *Physica B & C* **99**, 514–20 (1980).

386. K. Tanigaki, M. Kosaka, T. Manako, Y. Kubo, I. Hirosawa, K. Uchida and K. Prassides, *Chem. Phys. Lett.* **240**, 627 (1995).

387. K. Tanigaki and K. Prassides, *J. Mater. Chem.* in press (1995).

388. A. Bartl, L. Dunsch, D. Schmeisser, W. Gopel and H. Naarmann, *Synth. Met.* **69**, 389–90 (1995).

389. M. Honda, Masters Thesis, Tokyo Metropolitan Unviersity (1994).

390. F.J. Adrian, *Phys. Rev.* **B5**, 2682–5 (1982).